SMART NANOCOMPOSITES

Volume 5, Number 2, 2014

Table of Contents

nova publishers
New York

Smart Nanocomposites

This Journal presents new studies in the fast growing area of smart materials, in particular, composite nanostructured materials. It focuses on the physics and physical chemistry of surfaces, interfaces, thin films and coatings, nanoparticles and other nanostructures, as well as on their new and smart applications. Original approaches in fabrication and applications of nanostructured materials will get special attention. Nanostructured ceramics, alloys, various nanocarbon forms (nanotubes, fullerenes, graphene) and their composites used in sensors (including single molecule sensing) and actuators, artificial metabolism, drug delivery, selective membranes, fuel cells, energy storage, and photovoltaics are just a few examples of new classes of materials and applications that are within the scope of the Journal. It features the results of interdisciplinary research from universities, national labs, and privately owned companies.

The Journal is peer-reviewed with the highest standards and quality of publications. The purpose of this Journal is to bring the most up-to-date advances in nanotechnology together, and to give research groups the opportunity to compare their results with other groups' data. To achieve this, the Journal focuses mostly on practical applications of nanodevices, and on proof of the concept publications. Areas of interest include (but not are limited to): sensors, smart membranes, smart coatings for corrosion protection, aspects of significance to nanorobots: power supplies, nanorobot manipulating devices, and microchips for artificial intelligence. The Journal also deals with safety issues: safety of nanotechnology to the environment, controlling the nanodevices, and other aspects.

Smart Nanocomposites
is published in two issues per year by

Nova Science Publishers, Inc.
400 Oser Avenue, Suite 1600
Hauppauge, New York 11788-3619, U.S.A.
E-mail: nova.main@novapublishers.com
Web: www.novapublishers.com

ISSN: 1949-4823

Subscription Rate per Volume
Print: $245 Electronic: $245 Combined Print + Electronic: $367

Additional color graphics might be available in the e-version of this journal.

Smart Nanocomposites
Volume 5, Number 2
ISSN: 1949-4823

FEATURES OF COLLOIDAL QUANTUM DOTS SYNTHESIS IN NONPOLAR AND AQUEOUS MEDIA

O. A. Aleksandrova[1], D. S. Mazing[*,1], L. B. Matyushkin[#,1], V. A. Moshnikov[1,2] and N. S. Pshchelko[3]

[1]Department of Micro- and Nanoelectronics, Saint-Petersburg State Electrotechnical University "LETI",
Russia, St. Petersburg
[2] Department of Integral Electronics, St. Petersburg State Polytechnic University,
Russia, St. Petersburg
[3] Department of General and Technical Physics, St. Petersburg State Mining University,
Russia, St. Petersburg

ABSTRACT

Colloidal quantum dots (QDs) of cadmium selenide are synthesized in non-polar media and in aqueous media. Setup for colloidal QDs synthesis is described. Absorption and photoluminescence (PL) spectra of CdSe QDs are presented. The size of nanoparticles can be estimated as being less than 3 nm. The self-organization processes in ordering of PbS QDs are studied.

Keywords: colloidal quantum dots (QDs), synthesis in non-polar media, synthesis in aqueous medium, absorption spectra, photoluminescence spectra

INTRODUCTION

Colloidal semiconductor quantum dots (QDs) are of great interest due to their size-tunable photoemission characteristics which make them prospective material for fundamental studies [1, 2] and technical applications such as light-emitting devices [3, 4], lasers [5, 6], fluorescent labels and biosensors [7 - 10].

Combination of high spatial resolution fluorescence microscopy with state-of-the-art optical methods allows performing different kinds of intracellular diagnostics for medical and biological purposes. Simple non-distractive techniques based on fluorescent labels provide on-line acquisition of updating information about monitored object. Till now for such

[*] dmazing@yandex.ru
[#] leva.matyushkin@gmail.com

objectives organic fluorophores, fluorescent proteins and luminescent metal complexes have been employed. Their usage, however, is complicated by low absorption coefficients and poor stability to photobleaching making it impossible to carry out prolonged experiments [11].

Therefore there is a demand for fluorescent nanomaterials with high brightness and photostability under physiological conditions. Due to low dimensions, semiconductor nanoparticles offer local sensitivity for fluorescent methods. Because optical properties of semiconductor QDs are defined by quantum confinement (smaller nanocrystals are characterized by wider bandgap) emission band may be regulated by the size and composition of nanocrystal core. Another advantage of QDs as fluorescent labels is continuous absorption band which means that nanoparticles of different sizes can be excited by the same excitation source.

In order to cover different optical ranges AIIBVI semiconductors ZnO, ZnS, ZnSe, ZnTe, CdS, CdSe, CdTe are suitable for colloidal QDs production for applications in visible spectrum from violet to deep red. Photoluminescence (PL) in near infrared part of the spectrum can be obtained using lead calchogenides – PbS and PbSe. Colloidal QDs technology comprises non-polar, polar and mixed media synthesis methods. Typical synthesis of colloidal nanocrystals includes sources of ion species of nanoparticle core semiconductor material (precursors), surfactants which passivate nanoparticle surface hindering agglomeration and eliminating dangling bonds, and reaction medium. The role of surfactant is multifunctional. It not only provides colloidal stability but also passivates defect states on the surface of nanocrystals which could act as traps for charge carriers causing deterioration of luminescent properties. Moreover, the nature of stabilizing molecules being used, determines course of the nucleation stage and strongly affects reaction dynamics throughout growth phase of nanocrystals.

Historically the most developed and widely used is hot injection method which was proposed in the beginning of 90s [12]. By virtue of separating processes of nucleation and growth it allowed to obtain highly luminescent nanocrystals with good monodispersity. These techniques employ trioctylphosphine (TOP) – trioctylphosphine oxide (TOPO) based systems, in which the reagents are injected into a hot coordinating solvent at elevated temperature (200−400°C). However initial methods had certain disadvantages connected with expensive and hazardous pyrophoric reactants being used (dimethyl cadmium as cadmium precursor, organophosphorus compounds acting as solvents, surfactants and selenium precursors). It is also important to note that here solvent medium acts at the same time as surfactant making it more difficult to control synthesis procedure.

EXPERIMENT AND DISCUSSION

Experimental setup. Typical experimental setup for colloidal QDs synthesis is depicted in the Figure 1.

Usually reaction volume is a three-neck round bottom flask with one side neck being used for temperature control by means of a thermocouple and the other is for precursor solutions injections as well as taking aliquots to control course of the reaction. The central neck may be connected to condenser attached to inert gas line.

Heating is provided by fabric heating mantle with feedback via temperature controller. Injections and taking probes are conveniently carried out with glass syringes equipped with large gauge needles.

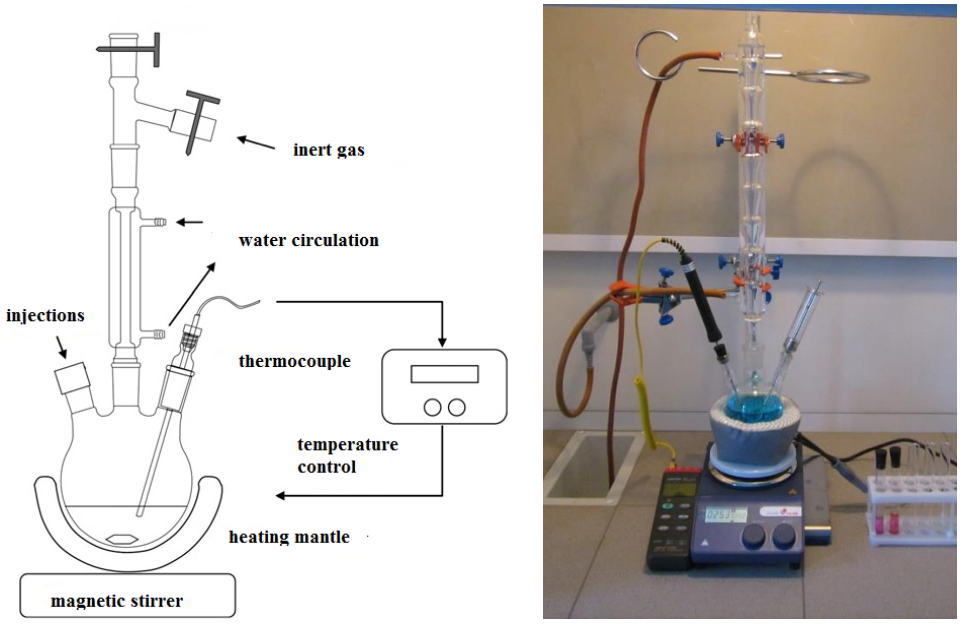

Figure 1. Setup for QDs preparation.

Colloidal quantum dots synthesis in non-polar media. Alternative routes for colloidal QDs preparation in organic solvents are based on utilization of non-coordinating solvents such as octadecene [13] and liquid paraffin [14]. Nanoparticle stabilization in this case may be achieved employing fatty acids and aliphatic amines. Instead of pyrophoric organometallic precursors corresponding oxides (CdO) or acetates might be used as sources for heavy metal species. These cheap and safe in handling compounds easily form salts of fatty acids in non-polar environment which are effective immediate sources of metal species during the reaction. Dissolution of elemental chalcogen powders upon heating or ultrasonic treatment in non-coordinating solvents yields highly reactive precursor solutions as well.

Using this facile approach oleic acid stabilized CdSe QDs with narrow emission band (full width at half maximum less than 35 nm) and quantum yield of bare nanocrystal cores near 10% were obtained. In the Figure 2 and 3 absorption and PL spectra of CdSe QDs prepared with molar ratio upon initial selenium precursor injection [Cd]:[Se] = 4:1 are presented. To monitor the reaction, the samples were taken in certain time intervals after the first injection. From the position of the first excitonic absorption peak the mean size of nanoparticles can be estimated as being less than 3 nm. Nanocrystal growth may be promoted further to obtain larger wavelength values by additional injections of Se precursor as reflected in the Figure 2. Doing so it is possible not only to expand spectral range but also tackle broadening of size distribution caused by depletion of free monomers during the reaction (Ostwald ripening).

In another implementation of phosphine-free technique liquid paraffin was used as synthesis medium of CdSe QDs stabilized with oleic acid (Figure 4 shows PL spectra) [15].

In order to make initial assessment of colloidal QDs fluorescence UV-lamp is often used. But visual perception might be deceptive. A quick checking of solutions under UV lamp showed an unusual order of the fluorescence colors: the first sample has red fluorescence, the second sample has yellow fluorescence, and finally the third sample has green fluorescence, while the quantum dots of cadmium chalcogenides demonstrate reverse order: the shorter the time of the synthesis and accordingly size of quantum dots, the smaller the wavelength.

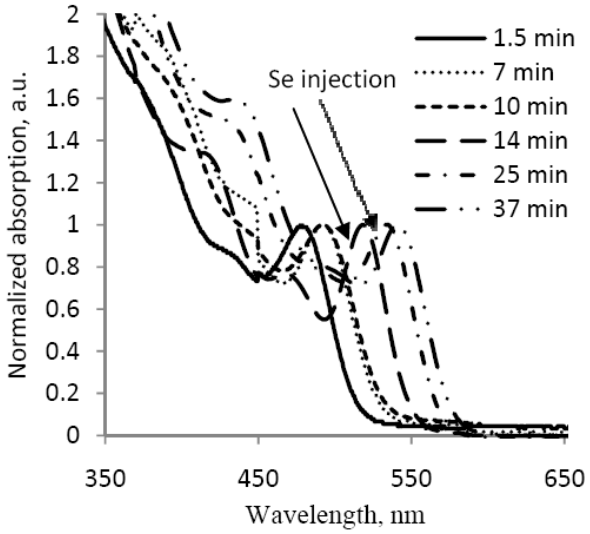

Figure 2. Absorption spectra of CdSe QDs prepared with use of Se precursor multiple injection in octadecene medium.

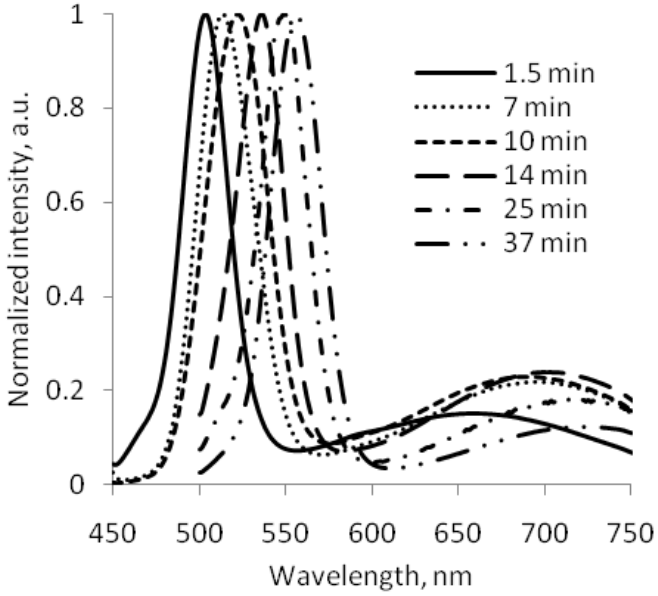

Figure 3. PL spectra of CdSe QDs prepared with use of Se precursor multiple injection in octadecene medium.

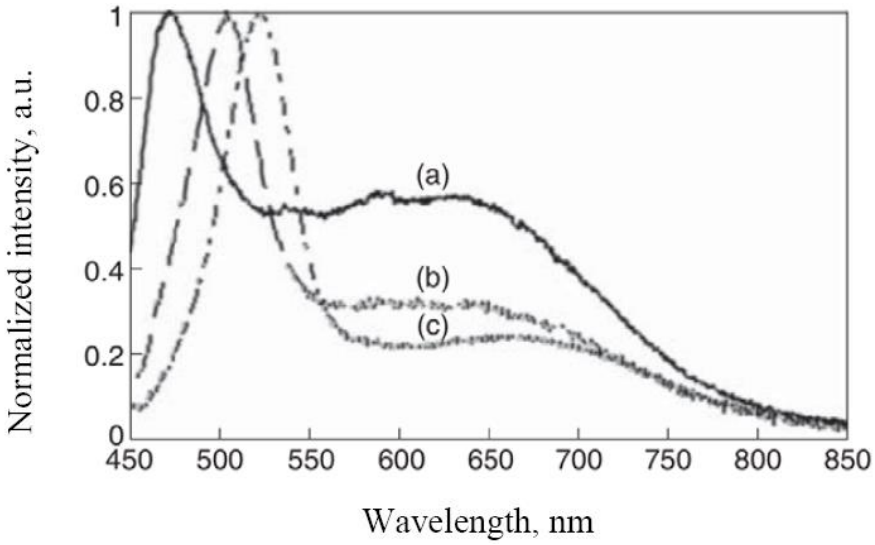

Figure 4. Normalized PL spectra of CdSe quantum dots as function of time:
(a) 1 min, (b) 2 min, (c) 5 min after injection [15].

PL spectra in the Figure 4 show that all of the samples contain two features on spectral characteristics: narrow shortwave part of high intensity, which we attribute to the interband radiative relaxation in synthesized quantum dots (half-width range of 50–75 nm) and wide area in the long-wavelength region extending to a wavelength of 800 nm associated with emission via surface defects energy levels inside bandgap. As can be seen nanoparticle size increases with reaction time with concurrent relative decreasing of long-wavelength emission band which points at gradual passivation of nanoparticle surface defects by surfactant molecules. This spectrum behavior explains reverse order of QDs emission color as visual sensations depend on the ratio of areas under broad and sharp peaks.

Synthesis of colloidal quantum dots in aqueous medium. In order to render colloidal nanoparticles biocompatible it is instructive to make them water soluble which makes polar solvents to be natural choice of medium for QDs preparation.

Despite poorer crystallinity and therefore generally inferior optical properties as compared to nanoparticles synthesized in non-polar media these methods are considered to be more environmentally benign and provide nanocrystals compatibility with biological tissues eliminating necessity for ligand exchange operations. Suitable precursors in this case may include water-soluble metal and chalcogenide salts as sources of metal and chalcogenide ions respectively while thiols might be used for surface passivation.

Figure 5 and 6 contain absorption and PL spectra of CdSe QDs prepared in water solution using thioglycolic acid (TGA) as stabilizator. Here cadmium chloride ($CdCl_2 \cdot 2.5H_2O$) and sodium hydroselenide (NaHSe) were used as sources of cadmium and selenium species respectively.

Upon heating from 30 to 90 °C the samples exhibited characteristic shift of absorption onset and PL band towards larger wavelengths. It is well seen that thus prepared nanoparticles are characterized by wide emission band and large Stokes shift (offset between absorption and emission maxima) which points to mechanism of PL associated with radiative relaxation via surface trap states inside bandgap [16].

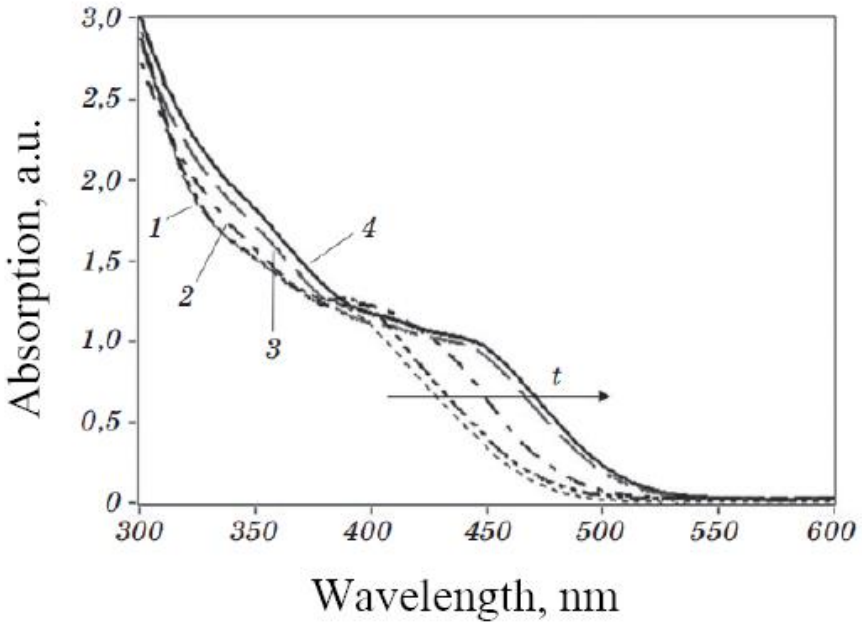

Figure 5. Absorption spectra of CdSe QDs stabilized with TGA.

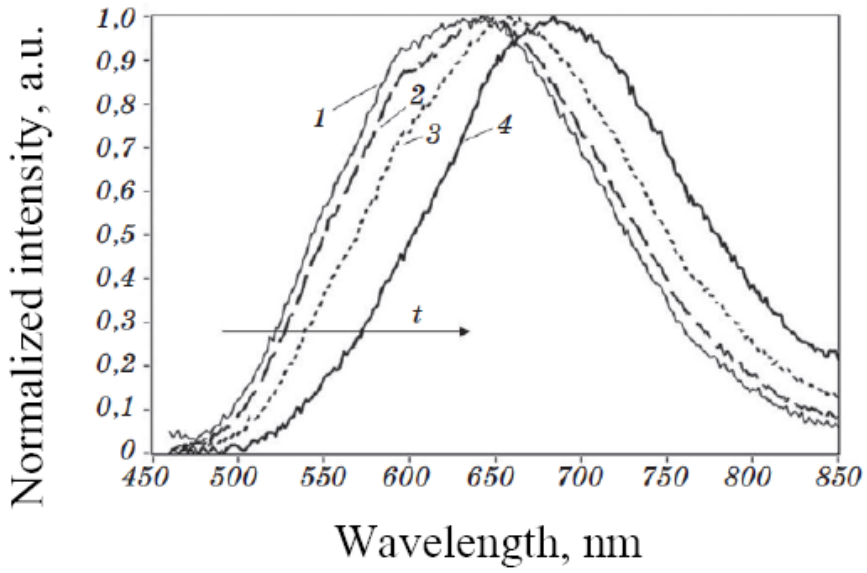

Figure 6. PL spectra of CdSe QDs stabilized with TGA.

Stability of these nanoparticles was observed to be much worse than of those prepared in organic medium (about one month without purification and even less after). The sample instability may be ascribed to photochemical degradation of thiol capping. Namely photooxidation of thiol ligands results in formation of disulfides which are less soluble in water and are not bonded to nanoparticle surface. If there is lack of free ligands in the solution to retain stabilization this leads to nanocrystal precipitation [17].

Study of the self-organization processes in ordering of quantum dots. In contrast to QDs produced by molecular beam epitaxy properties of colloidal QDs are independent of the substrate type. Particles can be deposited from organic and aqueous solutions onto rigid and flexible, smooth and even, bent and planar substrates. The substrate material may be either inorganic or organic (including biological materials); crystalline or amorphous; conducting, semiconducting or insulating. In this case, the matrix must not disrupt the crystal structure of the QDs. This leads to a number of difficulties in the development of preparation techniques.

The goal of the study [18] was to develop synthesis procedures that combine the synthesis of colloidal QDs in aqueous solutions and their simultaneous organization into ordered arrays. The developed synthesis procedures were intended for the creation of microstructures for the noninvasive diagnostics of biological tissues in the spectral range 0.9–1.7 μm. The performed synthesis of lead sulfide nanoparticles is based on the ion exchange reaction between lead acetate Pb $(CH_3COO)_2 \cdot 3H_2O$ and hydrogen sulfide H_2S. An aqueous solution of hydrogen sulfide is added to a solution of lead acetate in a 1% solution of polyvinyl alcohol. During the process, the long-chain molecules of polyvinyl alcohol served as a stabilizer of the colloidal solution. Further, the colloidal solution was deposited on glass substrate and the drop sample was dried for 24 h under standard conditions, with the result that the volume of the drop decreased and its edges were "darkened." We obtained PL signals in the expected spectral range (1–1.7 μm), which is markedly different from the emission range for bulk lead sulfide (3 μm). This confirmed that the synthesized samples contain a substantial concentration of QDs and are promising for application in luminescent devices.

To examine the volume redistribution of particles during the course of their self-organization upon sample drying, we compared the PL spectra at different positions of the laser light spot over the sample (Figure 7).

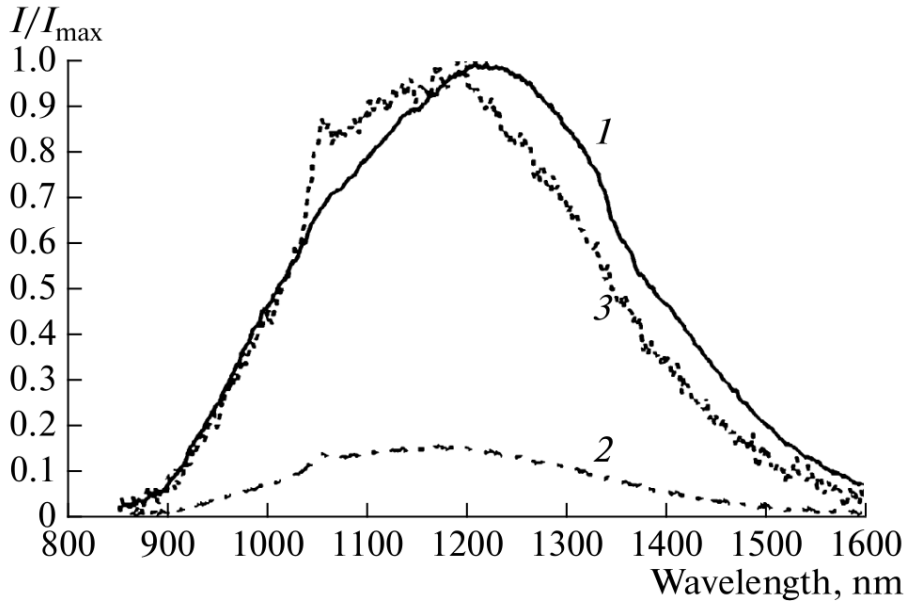

Figure 7. PL spectra from different parts of the sample: (1) at the edge of the dried drop, (2) at the center of the sample, and (3) at the center of the sample (spectra normalized to unity) [18].

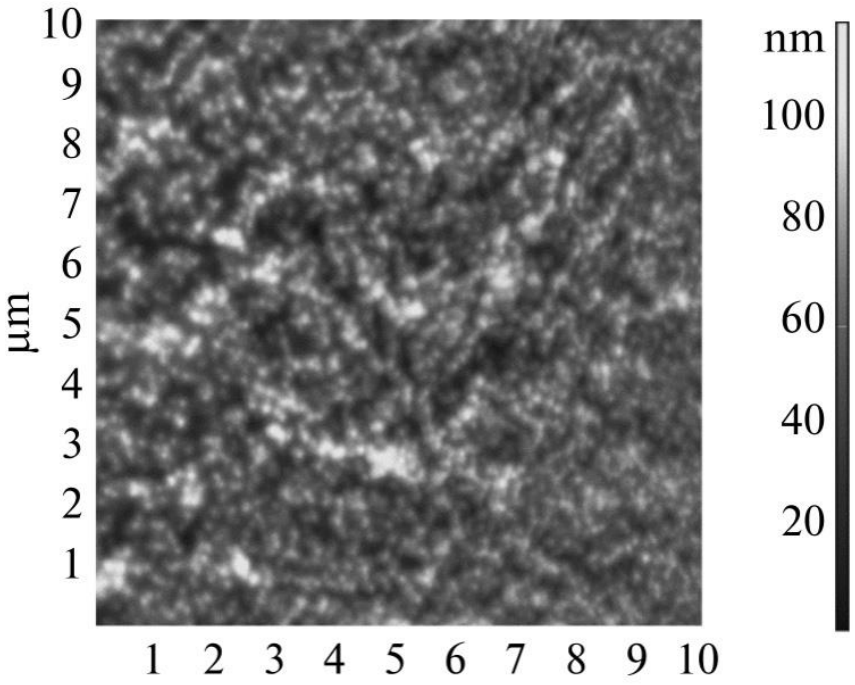

Figure 8. AFM image of the sample edge (10 × 10 μm scanning region) [18].

The signal intensity at the edge of the sample was 8 times higher than at its center. The position of the peak and the FWHM of the line change only slightly. This fact means that the QDs have approximately the same size dispersion over the entire drop and are present in the whole sample, including at its center. Comparison of the luminescence intensities at the edge of the sample and at its center (spectra *1* and *2* in Figure 7) shows that the most favorable conditions for formation of colloidal QDs arrays are created near the thin edge layer.

To examine the structure of the sample in detail, we used the AFM method with a tapping oscillatory procedure using Ntegra Terma installation. It was found that a large number of nanoparticle aggregates of intermediate size on the order of hundreds of nanometers are present near the drop edge (Figure 8).

On passing to the middle part of the drop, a network like structure is formed, which is accompanied by an increase in the profile depth to 0.5 μm. Probably a small number of lead sulfide particles are distributed in this region in other reaction products present in the initial solution.

CONCLUSION

Luminescent colloidal nanocrystals are the most prospective substitution of organic fluorophores being used nowadays.

Their advantages include high quantum yield, continuous absorption spectrum and higher stability to photo degradation.

The progress in the development of preparation techniques based on employing non-coordinating solvents and water medium reduces cost and makes colloidal QDs synthesis

environmentally friendly. Because of facility of colloidal QDs surface modification, compatibility with media of different nature and variety of materials eligible for low cost wet-chemistry methods of QDs production the range of their possible applications constantly increases.

ACKNOWLEDGMENT

The authors would like to thank S.A. Tarasov for his help in some photoluminescence measurements. The study was financially supported by the Russian Science Fund (project №14-15-00324).

REFERENCES

[1] Fisher B., Caruge J.M., Bawendi M.G. Room-Temperature Ordered Photon Emission from Multiexciton States in Single CdSe Core-Shell Nanocrystals // *Physical Review Letters* 2005, 94: 087403.

[2] S. Empedocles and M. Bawendi Spectroscopy of Single CdSe Nanocrystallites // Acc. *Chem. Res.*, 1999, 32 (5), P. 389–396.

[3] Caruge J. M., Halpert J., Wood E. V. et al. Colloidal quantum-dot light-emitting diodes with metal-oxide charge transport layers // *Nature Photonics*. 2008. Vol. 2. P. 247–250.

[4] Tan Z., Zhang F., Zhu T. et al. Bright and color-saturated emission from blue light-emitting diodes based on solution-processed colloidal nanocrystal quantum dots // *Nano Lett. 2*007. Vol. 7, N 12. P. 3803–3807.

[5] Hoogland S., Sukhovatkin V., Howard I. et al. A solution-processed 1.53 μm quantum dot laser with temperature-invariant emission wavelength // *Optics Express*. 2006. Vol. 14, N 8. P. 3273–3281.

[6] Cuong Dang, Joonhee Lee, Craig Breen, Jonathan S. Steckel, Seth Coe-Sullivan and ArtoNurmikko Red, green and blue lasing enabled by single-exciton gain in colloidal quantum dot films // *Nature Nanotechnology.* 2012. Vol. 7, P. 335–339 (2012)

[7] Ruedas-Rama M. J., Walters J. D., Orte A. et al. Fluorescent nanoparticles for intracellular sensing: A review // *Analytica Chimica Acta*. 2012. Vol. 751. P. 1–23.

[8] Algar W. R., Tavares A. J., Krull U. J. Beyond labels: A review of the application of quantum dots as integrated components of assays, bioprobes, and biosensors utilizing optical transduction // *Analytica Chimica Acta*. 2010. Vol. 673. P. 1–25.

[9] Musikhin S. F., Aleksandrova O. A., Luchinin V. V., Maksimov A. I., Moshnikov V. A. Semiconductor colloidal quantum dots in medicine and biology// *Biotekhnosfera* 2012. N. 5(6) P. 40–48. (in Russian)

[10] Musikhin S. F., Aleksandrova O. A., Luchinin V. V., Maksimov A. I., Matyushkin L. B., Moshnikov V. A. Sensors based on metal and semiconductor colloidal nanoparticles for biomedicine and ecology// *Biotekhnosfera* 2013. N. 2(26). P. 2–16. (in Russian)

[11] Resch-Genger U., Grabolle M., Cavaliere-Jaricot S. et al. Quantum dots versus organic dyes as fluorescent labels // *NatureMethods.* 2008. Vol. 5. P. 763–775.

[12] C.B. Murray, D.J. Norris, M.G. Bawendi Synthesis and Characterization of Nearly Monodisperse CdE (E = S, Se, Te) Semiconductor Nanocrystallites// *Journal of the American Chemical Society*.1993. Vol.115. P.8706–8715.

[13] X. Peng, L. Qu , Z. A.Peng Alternative Routes toward High Quality CdSeNanocrystals // *Nano Letters.* – 2001. Vol.1 (6). P. 333–337.

[14] L. Wang, X. Sun, W. Liu etal. High quality zinc-blende CdSenanocrystals synthesized in a hexadecylamine–oleic acid–paraffin liquid mixture// *Materials Chemistry and Physics*. 2010. Vol.120. P.54–60.

[15] Aleksandrova O.A., Gordushenkov O.E., Matyushkin L.B., Menkovich E.A., Mikhailov I.I., Moshnikov V.A., Romanovskiy D.S., Tarasov S.A. Phosphine-free synthesis of CdSe colloidal quantum dots with inverse order of fluorescence color // 21st Int. Symp. «*Nanostructures: Physics and Technology» Proceedings*. 2013. P. 298-299.

[16] D. S. Mazing, L. B.Matyushkin, O. A.Aleksandrova, I. I.Mikhailov, V. A.Moshnikov and S. A.Tarasov Synthesis of cadmium selenide colloidal quantum dots in aquatic medium// *J. Phys.: Conf. Ser.* 2014. 572 012028.

[17] J. Aldana, Y. A. Wang, and X. Peng Photochemical Instability of CdSe Nanocrystals Coated by Hydrophilic Thiols// *J. Am. Chem. Soc*. 2001. Vol. 123. N. 36. P. 8844-8850.

[18] Tarasov S.A., Aleksandrova O.A., Maksimov A.I., Maraeva E.V., Matyushkin L.B., Men'kovich E.A., Moshnikov V.A., Musikhin S.F. Study of the self-organization processes in lead sulfide quantum dots // *Semiconductors.* 2014. Vol.48, N.13, P. 1729–1731.

Smart Nanocomposites
Volume 5, Number 2
ISSN: 1949-4823

COATINGS CONTAINING CONJUGATED POLYMERS FOR CORROSION PROTECTION OF ACTIVE METALS

***Kirill Levine*[*,1,2] *and Balaram Sahoo*[3]**
[1]Department of General and Technical Physics,
National Mineral Resources University, St. Petersburg. Russia
[2]Institute of Macromolecular Compounds, Russian Academy of Sciences
[3]Materials Research Centre, Indian Institute of Science, Bangalore, India

ABSTRACT

Corrosion protection of active metals is an example where smart behavior of nanostructured coatings can be shown and their advantages in corrosion protection are obvious, compared to regular materials. Electrochemical methods allow precise study of this phenomenon. Reported study was focused on different aspects of diffusion-linked smart behavior in relation to the properties of oxide-coated surface of active metals. Few mechanisms are competing during corrosion: surface ennobling by intrinsically conducting polymers, intermolecular diffusion through homogeneous polymer structure, swelling of conjugated polymer filler, dopant release to intermolecular voids, and ingress of aggressive ions into coating through imperfections in the coating. All those mechanism occur simultaneously. Electrochemical impedance spectroscopy in this paper was employed as a tool of a precise close-look at coating's behavior, and the discussion is provided.

Keywords: corrosion protection of aluminum, conducting polymers, polypyrrole, electrochemical impedance spectroscopy, aluminum oxide, nanocomposite, diffusion

INTRODUCTION

By active metals, such as aluminum (Al) or magnesium (Mg), are usually understood metals, which lie far below the hydrogen potential in the electrochemical series. High chemical activity of those metals would prevent their long-lasting existence in oxygen or water vapor containing environment unless they are protected by oxide layer. Indeed, oxide layer formed on the surface of the majority of active metals protects them from environmental decay. Aluminum alloys because of the ability of Al to react with impurities and alloying elements, are prone to developing intermetallic (IM) impurities during the solidification

* Corresponding author: Email: levinkl@hotmail.com; rectorat@spmi.ru

process. These IM phases can act as initiation sites for localized corrosion processes, resulting in degradation phenomena, such as pitting

To protect Al alloys, hexavalent chromium coatings were used, however, hexavalent coatings technology is carcinogenic and needs replacement. The most promising approaches utilize Mg-rich coatings [1], coatings by conjugated polymers (CPs) [2], and coatings containing conjugated polymer modified nanoparticles [3].

The ideology behind using Mg rich coatings is M1 sacrificing for the sake of M2 (metal surface), where M1 is metal which is more electro-negative than metal M2, for example: M1 is Mg and M2 is Al [1]. Coatings cited in mentioned article, do demonstrate performance, however, it is not clear how this coatings will perform after all M1 is consumed.

In this paper, approaches utilizing CPs are expanded, and their connection to nanotechnology is discussed.

CPs and Their Anti-Corrosion Performance

Example of CPs is shown in Figure 1. All of them were evaluated for corrosion control of Al alloys [4-8]. The main CPs limitation in corrosion control is their poor adhesion to active metal surface when deposited chemically. As a result, CPs are either incorporated as a pigment to a traditional polymeric binder [4, 8], or deposited onto surface electrochemically.

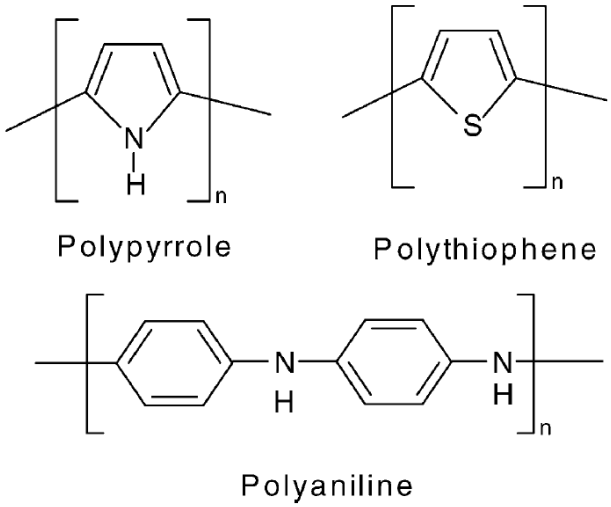

Figure 1. Examples of conducting polymers.

Electrochemical deposition of CPs to active metal surfaces is a challenge, and cannot be undertaken without special surface preparation strategies. Special electrolytes, high monomer concentrations must be used and even with them overoxidized polymer is often obtained [9, 10].

Approach suggested in [11, 12] utilizes so-called electron transfer mediators (ETMs) to reduce the deposition potential of polypyrrole (PPy) on aluminum and aluminum alloy by approximately 500 mV, permitting film deposition from aqueous solution with nearly 100% current efficiency.

The mediator used most often in this work was the disodium salt of 4,5-dihydroxy-1,3-benzenedisulfonate (DHBDS), which also served as the dopant or counter ion in the polymer, but other mediators appear promising [10]. DHBDS mediates both the initial nucleation (initial PPy deposition on the Al_2O_3 surface) and the film growth stage.

Meanwhile PPy deposition in the presence of ETMs allows significant surface modification, it does not take advantage of natural corrosion control performance of Al oxide. Additional oxide growth utilized such performance in connection with ennobling CPs properties [13]. The oxide structure was clearly identified as porous by SEMin contrast to bare Al (Figure 2). Highly adherent PPy film with electrochemical potential + 100 mV vs. SCE was formed at an oxide surface. OCP of a formed layer exceeded bare Al by 1000 mV, while it hardness have reached 1600 Vickers (vs. 1900 for bare Al). The corrosion control experiment was settled for 2 weeks, showing progressive performance.

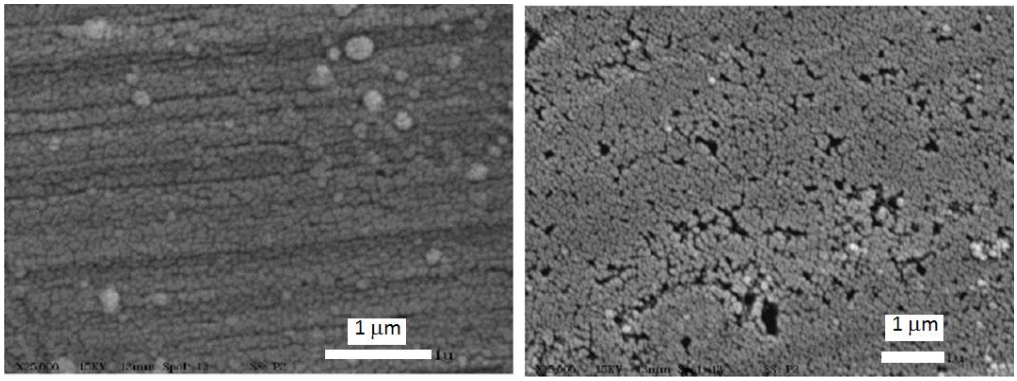

a b

Figure 2. SEM images of untreated aluminum (a) and porous aluminum (b) surface [11].

Electron Transfer Mediators to Enhance the Deposition of Conjugated Polymers

Problem arising in the direct deposition of CPs onto active metal surface is the competing oxide growth going simultaneously with the electrodeposition. In the case of aluminum and its alloys, a high bandgap (i.e., electronically insulating) oxide forms under such conditions and an adherent, continuous CP film is difficult to achieve without resorting to special surface preparation strategies and electrolytes, and even then high monomer concentrations must be used, which often results in an over-oxized polymer [14, 15].

When monomer of pyrrole or another CP is dissolved in the solution, it can be polymerized electrochemically by oxidative free-radical polymerization mechanism first described by Diaz [14]. Electrochemical method allows overcoming the difficulty of competing surface oxidation with the help of a so-called electron transfer mediators (ETMs), such as DHBDS. The mechanism of its action is shown in Figure 4.When DHBDS is dissolved in aqueous solution it dissociates forming anions. At anode their hydroxyl groups release proton and acquire positive charge which is immediately transferred to monomer with proton returned back. Therefore ETM is returned to its anionic state while monomer is

oxidized. This process repeats continuously resulting in collecting oxidized monomers in pre-anodic space and their polymerization and film growth.

CPs electronic structure and morphology allows so-called doping, the process of simultaneous attaining positive or negative charge to a polymer chain followed by migration into polymer chain counter-ion which maintains electroneutrality [16]. Doping can be achieved chemically or electrochemically. In the case of electrochemical doping, film must be in good electrical contact with electrode by its one side and face the solution containing dissolved dopant ions by its other side.

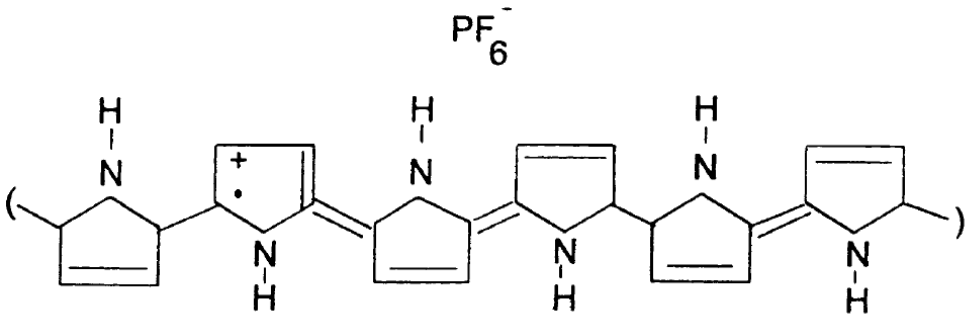

Figure 3.An example of PPy doped by hexafluorophosphate ion.

Approach that uses ETMs allows the reduction of PPy deposition potential on Al and its alloys by nearly 500 mV, permitting CP film deposition from aqueous solution with high current efficiency [10].

Anion of DHBDS also can serve dopant to CP.

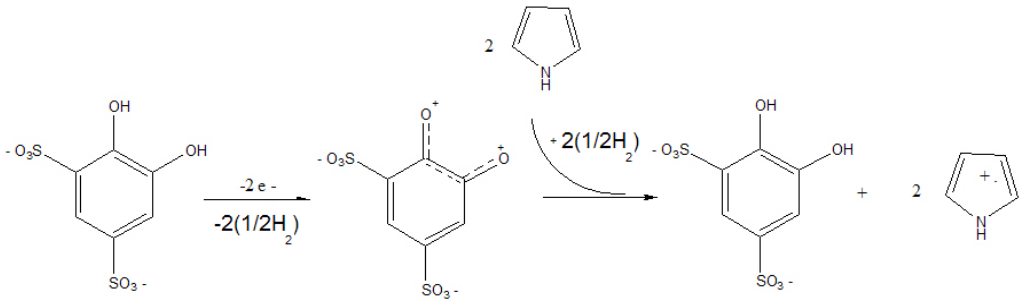

Figure 4.Schematic representation of DHBDS action on pyrrole oxidation.

Corrosion Control by Oxygen Reduction Inhibitors

When corrosion starts at metal surface, an electron is released.

$Al \rightarrow Al^{3+} + 3e^-$,

The released electron is consumed to reduce oxygen:

$½\ O_2 \rightarrow O^{2-} - 2e^-$.

Oxygen ion reacts with metal ion to form corrosion by-products, such as oxide, hydroxides and other species:

$2Al^{3+} + 3O^{2-} \rightarrow 2Al_2O_3$

$Al^{3+} + 3(OH^-) \rightarrow Al(OH)_3$

By lowering down oxygen ion formation, corrosion rate can be lowered down. For this purpose, oxygen reduction inhibitors (ORIs) can be used as dopants. An example of ORI, is 2,5-dimercapto 1,3,4-thiadiazole (DMCT), Figure 5. Using ORI's is believed to significantly slow down corrosion [17] in the way it is shown in Figure 6:

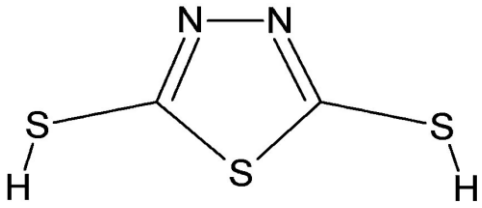

Figure 5.ORI 2,5-dimercapto 1,3,4-thiadiazole, (acid form).

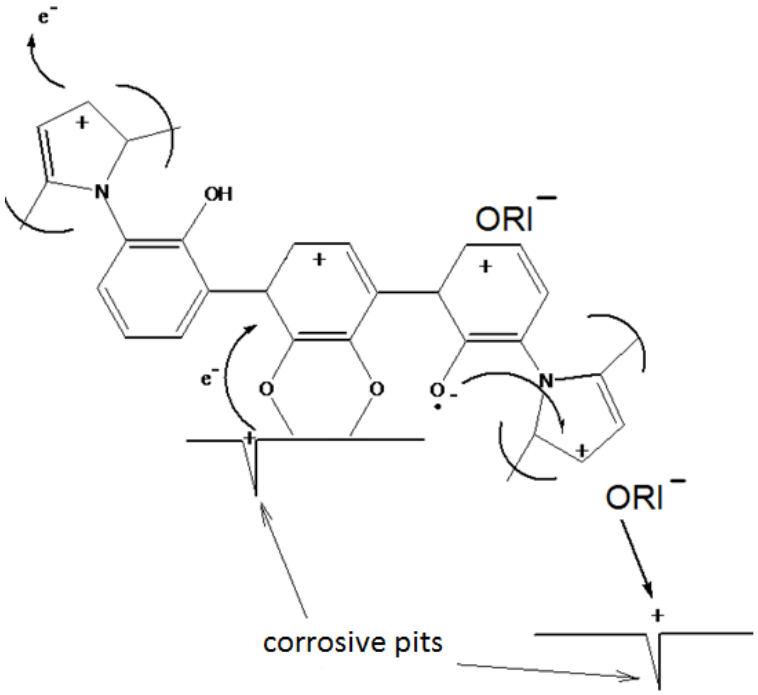

Figure 6.Schematic representation of ORI release.

1. As a result of corrosion, an electron is released, (corrosive pit at the left).
2. An electron is absorbed by conjugated double bond electronic structure.
3. From the electroneutrality considerations, ORI^- ion is released at the location of a corrosive pit, (shown at right-hand side of the figure).
4. Further corrosion is slowed down due to an ORI action.

Opponents of this theory have justified that this mechanism needs the corrosion to be started in order to be in force. This is however possible to use nanoparticles containing active metal dispersed in primer layer to supply electron and therefore to being consumed before corrosion reaches the protecting surface. For example, this can be Mg nanoparticles or Al nanoparticles even in the case when protecting metal is Al for the reason that nanoparticles are much more chemically active than flat metal surface. Indeed, surface area per unit mass for nanoparticle is inversely proportional to radius, therefore, making dispersed metallic particles sufficiently small, their chemical activity can be controlled.

Interfacial properties of protecting surface and polymer film plays a key role in electron transfer from metallic surface, which is responsible for corrosion. Surface treatment with CPs affects it electron transfer properties allow surface ennobling - making electrochemical potential more positive, therefore, slowing down corrosion [18]. CP modified surfaces are also attractive from the point of view of their biocompatible applications [19].

CP Interaction with Developed Oxide Surface of Active Metal

Adhesion between coating and metallic surface plays a key role in its protective properties. In addition to good mechanical contact, CP layer developed at an oxide surface ennobles the surface, providing additional mechanism of protection. Due to high ohmic drop at oxide, CP electrochemical deposition at oxide surface required high overpotential:

$$E_{appl} = E_{Sh} + E_{Ox} + E_{PPy\ dep} \quad \text{Eq. 1}$$

where: E_{appl} – applied potential, E_{Sh} – potential drop due to Shottky junction, E_{ox} – potential drop at oxide, E_{PPydep} – potential drop required to for PPy deposition, however, increased open circuit potential (OCP) (from -0.9 for bare Al to 0.0 for PPy coated oxide)[1] indicates excellent protective properties provided by CP . Bare and oxide coated surface is shown in Figure 2 for comparison.

Characterization of Porous Layers by Impedance Methods

Electrical conductivity of the solution σ is contributed by the conductivity of several types of ions *i*:

$$\sigma = \sum n_i \mu_i \mid q_i \mid \quad \text{Eq. 2}$$

[1]Potentials are given vs. SCE (Saturated calomel electrode).

where: n_i is concentration, q_i is charge, and μ_i is mobility of i^{th} ion. An oxide layer can be taken as permeable membrane which is placed between metal and solution. If membrane resistancer_{pore} is much higher than the solution resistance r_{sol} ($r_{pore} >> r_{sol}$), than measurable quantity characterizes the resistance of pores (pore resistance) [21]. The resistance of a cylindrical pore, Figure 7(a), with index j ($r_{pore\,j}$) can be written as

$$r_{porej} = \rho \frac{d}{A_p} \qquad \text{Eq. 3}$$

and

$$A_p = \pi r_{geom}^2 \qquad \text{Eq. 4}$$

where: d - pore length, A_p-crossectional area, r_{geom} - pore radius, ρ - unit resistance of the solution in pore, equal to

$$\rho = \sigma^{-1} \qquad \text{Eq. 5}$$

If pore is not cylindrical, Figure 7(b), its resistance can be determined by integrating

$$r_{pore\,j} = \rho \int_V \frac{dV}{A(x,y,z)}, \qquad \text{Eq. 6}$$

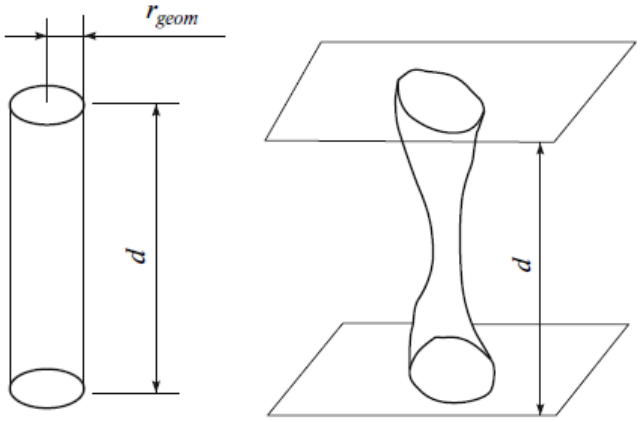

Figure 7.Ideal (a) and non-ideal (b) pore.

By taking sum of separate parallel pores by index j, the entire film resistance can be determined as

$$r_{pore}^{-1} = \sum_{j=1}^{N} r_{pore(j)}^{-1} \qquad \text{Eq. 7}$$

that is a mathematical meaning of pore resistance.

Measured at small frequency (1/2π Hz) cell resistance r_{cell}, determined from Bode plot can be written as:

$$r_{cell} = r_{sol} + r_{pore} + r_{pol} \quad \text{Eq. 8}$$

In this equation r_{sol} solution resistance which can be neglected, r_{pol} is polarization resistance which is of the same order as r_{pore} [22]. Therefore:

$$r_{cell} \approx r_{pol} + r_{pore} \quad \text{Eq. 9}$$

$r_{pol}$is out of interest because it can be eliminated by selecting zero potential which equilibrates film with the solution making

$$r_{cell} \approx r_{pore} \quad \text{Eq. 10}$$

and in this case can be determined from low frequency part of Bode plot. Diffusion characteristics also can be obtained from EIS data [22].

CONCLUSION

In this study some aspects of corrosion protection methods and approaches related to intrinsically conducting polymers, such as polypyrrole, and active metals, such as aluminum were summarized. This study however did not intend to cover the entire problematic in its fundamental meaning, it was focused on aspects of diffusion-linked smart behavior with relation to oxide properties that seemed important to us. Two models were discussed and correlation between them was shown: surface ennobling by ICP – slowing down corrosion, and clogging pores by swelled ICP - therefore blocking passes to aggressive ions. In practically applied anti-corrosion coatings these processes go simultaneously. Electrochemical impedance spectroscopy was reviewed as a method suitable for a close-look at diffusion through pores of variable size. Creation of new anti-corrosion smart materials was discussed.

ACKNOWLEDGMENTS

Authors are acknowledgeable to Dr. Dennis E. Tallman from North Dakota State University for his guidance throughout a significant part of this project and Dr. Valery V. Malev from St. Petersburg State University for valuable discussion.

REFERENCES

[1] D. Battocchi, A.M. Simões, D.E. Tallman, G.P. Bierwagen, *Corrosion Science*, 2006,48(5), 1292-1306.

[2] D.E. Tallman, Y. Pae, G.P. Bierwagen, *Corrosion* 2000, 56, 401.

[3] D. E. Tallman, K. L. Levine, C. Siripirom, V. J. Gelling, G. P. Bierwagen, and S. G. Croll, *Applied Surface Science*, 254 (2008) 5452 – 5459.

[4] D. E. Tallman, Y. Pae, G. P. Bierwagen, *Corrosion* 2000, 56, 401.

[5] V. Johnston-Gelling, M. M. Wiest, D. E. Tallman, G. P. Bierwagen, G. G. Wallace, *Prog. Organic Coatings*,2001, 43, 149.

[6] D. E. Tallman, G. M. Spinks, A. J. Dominis, G. G. Wallace, *J. Solid State Electrochem*. 2002, 6, 73.

[7] D. E. Tallman, J. He, V. Johnston-Gelling, G. P. Bierwagen, G. G. Wallace, in Electroactive Polymers for Corrosion Control (Ed. P. Zarras, J. D. Stenger-Smith, Y. Wei) 2003, *ACS Symposium Series* 843, pp. 228-253 (Washington, DC).

[8] G. M. Spinks, A. J. Dominis, G. G. Wallace, D. E. Tallman, *J. Solid State Electrochem*. 2002, 6, 85.

[9] F. Beck, P Huelser, J. Electroanal. *Chem. Interfacial Electrochem*.1990, 280, 159.

[10] P. Huelser, F Beck, *J. Appl. Electrochem.* 1990, 20, 596.

[11] D. E. Tallman, C. Vang, G. G. Wallace, G. P. Bierwagen, *J. Electrochem. Soc*. 2002, 149, C173.

[12] Levine, K.L., Tallman, D.E., Bierwagen, G.P. ,*Australian Journal of Chemistry* 58, (2005) (4), 294-301.

[13] Levine, K.L., Tallman, D.E., Bierwagen, G.P. ,*ECS Transactions*, (2005) 1 (4), pp. 81-91.

[14] F. Beck, P Huelser, *J. Electroanal. Chem. Interfacial Electrochem*.1990, 280, 159.

[15] P. Huelser, F Beck, *J. Appl. Electrochem*. 1990, 20, 596.

[16] Handbook of Conducting Polymers. T.A. Scotheim, ed. by, 1st edition. 1983. Marcel Dekker, NY.

[17] M. Kendig, M. Hon, L. Warren,*Progress in Organic Coatings*, 47 (2003) 183–189.

[18] K.L. Levine, D.E. Tallman, G.P.Bierwagen, ECS Transactions, (2005) 1 (4), pp. 81-91.

[19] P. R. Bidez, S. Li, A. G. MacDiarmid, E.C. Venancio, YENWEI 3, and P. I. Lelkes, J. Biomater. *Sci. Polymer Edn*, Vol. 17, No. 1–2, pp. 199–212 (2006).

[20] K.L. Levine and J. O. Iroh, *Journal of Porous Materials*, 11, (2004), 87-95.

[21] K. L. Levine, N. S. Pshchelko, *Polymer Science series A* (Polymer Physics), 2011, Vol. 53, N 6, p 510-520.

[22] A. V. Bezmaternykh, K. L. Levine, A. G. Syrkov, I. V. Pleskunov, and V. V. Afanas'ev, Application of electrochemical impedance Spectroscopy For Characterization of Nanoporous Films, Smart Nanocomposites, 2013, Vol. 4, issue 1, pp. 47-49

Smart Nanocomposites
Volume 5, Number 2
ISSN: 1949-4823

PECULIARITIES OF ELECTRON STATE IN SYSTEM OF PARALLEL COUPLED QUANTUM WELLS

***Peter A. Meleshenko*[*,1,2], *Hang T. T. Nguyen*[3] and *Alexander F. Klinskikh*[2]**

[1]Zhukovsky–Gagarin Air Force Academy, Voronezh, Russia;
[2]Voronezh State University, Russia
[3]Vietnam National University–Ho Chi Minh City,
Ho Chi Minh City, Vietnam

ABSTRACT

In this paper we consider the system of parallel coupled identical one-dimensional quantum wells (such a system can be presented as a multi-arm quantum ring) with a given properties, namely, a width and a depth. It is shown that the number of quantum wells can be considered as a driven parameter for the position of bound states in such a system. Namely, in the case of quantum wells that contain two bound states we have shown that addition of new wells leads to the fact that the distance between the bound states decreases. Addition of the Aharonov-Bohm flux at origin of such a "ring of quantum wells" allows to change the distance between the bound states as well as their positions just only by changing the magnetic flux.

PACS 03.65.Nk, 85.35.Gv, 73.63.-b, 73.23.-b

Keywords: ballistic transport, Aharonov-Bohm effect, quantum ring

1. INTRODUCTION

In recent time various one-dimensional (quantum wires, quantum rings [1] etc.) and two-dimensional systems (such as grapheme [2]) have particular interest in connection with the development of low-dimensional technologies. In particular, such systems is widely used (or proposed to be used) in different fields, such as optics [3], spintronics [4], quantum interferometry [5] etc. It should be noted that the charge transport process in such structures is of purely quantum nature. Special kind of such low-dimensional systems is quantum interference devices (such as quantum graphs and quantum rings). Using these devices it is possible to observe the "delicate" quantum effects that are connected with the changes in the electron's wave function phase.

Here we consider (our consideration is based on the scattering theory which allow to investigate not only the continuous spectrum of charge carriers, but also the discrete spectrum) the system of parallel coupled identical one-dimensional quantum wells (such a system can be considered as a multi-arm quantum ring). State of an electron in such a system has an interesting properties, namely, if one change the number of parallel coupled quantum wells the new bound states in such a system will not appear (as is known, when the quantum wells are arranged in series, i.e., the width of the resulting quantum well increases, there are many bound states in such a system and addition of new wells leads to increasing of the number of bound states) just only shift to the limiting value which determines by the parameters of a single well. In the case of quantum wells with two bound states we have the same result, however the distance between the bound states (it should be noted that the distance between the bound states corresponds to THz frequencies) decreases when the number of wells in a system increases. As a result, the characteristics of such a system, e.g., the optical properties (namely, the frequencies of laser transitions), can be changed by addition of new wells only. Addition of the Aharonov-Bohm flux at origin of such a "ring of quantum wells" allows to change the distance between the bound states as well as their positions just only by changing the magnetic flux. As a result, the Aharonov-Bohm flux can be considered as a "strong" driven parameter for the optical properties of the system under consideration.

2. MAIN FORMALISM

Most of the problems of one-dimensional quantum mechanics can be formulated in terms of quantum graphs. Moreover, the solution of these problems in the frame of the graphs formalism could be more efficient and "elegant" in comparison with the traditional methods of quantum mechanics. A simple and clear example which demonstrates the "elegancy" of the graphs formalism is the problem of the one-dimensional quantum well.

There are various ways to solve the Schrödinger equation in the graph [6, 7, 8]. In the presented work we use the *vertex amplitudes* method [9]. The main idea of this method is to express the parameters of the problem through the values of the wave function at the vertex of graph Ψ_1 and Ψ_2. The considered method allows to solve the scattering problem in the quantum graph, to find the energy spectrum and to construct the wave functions. The classical analog of the *vertex amplitudes* method is the Kirchhoff's nodal potentials method in the theory of electrical circuits.

Let us consider the one-dimensional scattering problem for a quantum graph with the potentials that are placed in the graph's edges. We assume that the quasi-one-dimensional dynamics takes place[1]. The considered quantum graph consists of a compact part connected with the reservoirs of the charge carries by the semi-infinite edges. We denote these edges as the *in,out*-edges. In these edges the asymptotic conditions for the electron wave functions with respect to the compact part of the graph are realized.

The wave functions of an electron in the in, out-edges are:

[1]Let us note, that the quasi-one-dimensional dynamics may be realized in the lowest sub-band of a very narrow quantum wire. The wire width in the real experiments can not be infinitely narrow. But, for the quantum wire under low temperature the electron dynamics is quasi-one-dimensional because the higher transverse levels can not be excited.

$$\psi_{in} = a_{in} \exp(ikx) + b_{in} \exp(-ikx), \quad (1)$$

$$\psi_{out} = a_{out} \exp(ikx) + b_{out} \exp(-ikx), \quad (2)$$

where k is the electron wave-number. As it follows from (1) and (2) the elastic scattering takes place.

This assumption facilitates further mathematics.

In each edges γ_n of length l_{γ_n} the proper coordinates are used $\xi_{\gamma_n} \in [0, l_{\gamma_n}]$. In the in, out-edges coordinates are defined in a different way: $\xi_{in} \in (-\infty, 0)$, $\xi_{out} \in (0, \infty)$. These coordinates are just a natural parameter in differential geometry [10]. The electron wave function Ψ in the graph is represented by a set of components $\psi_{\gamma_n}(\xi_{\gamma_n})$, $n = 1,2,\dots,M$, where M is the number of edges in graph. Each element $\psi_{\gamma_n}(\xi_{\gamma_n})$ of the set is governed by the Schrödinger equation:

$$\begin{aligned} H_{\gamma_n}\psi_{\gamma_n}(\xi_{\gamma_n}) &= \varepsilon_{\gamma_n}\psi_{\gamma_n}(\xi_{\gamma_n}), \\ H_{\gamma_n} &= \left[-\frac{\hbar^2}{2}\frac{d}{d\xi_{\gamma_n}}\left(\frac{1}{m_{\gamma_n}}\frac{d}{d\xi_{\gamma_n}}\right) + V_{\gamma_n}(\xi_{\gamma_n})\right], \end{aligned} \quad (3)$$

where m_{γ_n} is an effective mass of an electron in the edge γ_n, V_{γ_n} is the real and locally measurable potential placed in the edge γ_n.

Let us consider the edge γ_n with a potential which is localized somewhere in this edge. The wave function ψ_{γ_n} can be determined by the following pairs of coefficients: $(a_{\gamma_n}, b_{\gamma_n})$ (coefficients before the potential) and $(c_{\gamma_n}, d_{\gamma_n})$ (coefficients beyond the potential).

An application of the continuity and hermiticity conditions leads to the system of linear algebraic equations for the vertex amplitudes $\Psi = (\Psi_{in} \equiv \Psi_1, \Psi_2, \dots, \Psi_{out} \equiv \Psi_n)^T$. This system contains the coefficients of functions ψ_{γ_n}. Hence to solve the obtained system for Ψ it is needed to express a_{γ_n}, b_{γ_n}, c_{γ_n} and d_{γ_n} in terms of $(\Psi_1, \Psi_2, \dots, \Psi_n)$. In order to do this we use the following obvious relations:

$$\begin{pmatrix} a_{\gamma_n} \\ b_{\gamma_n} \end{pmatrix} = \Gamma^{(1,\gamma_n)} \begin{pmatrix} \Psi_n \\ \Psi_{n+1} \end{pmatrix}, \begin{pmatrix} c_{\gamma_n} \\ d_{\gamma_n} \end{pmatrix} = \Gamma^{(2,\gamma_n)} \begin{pmatrix} \Psi_n \\ \Psi_{n+1} \end{pmatrix}. \quad (4)$$

The pairs of coefficients $(a_{\gamma_n}, b_{\gamma_n})$ and $(c_{\gamma_n}, d_{\gamma_n})$ are related by the transfer-matrix M [11]:

$$\begin{pmatrix} a_{\gamma_n} \\ b_{\gamma_n} \end{pmatrix} = M^{(\gamma_n)} \begin{pmatrix} c_{\gamma_n} \\ d_{\gamma_n} \end{pmatrix}. \quad (5)$$

The elements of the M-matrix are

$$M^{(\gamma_n)} = \begin{pmatrix} 1/t_{\gamma_n} & r_{\gamma_n}/t_{\gamma_n} \\ r^*_{\gamma_n}/t^*_{\gamma_n} & 1/t^*_{\gamma_n} \end{pmatrix}, \quad (6)$$

$t_{\gamma_n}(r_{\gamma_n})$ is the transmission (reflection) amplitude for the potential placed in the edge γ_n. Using the relations (4), (5) and hermiticity condition one get:

$$\Gamma^{(1,\gamma_n)} = \frac{1}{\zeta-\zeta^*}\begin{pmatrix} \zeta & -1 \\ -\zeta^* & 1 \end{pmatrix}, \text{where}$$
$$\zeta = \exp(-ik\xi_{v_{n+1}})M_{11}^{(\gamma_n)} - \exp(ik\xi_{v_{n+1}})M_{12}^{(\gamma_n)}. \quad (7)$$

From (4), (5) it follows

$$\Gamma^{(2,\gamma_n)} = [M^{(\gamma_n)}]^{-1}\Gamma^{(1,\gamma_n)}. \quad (8)$$

Finally, (4), (7), (8) together with the hermiticity condition lead to the system of linear equation for unknown vector Ψ. Finding the Ψ solves the transport problem for graph because the wave functions ψ_{in}, ψ_{out} satisfy the following conditions at the in,out-vertices:

$$1 + r(k) = \Psi_{in}, \quad t(k) = \Psi_{out}. \quad (9)$$

3. PARALLEL COUPLED QUANTUM WELLS

Let us consider the interesting system of parallel coupled quantum wells. The problem of ballistic transport in the system of n parallel coupled quantum wells (see the Figure 1) can be easily solved using the proposed vertex amplitudes method.

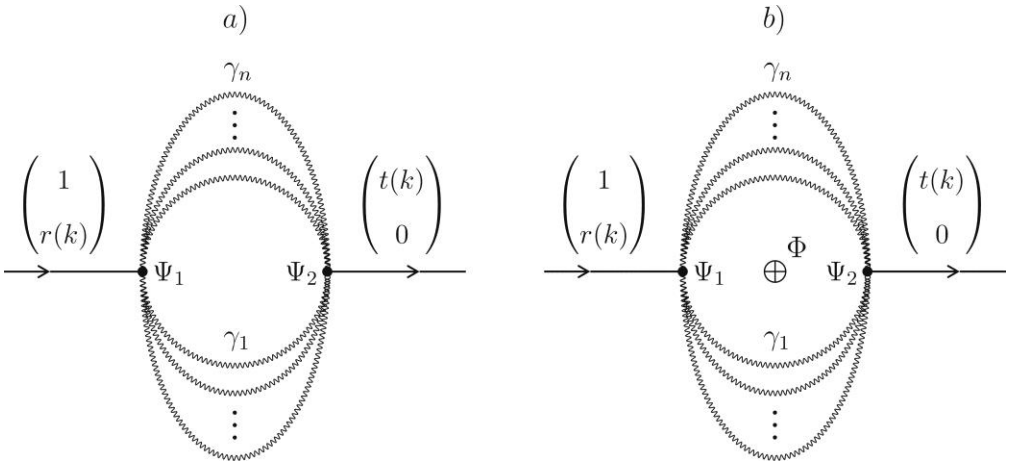

Figure 1. Panel a): The graph that corresponds to the scattering problem in the system of n parallel coupled quantum wells. Wavy line represents the potential (in the considered case the potential is the rectangular quantum well). Panel b): the same as in panel a) but with the non-zero AB flux.

The transmission and reflection amplitudes can be found using the vertex amplitudes method. Namely, for the transmission amplitude we get:

$$t_n(k) = \frac{2ikq}{(k^2+n^2q^2)\sin ql + 2ikq\cos ql}. \quad (10)$$

Here $q = \sqrt{k^2 - V}$, $V = 2m_e U/\hbar^2$, U is the well's depth and l is the well's width, n is a number of quantum wells in a system. As it should be, at $n = 1$ this expression turns in to the standard expression for the scattering amplitude for the single one-dimensional quantum well. Using (10) we can analyze the dependence of the energy spectrum and transmission coefficient of such a system on the number of connected quantum wells. In order to do this, let us recall that energies of bound states correspond to the simple poles of the transmission amplitude [12, 13]. In order to determine the bound states energies construct the analytic continuation of the transmission amplitude $t(i\kappa)$. The bound states are placed in the half-line $\Im k > 0$.

In the case of identical quantum wells that contain two bound states $E_1 = \frac{\hbar^2\kappa_1^2}{2m_e} \approx -0.099\,\text{eV}$ and $E_2 = \frac{\hbar^2\kappa_2^2}{2m_e} \approx -0.734\,\text{eV}$ (the parameters of wells are $U_0 = -1,\text{eV}$ and $l = 3 \times 10^{-7}$ cm) the results for the bound states positions are presented in the Figure 2.

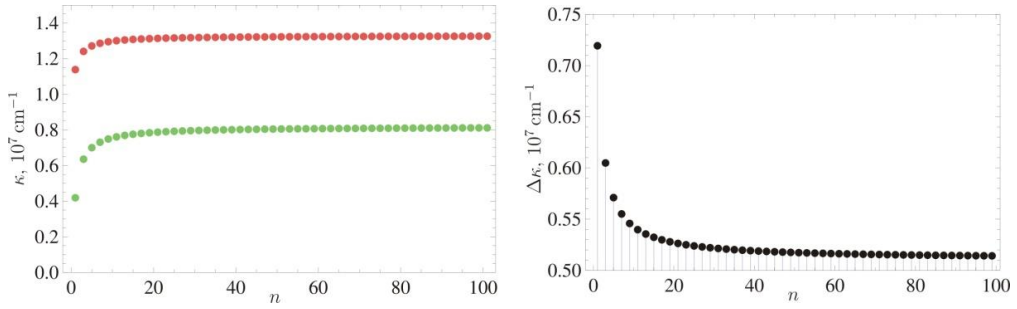

Figure 2. Left panel: the dependence of the bound states positions in the system of parallel coupled quantum wells on the number of wells n; the parameters of wells are $U_0 = -1$ eV and $l = 3 \times 10^{-7}$ cm; the parameters of wells are chosen so that each of them contains two bound states only with the energies equal to $E_1 \approx -0.099$ eV and $E_2 \approx -0.734$ eV; red points correspond to the top bound state E_1, green points correspond to the bottom bound state E_2. Right panel: the dependence of the difference $\Delta\kappa = \kappa_1 - \kappa_2$ (the distance between the bound states) on the number of wells n in the system.

As it can be seen from this figure the new bound states in such a system will not appear just only shift to some limiting positions. More clearly this result is presented in the left panel of Figure 2. Also in Figure 2 (right panel) we show that the distance between the bound states $\Delta\kappa = \kappa_1 - \kappa_2$ in such a system decreases when the number of quantum wells increases. We can conclude that the number of wells in such a system can be considered as a driven parameter for the bound states positions as well as for the distance between the bound states. As a result, the characteristics of the system under consideration, e.g., the optical properties (namely, the frequencies of laser transitions), can be changed by addition of new wells only.

In the case when the AB flux at origin of such a system takes place the explicit expression for the transmission amplitude (in the case of identical wells) can be obtained in the following form[2] (for details see [9]):

$$t_n(k) = \frac{4ikq \sin(ql)\cos\left(\frac{\alpha}{2n}\right)}{(2nq)^2\cos^2\left(\frac{\alpha}{2n}\right)+k^2\sin^2(ql)(1+2iq\cot(ql))^2}, \tag{11}$$

where (as before) $q = \sqrt{k^2 - V}$, $V = 2m_e U/\hbar^2$, U is the well's depth and l is the well's width, n is a number of quantum wells in a system, α is a dimensionless AB flux. As previously, in order to determine the bound states energies $E_{bound} = -\hbar^2\kappa^2/2m_e$ we construct the analytic continuation of the transmission amplitude $t(i\kappa)$.

In the Figure 3 we present the results of numerical simulations for the logarithm of the transmission coefficient $\ln|t(i\kappa)|^2$ (for various AB fluxes) which determines the bound states positions in the system under consideration.

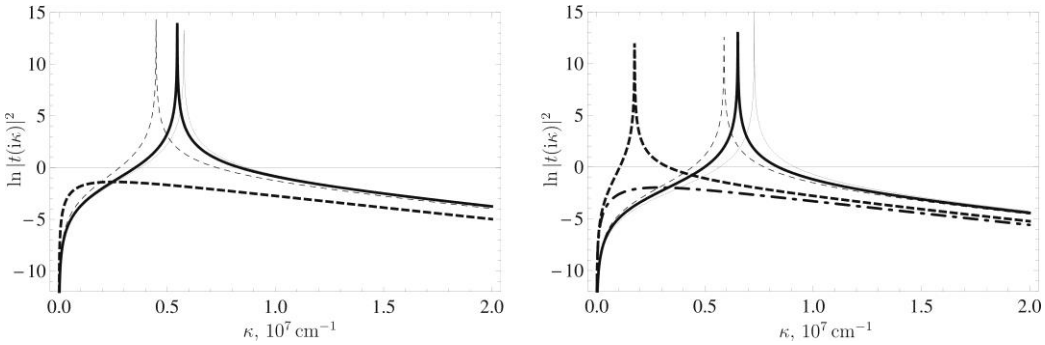

Figure 3. Logarithm of the transmission coefficient $\ln|t(i\kappa)|^2$ for various AB fluxes α in the case of two coupled wells (left panel $n = 2$) and four coupled wells (right panel $n = 4$) as a function of the wave number κ ($k = i\kappa$). Left panel: thin solid line is $\alpha = 0$, thick solid line is $\alpha = 0.5$, thin dashed line is $\alpha = 1$, thick dashed line is $\alpha = 2$; Right panel: thin solid line is $\alpha = 0$, thick solid line is $\alpha = 1.5$, thin dashed line is $\alpha = 2$, thick dashed line is $\alpha = 3.5$, thick dot dashed line is $\alpha = 4$. The parameters of wells are $U = -0.5$ eV and $l = 10^{-7}$ cm.

We see that the presence of the AB flux leads to the fact that the bound state position in such a system becomes dependent on the value of AB flux. As a result also the optical properties that determined by the bound states positions become dependent on the AB flux. Namely for some values of the AB flux the bound state in such a system will not appear due to interference effects. In this paper we present the results for the case when the single well contains single bound state. In the case when the quantum well contains two bound states the positions of these states together with the distance between them depends not only on the number of wells in the system, but also on the value of AB flux (it should be noted also that the distance between the bound states corresponds to THz frequency domain, so the considered system seems promisingly and perspective in connection with development of modern low-dimensional optics). We can conclude that the number of wells in such a system

[2]Here we would like to note that the graph ideology allows to obtain the transmission coefficient not only in the case of identical wells, but in this case only numerical results take place

together with the AB flux can be considered as driven parameters for the bound states positions as well as for the distance between the bound states. These facts open a new way for control of the optical properties of ring-like structures by addition of extra wells in the system, as well as by changing of the magnetic flux through the system.

CONCLUSION

In this paper we have considered a system of parallel coupled quantum wells with the AB flux at origin of such a system. In the case of similar quantum wells the explicit analytic expression for the transmission amplitude is observed and numerically analyzed. In particular, it is shown numerically that changing of wells number in the system (in the the case of identical wells) does not lead to appearance of a new bound states. However, the addition of new wells leads to the fact that the bound states positions in such a system shift to some limiting value determined by the characteristics of a single well.

Addition of the AB flux at origin of such a system leads to the fact that the bound states position become dependent on its values. Moreover, for some values of the AB flux the bound states in such a system will not appear due to quantum interference effects. Thus, we can conclude that the number of quantum wells in the system under consideration together with the AB flux can be considered as driven parameters for the bound states positions as well as for the distance between the bound states. As a result, the optical properties of such a system (frequencies of laser transitions) depend on the number of well as well as on the AB flux. These facts opena new way for control of the optical properties of ring-like structures with quantum wells by addition of extra wells in the system, as well as by changing of the magnetic flux through the system.

REFERENCES

[1] Fuhrer et al., *Nature* 413, 822 (2001).
[2] H. Castro Neto, F. Guinea, N. M. R. Peres, K. S. Novoselov, and A. K. Geim, *Rev.Mod. Phys.* 81, 109 (2009).
[3] M. Suarez, T. Grosjean, D. Charraut, and D. Courjon, Optics Communications 270, 447 (2007).
[4] G. Cohen, O. Hod, and E. Rabani, *Phys. Rev.* B 76, 235120 (2007).
[5] D.-Y. Liu, J.-B. Xia, and Y.-C. Chang, *J. Appl. Phys*. 106, 093705 (2009).
[6] J. Xia, *Phys. Rev. B 45*, 3593 (1992).
[7] Texier and G. Montambaux, *J. Phys. A: Math. Gen*. 34, 10307 (2001).
[8] E. Akkermans, A. Comtet, J. Desbois, G. Montambaux, and C. Texier, *Ann. Phys*. 284, 10 (2000).
[9] A. F. Klinskikh, A.V. Dolgikh, P.A. Meleshenko, and S.A. Sviridov, Arxiv preprint arXiv:1012.3634, 1 (2011).
[10] B. A. Dubrovin, A.T. Fomenko, and S.P. Novikov, *Modern Geometry - Methods and Applications: Part I: The Geometry of Surfaces, Transformation Groups, and Fields*, Springer-Verlag, New-York, 1992.

[11] A. F. Klinskikh, D.A. Chechin, and A.V. Dolgikh, *J. Phys. B: At. Mol. Opt*. 41, 161001 (2008).

[12] L. D. Landau and E.M. Lifshitz, *Quantum mechanics (Nonrelativistic theory)*, Pergamon, Oxford, 1977.

[13] S. P. Novikov, S.V. Manakov, L.P. Pitaevskii, and V.E. Zakharov, *Theory of solitons. The Inverse Scattering Transform Method*, Springer, 1984.

Smart Nanocomposites
Volume 5, Number 2
ISSN: 1949-4823

SYNTHESIS, CHARACTERIZATION AND ANTICANCER ACTIVITY OF SOME TRANSITION METAL COMPLEXES OF NEW SCHIFF BASE TRIAZOLE DERIVATIVES

Nabil S. Youssef[1], Eman A. M. El-Zahany[1], Sayed A. Drweesh[1], Bakr F. Abdel-Wahab[2] and Mamdouh M. Ali[3]

[1]Inorganic Chemistry Department, National Research Centre, Dokki- Giza- Egypt
[2]Applied Organic Chemistry Department, National Research Centre, Dokki- Giza- Egypt-
[3]Biochemistry Department, Division of Genetic Engineering and Biotechnology, National Research Centre, Dokki- Giza- Egypt

ABSTRACT

Two new Schiff base triazole ligands H_2L^1 and H_2L^2 and their Co(II), Ni(II), Cu(II), Zn(II), Fe(III) and Ag(I) metal complexes were synthesized. The ligands and their complexes were characterized by IR, ^{1}H and ^{13}C NMR, UV–vis, mass spectra, and magnetic measurements. The IR spectra show that the ligands H_2L^1 and H_2L^2 are coordinated to the metal ions in a tridentate manner. All the metal (II) complexes possess an octahedral geometry except the Cu(II) complexes which showed a distorted octahedral geometry whereas Ag(I) complexes have tetrahedral structure. The cytotoxicity and the percent of Urokinase (uPA) inhibition of ligands H_2L^1 and H_2L^2 and their metal complexes against three different human cancer cell lines including breast MCF-7, liver HepG2, and lung A549 that may act through uPA inhibition were evaluated. The comparison revealed that ligand H_2L^2 and its complexes have cytotoxicity more than that of ligand H_2L^1 and its complexes in the three tested kinds cell lines which may be attributed to the presence of the extra methyl group in ligand H_2L^2.

Keywords: 1,2,3-Triazoles, transition metal complexes, cancer cells, urokinase

1. INTRODUCTION

Cancer, being one of the leading causes of death globally, causes almost 8 million people death each year and possess a major socioeconomic hazard to humanity at large. Among all factors resulting in the ultimate failure of cancer treatment, drug resistance is a significant player [1]. There is general belief that agents modulating more than one target could have

superior efficiency compared to single target drugs [2]. Development of new molecules with novel mechanisms of action to fight cancer are urgently needed as most anticancer drugs are ineffective due to drug resistance [3].

Urokinase is implicated in cancer invasion and metastatization, its expression has been elevated in a large number of malignancies, e.g., cancers of breast, lung, bladder, cervix, kidney, stomach and brain [4, 5].

Over the past few years, 1,2,3-Triazoles have occupied an important role not only inorganic chemistry but also in medicinal chemistry due to their easy synthesis by click chemistry and attractive features as well as numerous biological activities [6]. Moreover, 1,2,3-Triazole is one of the key structural units found in a large variety of bioactive molecules as anti-fungal [7], antibacterial [8] anti-allergic [9], anti-HIV [10], anti-tubercular [11] and anti-inflammatory agents [12]. In recent years, people are increasingly focused on their anticancer activity [11].

By combining 1,2,3-triazole with other pharmacophores via click chemistry, a number of compounds with potent antitumor activity were synthesized [3, 14]. They are also used as intermediates in the synthesis of antibiotics (e.g., Tazobactum) [15] and applied as agrochemicals mainly as fungicides [16] insecticides [17] and plant growth regulators. [18]. They have practical use in industrial applications as dyes, corrosion inhibitors (of copper and copper alloys), photo stabilizers and in photographic materials [19]. Recently, alkylating agents have been extensively studied with regard to cancer chemotherapy, this has led to the development of many new and more selective alkylating agents like some molecules based on triazole moiety as anticancer drugs [20].

It is evident that the azomethine linkage (C=N) is an essential structural requirement for biological activity [21]. Several azomethine group containing compounds have been reported to possess remarkable antibacterial [22], antifungal [23] and anticancer activities [24]. In view of above mention, biological behavior of triazole and azomethine linkage (C=N) many triazole based Schiff bases have also been reported to possess antibacterial [25] antifungal [26], antitumor [27], plant growth regulating [28] and cytotoxic activities [29]. Metallo-organic chemistry is becoming an emerging area of research due to the demand for new metal based antibacterial and antifungal compounds [29-30].

In view of the significant structural and biological applications of triazole complexes, we report here the synthesis of a new class of triazole Schiff base derivatives H_2L^1 and H_2L^2 and their silver(I), copper(II) iron(III), cobalt(II), nickel(II) and zinc(II) metal complexes.

2. EXPERIMENTAL

2.1. Materials

All the reagents employed for the preparation of the ligands and their complexes were of the best grade available and used without further purification. They include salicylaldehyde, 2-hydroxyaceteophenone, silver(I) nitrate $AgNO_3$, copper(II) acetate ($Cu(CH_3COO)_2$), nickel(II) chloride hexahydrate $NiCl_2 \cdot 6H_2O$, ferric(III) chloride $FeCl_3$**,** cobalt(II) sulfate hexahydrate $CoSO_4.6H_2O$, zinc acetate dihydrate $Zn(CH_3COO)_2.2H_2O$.

2.2. Physical Measurements

The H_2L^1 and H_2L^2 ligands and their metal complexes were analyzed for C, H, N, and metal contents at the Micro Analytical Laboratory, Faculty of Science, Cairo University, Egypt. Analytical and physical data of the ligands and their metal complexes are reported in Table 1. The metal ion contents of the complexes were also determined by the previously reported methods [31]. IR spectra of the ligands and their metal complexes were measured using KBr discs with a Jasco FT/IR 300E Fourier transform infrared spectrophotometer covering the range 400-4000 cm^{-1}at the central Laboratory, National Research centre, Dokki, Egypt. The electronic spectra of the ligand and its complexes were obtained in Nujol mulls using a Shimadzu UV–240 UV–Vis recording spectrophotometer at the central Laboratory, National Research Centre, Dokki, Egypt. ^{1}H and ^{13}C NMR spectra were obtained on Brucker Avance 300-DRX or Avance 400-DRX spectrometers. Chemical shifts (ppm) are reported relative to TMS. Molar conductivities of the metal complexes in DMSO (10^{-3} M) were measured using a dip cell and a Bibby conductimeter MC1 at room temperature. The resistance measured in ohms and the molar conductivities were calculated according to the equation: $\Lambda = V \times K \times Mw/g \times \Omega$, where Λ, molar conductivity ($ohm^{-1}\ cm^2\ mol^{-1}$); V, volume of the complex solution (mL); K, cell constant 0.92 cm^{-1}; Mw, molecular weight of the complex; g, weight of the complex; and Ω, resistance measured in ohms. Magnetic susceptibilities were measured at 25^{o}C by the Gouy method using mercuric tetrathiocyanatocobaltate (II) as the magnetic susceptibility standard. Diamagnetic corrections were estimated from Pascal's constant [32]. The magnetic moments were calculated from the equation: $\mu_{eff.} = 2.84\sqrt{\chi_M^{corr}.T}$. Mass spectra of the ligand in the solid form was recorded using JEUL JMS-AX-500 mass spectrometer.

2.3. Synthesis of the Ligands

The H_2L^1 ligand, *N*'-(2-hydroxybenzylidene)-5-methyl-1-phenyl-1*H*-1,2,3-triazole-4-carbohydrazide and H_2L^2 ligand, *N*'-(1-(2-hydroxyphenyl)ethylidene)-5-methyl-1-phenyl-1*H*-1,2,3-triazole-4-carbohydrazide were prepared. A mixture of 5-methyl-1-phenyl-1*H*-1,2,3-triazole-4-carbohydrazide (2.17 g, 10 mmol) in ethanol (100 cm^3), salicylaldehyde or 2-hydroxyaceteophenone (12 mmol), and a few drops of glacial acetic acid were refluxed for 4h. The resulting solid product was filtered off and dried (Scheme 1).

2.4. Synthesis of the Metal Complexes

The metal complexes of the ligands H_2L^1 and H_2L^2 were prepared by dissolving the required amount of the ligands in mixture of MeOH/DMF (10/20 ml) and then mixing with the methanol solution of the required amount of the metal salt to form 1:1 or 1:2 M/L (metal/ligand) complexes. The reaction mixture was then heated for few minutes. The precipitates formed were filtered off, washed with ethanol, then with diethyl ether and dried under vacuum at 50 ^{o}C for 5 h. The analytical data for the ligands and their complexes are given in Table 1.

Table 1. Analytical and physical data of the ligands H_2L^1& H_2L^2 and their metal complexes

No.	Ligands/Complexes	Color	FW	Yield (%)	Anal./found (calc.) (%)				Molar conductance Λm (Ω^{-1} cm^2 mol^{-1})
					C	H	N	M	
1	H_2L^1, $C_{17}H_{15}N_5O_2$	colorless	321.33	75	63.4 (63.5)	4.8 (4.7)	22.3 (21.8)	-	-
2	$(HL^1)_2Cu$ $C_{34}H_{28}CuN_{10}O_4$	green	704.2	60	57.5 (58.0)	4.4 (4.0)	19.4 (19.9)	9.1 (9.0)	16
3	$[H_2L^1FeCl_3].3H_2O$ $C_{17}H_{21}Cl_3FeN_5O_5$	brown	537.6	65	34.4 (38.0)	3.6 (3.9)	13.4 (13.0)	10.1 (10.4)	15
4	$[HL^1NiCl(H_2O)_2]$ $C_{17}H_{18}ClN_5NiO_4$	green	450.5	75	45.8 (45.3)	4.1 (4.0)	16.0 (15.5)	13.2 (13.0)	19
5	$H_2L^1Ag(H_2O)$ $C_{17}H_{16}AgN_5O_3$	Grey	446.2	70	45.3 (45.7)	3.1 (3.6)	15.9 (15.7)	24.0 (24.2)	18
6	$[(H_2L^1)_2Zn]Cl_2.2H_2O$ $C_{34}H_{34}Cl_2N_{10}O_6Zn$	yellow	815.0	75	50.5 (50.1)	3.8 (4.2)	17.3 (17.2)	8.2 (8.0)	70
7	$(HL^1)_2Co$ $C_{34}H_{28}CoN_{10}O_4$	brown	699.6	65	58.1 (58.6)	4.5 (4.0)	19.8 (20.0)	8.9 (8.4)	12
8	H_2L^2, $C_{18}H_{17}N_5O_2$	colorless	335.36	80	64.0 (64.5)	4.8 (5.1)	20.5 (20.9)	-	-
9	$H_2L^2Ag(H_2O)$ $C_{18}H_{18}AgN_5O_3$	Grey	460.2	70	47.5 (47.0)	4.0 (3.9)	15.5 (15.2)	23.1 (23.4)	25
10	$[(H_2L^2)_2Cu].2H_2O.2OAc$ $C_{40}H_{44}CuN_{10}O_{10}$	green	888.4	65	54.5 (54.0)	4.6 (5.0)	15.5 (15.8)	7.0 (7.1)	86
11	$[(H_2L^2)_2Fe]Cl_3.3H_2O$ $C_{36}H_{40}Cl_3FeN_{10}O_7$	brown	888.9	60	48.0 (48.5)	4.6 (4.5)	15.5 (15.8)	6.0 (6.3)	88
12	$[(H_2L^2)_2Zn].2OAc$ $C_{40}H_{40}N_{10}O_8Zn$	yellow	854.2	60	56.0 (56.2	4.6 (4.7)	16.5 (16.4)	8.0 (7.6)	82
13	$[H_2L^2Co(H_2O)].SO_4$ $C_{18}H_{19}CoN_5O_7S$	brown	508.4	65	42.0 (42.5)	3.6 (3.8)	13.5 (13.8)	11.0 (11.6)	95

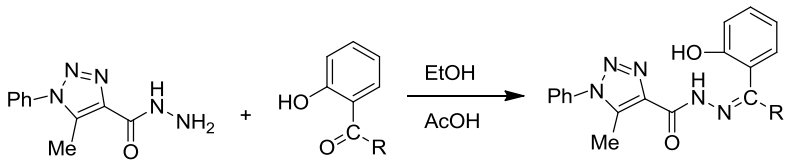

H_2L^1: R = H

H_2L^2: R = Me

Scheme 1. Schematic representation for the formation of the H2L1 and H2L2 ligands.

2.5. Biological Evaluation

2.5.1. Chemicals

Fetal bovine serum (FBS) and L-glutamine, were obtained from Gibco Invitrogen Company (Scotland, UK). Dulbecco's modified Eagle's (DMEM) medium was provided from Cambrex (New Jersey, USA). Dimethyl sulfoxide (DMSO), doxorubicin, penicillin, and streptomycin were obtained from Sigma Chemical Company (Saint Louis, MO, USA).

2.5.2. Cell lines and Culturing

Anticancer activity screening for the tested complexes utilizing 3 different human tumor cell lines including breast cancer cell line MCF-7, liver cancer cell line HepG2, and lung carcinoma cell line A549 were obtained from the American Type Culture Collection (Rockville, MD, USA). The tumor cells were maintained in Dulbecco's modified Eagle's medium (DMEM) supplemented with 10% heat inactivated fetal calf serum (GIBCO), penicillin (100 U/ml) and streptomycin (100µg/ml) at 37 ^{o}C in humidified atmosphere containing 5% CO_2. Cells at a concentration of 0.50 x 10^6 were grown in a 25 cm^2 flask in 5ml of complete culture medium.

2.5.3. In Vitro Cytotoxicity Assay

The cytotoxicity was measured in vitro using the Sulfo-Rhodamine-B stain (SRB) assay according to the previous reported standard procedure [33]. Cells were inoculated in 96-well microtiter plate (10^4 cells/well) for 24 h before treatment with the tested complexes to allow attachment of cell to the wall of the plate. The tested complexes were dissolved in DMSO at 1 mg/ml immediately before use and diluted to the appropriate volume just before addition to the cell culture. Different concentrations of tested complexes and doxorubicin were added to the cells.

Triplicate wells were prepared for each individual dose. Monolayer cells were incubated with the complexes for 48 h. at 37 °C and in atmosphere of 5% CO_2. After 48 h cells were fixed, washed, and stained for 30 min with 0.4% (w/v) SRB dissolved in 1% acetic acid. Unbound dye was removed by four washes with 1% acetic acid, and attached stain was recovered with Tris-EDTA buffer. Color intensity was measured in an ELISA reader. The relation between surviving fraction and drug concentration is plotted to get the survival curve for each cell line after the specified time. The concentration required for 50% inhibition of cell viability (IC_{50}) was calculated and the results are given in Table (5). The results were compared to the antiproliferative effects of the reference control doxorubicin [34].

2.5.4. Determination of the Level of uPA Expression

The expression of uPA protein was determined using Assay Max human urokinase (uPA) ELISA kit (Assaypro, USA) according to manufacturer's instructions. The complexes and standard drug, doxorubicin were incubated for 48 h with MCF-7, HepG2 and A549 cells at concentration of 1/10 of the IC_{50} values of each complex, then the cells were collected and centrifuged at 2000 xg for 10 min, 50 µl of the cell extracts were added to each well of ELISA plate and incubated for 2 h. Wells were washed with 200 µl of washing buffer then 50 µl of biotinylated uPA antibody were added to each well and incubate for 1 h at 25 ºC. After washing, plate was incubated with 50 µl of streptavidin-peroxidase conjugate per well for 30 min then washed. 50 µl of chromogen were added to each well and incubate for about 10 min, then 50 µl of stop solution were added to each well. The color will change from blue to yellow. Read the absorbance on a microplate reader at a wavelength of 450 nm immediately and the concentrations of uPA were determined.

2.5.5. Statistical Analysis

The results are reported as Mean ± Standard error (S.E.) for at least three times experiments.

3. RESULTS AND DISCUSSION

3.1. Elemental Analysis

The elemental and physical data of the ligands H_2L^1 and H_2L^2 and their complexes (Table 1) showed that the stoichiometry of the complexes obtained is either 1:1 or 1:2 M/L.

3.2. Mass Spectra of the Ligands

The mass spectra of the free ligands H_2L^1 and H_2L^2 (Figure 1) exhibit the molecular ion peaks at *m/e* 321.33 and 335.36, respectively, which confirm their proposed formulae. Their suggested pathway fragmentation patterns are described (Scheme 2 and 3).

3.3. Conductivity Measurements

The molar conductance values of 10^{-3} M solution of the metal complexes in DMSO calculated at room temperature in the range (10-95) Ω^{-1} cm^2 mol^{-1} are listed in Table 1. The non-electrolytic nature of the metal complexes 2, 3, 4, 5, 7 and 9 was confirmed by the low molar conductance values [35] while complexes 6 and 10-13 behaved as electrolytes [36].

3.4. Infrared Spectra

The significant IR bands of the ligands H_2L^1 and H_2L^2 and their metal complexes are given in Table (2). The IR spectra of the complexes are compared with those of their free ligands in order to determine the coordination sites that may be involved in chelation. The

bands around 3424-3370, 3205-3054, 1692-1688, 1645-1603 and 1218 cm^{-1} in the free ligands H_2L^1 and H_2L^2 are assigned to $\nu OH_{(phenolic\ and\ H2O)}$, νNH, $\nu C{=}O$, $\nu C{=}N$ and $\nu C{-}O_{(phenolic\ group)}$, respectively.

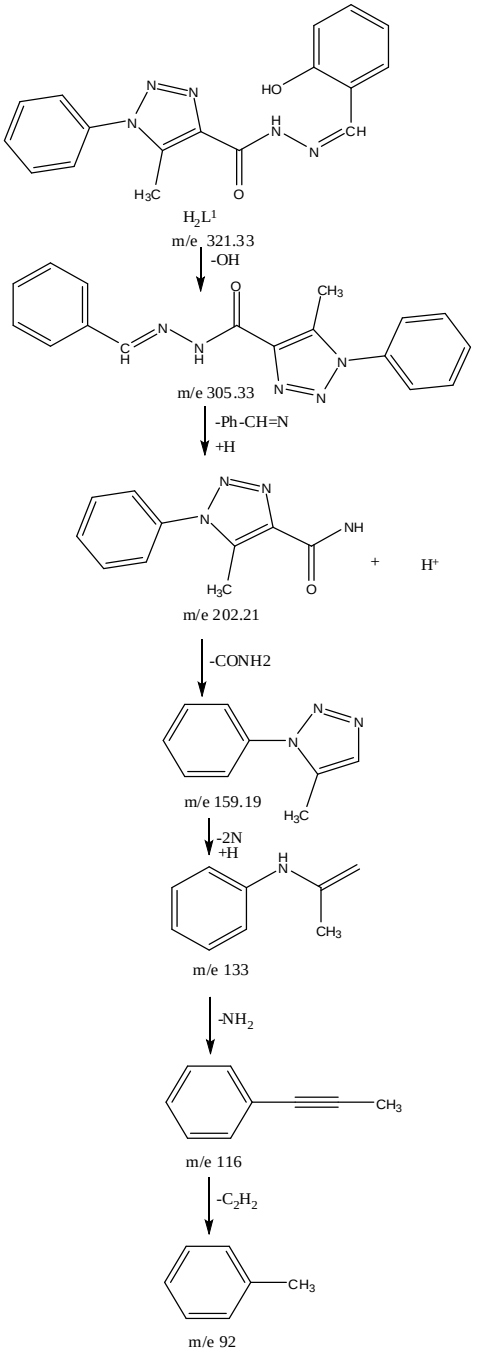

Scheme 2. The pathway fragmentation pattern of the mass spectrum of the H2L1 ligand.

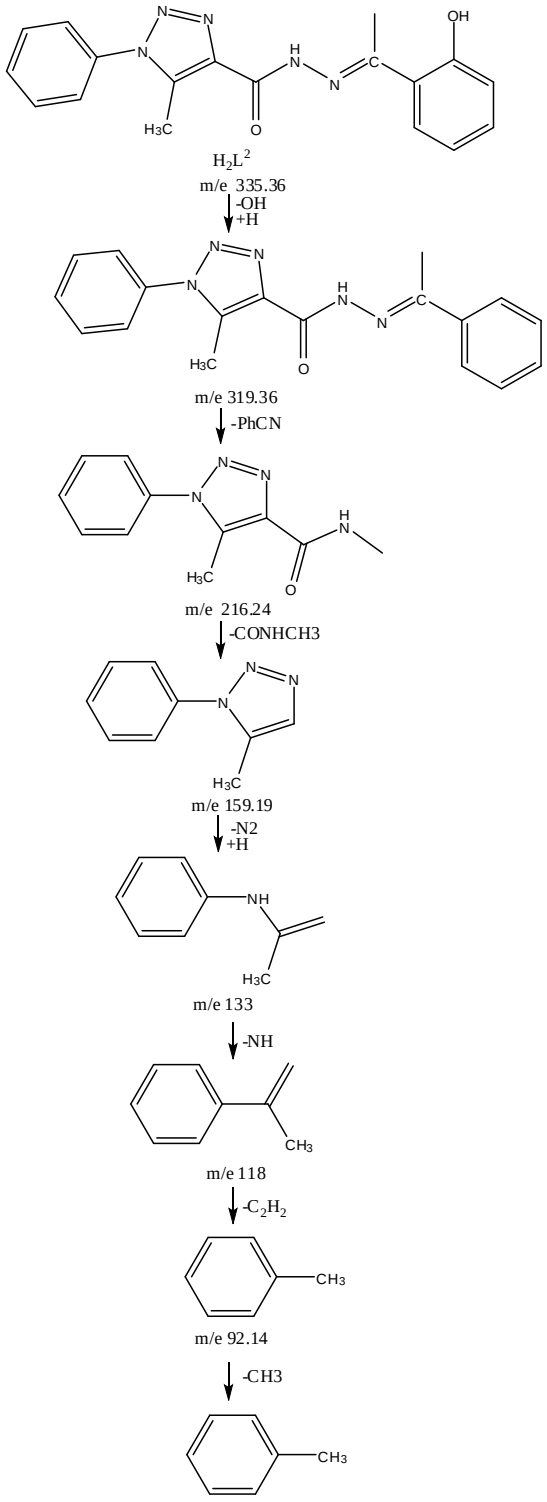

Scheme 3. The pathway fragmentation pattern of the mass spectrum of the H2L2 ligand.

Table 2. IR frequencies of the bands (cm^{-1}) of the ligands H_2L^1& H_2L^2 and their metal complexes and their assignments

No	Ligand /Complex	ν(OH) $_{phenolic}$ + H_2O	ν(NH)	ν(C=O)	ν(C=N)	ν_s(COO), ν_{as}(COO), or SO_4	(C-O) $_{Phenolic}$
1	H_2L^1	3376	3205	1692	1645	-	1218
2	$(H_2L^1)_2$ Cu	3412br	3200	1677	1617	-	1197
3	$[H_2L^1FeCl_3].3H_2O$	3410	3219	1675	1611	-	1215w
4	$HL^1NiCl(H_2O)_2$	3404	3200	1678	1618	-	1208
5	$H_2L^1Ag(H_2O)$	3442	3195	1675sh	1633	-	1210w
6	$[(H_2L^1)_2Zn]Cl_2.2H_2O$	3427	3200	1670	1619	-	1213w
7	$(HL^1)_2Co$	-	3220	1680	1631	-	1199
8	H_2L^2	3370	3054	1688	1613	-	1218s
9	$H_2L^2Ag(H_2O)$	3472	-	1600	1597	-	1211vw
10	$[(H_2L^2)_2Cu].2H_2O.2OAc$	3425	3056	1655	1597	1549 1441	1217vw
11	$[(H_2L^2)_2Fe]Cl_3.3H_2O$	3400	3052	1696vw	1595	-	1218w
12	$[(H_2L^2)_2Zn].2OAc$	3409	3054	1653	1598	1525 1393	1215w
13	$[H_2L^2Co(H_2O)].SO_4$	3428	3285	1696vw	1598	1199	1220w

These bands are shifted or weakened upon complexation with copper, iron, nickel, silver, zinc and cobalt ions, indicating the participation of C=O, C=N and oxygen of C–O phenolic group. This behavior was proved by: (i) the shift of (C=O) band to lower or higher frequencies (12-22, 8-35 cm^{-1}). (ii) the shift of (C=N) to lower frequency together with its weak appearance (12-34, 15-18 cm-1), (iii) The bands of the triazole ring (1276 and 1146), (1218 and 1088) in the free ligands H_2L^1 and H_2L^2, respectively are found almost at the same frequencies for all complexes, which suggest the non participation of triazole ring in complexation. (iv) The disappearance of ν(OH) band of the free ligand H_2L^1 found around 3424 and 3376 cm^{-1} in the spectra of all complexes except complexes 3 and 6 indicating the deprotonation of ligand prior to coordination. On the other hand, the ν(C–O), which found at 1218 cm^{-1} for the ligand was moved to lower frequencies, in case of complexes 2, 4, 5 and 7 after complexation, this shift confirms the participation of phenolic oxygen of the ligand in C–O–M bond formation [37]. In case of the H_2L^2 ligand the weakness of the band due to phenolic group C–O in all of its complexes except complex 9 confirms the participation of phenolic oxygen of the ligand bond formation without deprotonation [38].

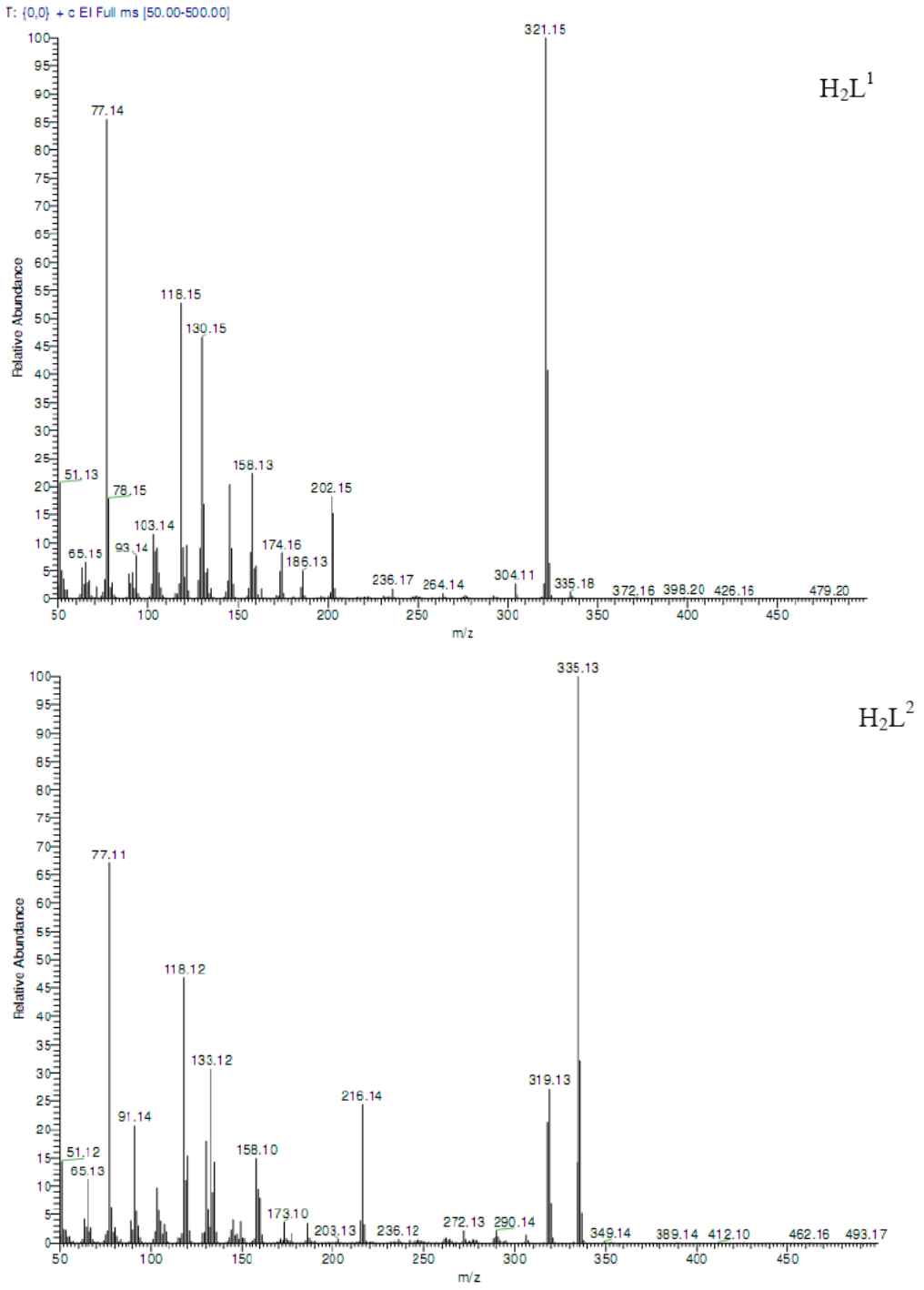

Figure 1. Mass spectra of the H2L1 and H2L2 ligands.

The spectra of complexes 10 and 12 showed the appearance of two characteristic bands at (1549 and 1441) cm^{-1} and (1525 and 1393) cm^{-1} attributable to asym (OCO) and sym (OCO), respectively, having the separation value Δ(OCO) 108 and 132 cm^{-1}, respectively, suggesting

the ionic nature of the acetate [39]. Also, the spectrum of the cobalt complex 13 shows a new sharp band at 1099 cm^{-1} indicating the presence of ionic behavior or uncoordinated sulphate group [40].

3.5. ^{1}H and ^{13}C NMR Spectra

The ^{1}H and ^{13}C NMR spectral information are reported along with their possible assignments in Table (3). The ^{1}H NMR spectra of the ligands H_2L^{1} and H_2L^{2} exhibit signals at 10. 57, 13.12 and 9.76, 11.40 ppm due to hydrazine NH and phenolic –OH protons, respectively. Multiplet is observed at 7.12-7.52 and 6.90-7.67 ppm due to aromatic protons in $H_2L^{1}$and H_2L^{2}, respectively. In silver(I) complexes (5 and 9) the phenolic protons disappeared; this confirms that the hydroxyl group reacted with metal ion via deprotonation. In zinc(II) complexes (6 and 12) the phenolic protons signal shifts downfield due to the coordination of the phenolic protons to central metal ion without deprotonation [41].

The ^{13}C NMR spectra of the ligands H_2L^{1}, H_2L^{2} and their complexes were taken in DMSO-d^6. The ^{13}C NMR spectra of the ligands displayed the C=O carbon at 161.4-162.1 [42] and carbons of the phenyl group appeared at 115.7–159.1 and 117.8-158.9 ppm in the ligands H_2L^{1} and H_2L^{2}, respectively. The phenyl carbon (C1) of these ligands were observed downfield in the region 158.9-159.1 ppm, due to attachment of hydroxyl (OH) group [30b]. The azomethine carbon (CH=N) appeared at 140.7–141.5 ppm in the ligands H_2L^{1}, H_2L^{2} [43]. In the spectra of Zn(II) and Ag(I) complexes of the ligands H_2L^{1}, H_2L^{2} the shifting of carbonyl group carbon, carbons of phenyl group (–C–OH), and azomethine carbon (–C=N) indicated the involvement of these groups in coordination to zinc or silver ions, respectively. The results of these studies were found to be in agreement with those of IR and ^{1}H NMR spectra of these complexes.

Table 3. ^{1}H and ^{13}C NMR spectra of the ligands H_2L^{1} and H_2L^{2} signals (δ, ppm) and their assignments recorded in DMSO d^6 solution

No	Ligand/ complex	^{1}H NMR			^{13}C NMR		
		NH	–OH	Aromatic	C=O	–C–OH	C=N
1	H_2L^{1}	10. 57	13.12	7.12–7.52	161.4	159.1	140.7
5	$H_2L^{1}Ag(H_2O)$	11.20	-	7.01-7.35	159.5	159.9	142.5
6	$[(H_2L^{1})_2Zn]Cl_2.2H_2O$	10.85	13.41	7.15-7.62	160.3	159.6	141.2
8	H_2L^{2}	9.76	11.40	6.90 -7.67	162.1	158.9	141.5
9	$H_2L^{2}Ag(H_2O)$	10.25	-	7.11-7.85	161. 6	159.3	142.0
12	$[(H_2L^{2})_2Zn].2OAc$	10.13	11.85	7. 32 -7.75	161.4	159.2	141.9

3.6. Electronic Spectra and Magnetic Moments

The UV-Vis spectral data of the ligands and their metal complexes in DMSO solution are given in Table 4. The absorption spectra of the ligands are characterized mainly by absorption bands in the region 290-394 nm which may be assigned to $\pi \rightarrow \pi^*$ and $n \rightarrow \pi^*$.

The electronic spectra of Fe(III) complexes 3 and 11 exhibit bands at 415 and 416 nm which may be assigned to the $^6A_1g \rightarrow T_2g(G)$ transition in octahedral geometry of the complexes. Also, the $^6A_1g \rightarrow {}^5T_1g$ transition appears at 630 and 635 nm, respectively. The observed magnetic moments of Fe(III) complexes are 5.4 and 5.6 B.M. indicating octahedral geometry [44].

The electronic absorption spectra of the Co(II) complexes 7 and 13 showed a band at 426 and 450 nm, respectively assigned to the transition $^4T_1g(F) \rightarrow {}^4T_1g(P)$ suggesting octahedral structure around Co(II) ion [45]. The magnetic moment values of Co(II) complexes 7 and 13, have been found to be 4.91 and 4.85 BM. respectively, showing three unpaired electrons which are within the range of values corresponding to high spin (sp^3d^2 structure) octahedral complexes of Co(II) ion [46]. This indicates that these complexes are monomeric in nature and there are no metal-metal interactions.

Table 4. The electronic absorption spectral bands (nm) and magnetic moment (B.M.) for the ligands H_2L^1 & H_2L^2 and their metal complexes

No	Ligand/ complex	λ_{max} (nm)	d-d bands and CT	μ_{eff} in BM
1	H_2L^1	300, 317, 360	-	-
2	$(H_2L^1)_2$ Cu	317, 400	540,467	1.76
3	$[H_2L^1FeCl_3].3H_2O$	321, 400	640,423	5.4
4	$HL^1NiCl(H_2O)_2$	280, 320, 400	435	3.3
5	$H_2L^1Ag(H_2O)$	300, 317, 360	-	diamagnetic
6	$[(H_2L^1)_2Zn]Cl_2.2H_2O$	316, 400	431	diamagnetic
7	$(HL^1)_2Co$	312, 401	560, 426	4.91
8	H_2L^2	290, 302, 336	-	-
9	$H_2L^2Ag(H_2O)$	315, 367	-	diamagnetic
10	$[(H_2L^2)_2Cu]2OAc.2H_2O$	318, 400	475, 590	1.85
11	$[(H_2L^2)_2Fe]Cl_3.3H_2O$	318, 400	635	5.6
12	$[(H_2L^2)_2Zn].2OAc$	292, 323, 400	-	diamagnetic
13	$[H_2L^2Co(H_2O)].SO_4$	315, 400	450	4.85

The electronic spectra of copper(II) complexes 2 and 10, display a band at 540 and 590 nm, respectively has been assigned to $^2Eg \rightarrow {}^2T_2g$ transitions suggesting a distorted octahedral environment. The distortion may be due to Jahn Teller effect. The bands of copper complexes 3 and 11 at 467 and 475 nm, respectively refer to a charge transfer band [47]. The

magnetic moments of the copper complexes 2 and 10 at room temperature lie in the range 1.76-1.85 B.M. corresponding to one unpaired electron and fall within the range observed for octahedral Cu(II) complexes.

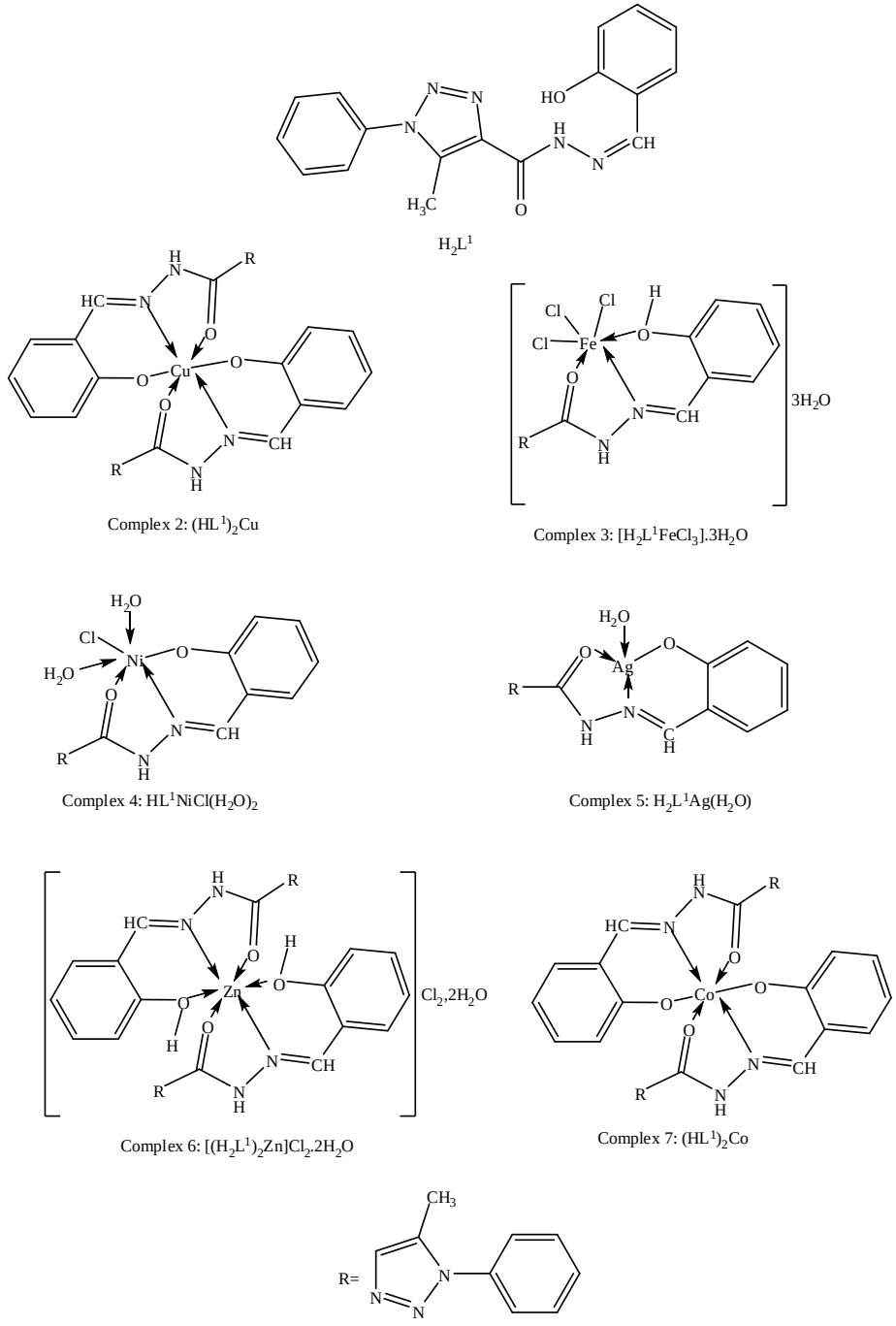

Figure 2. The proposed structures of H2L1 metal complexes.

Also, this indicates that these complexes are monomeric in nature and there are no metal-metal interactions [48].

The broad band at 430 nm in the spectra of Ni(II) complex 4 may be assigned to the $^3A_2g \rightarrow {}^3T_1g(F)$ transition, suggesting octahedral Ni (II) complex. The magnetic moment value for this complex was 3.3 B.M. expected for octahedral nickel complexes [49].

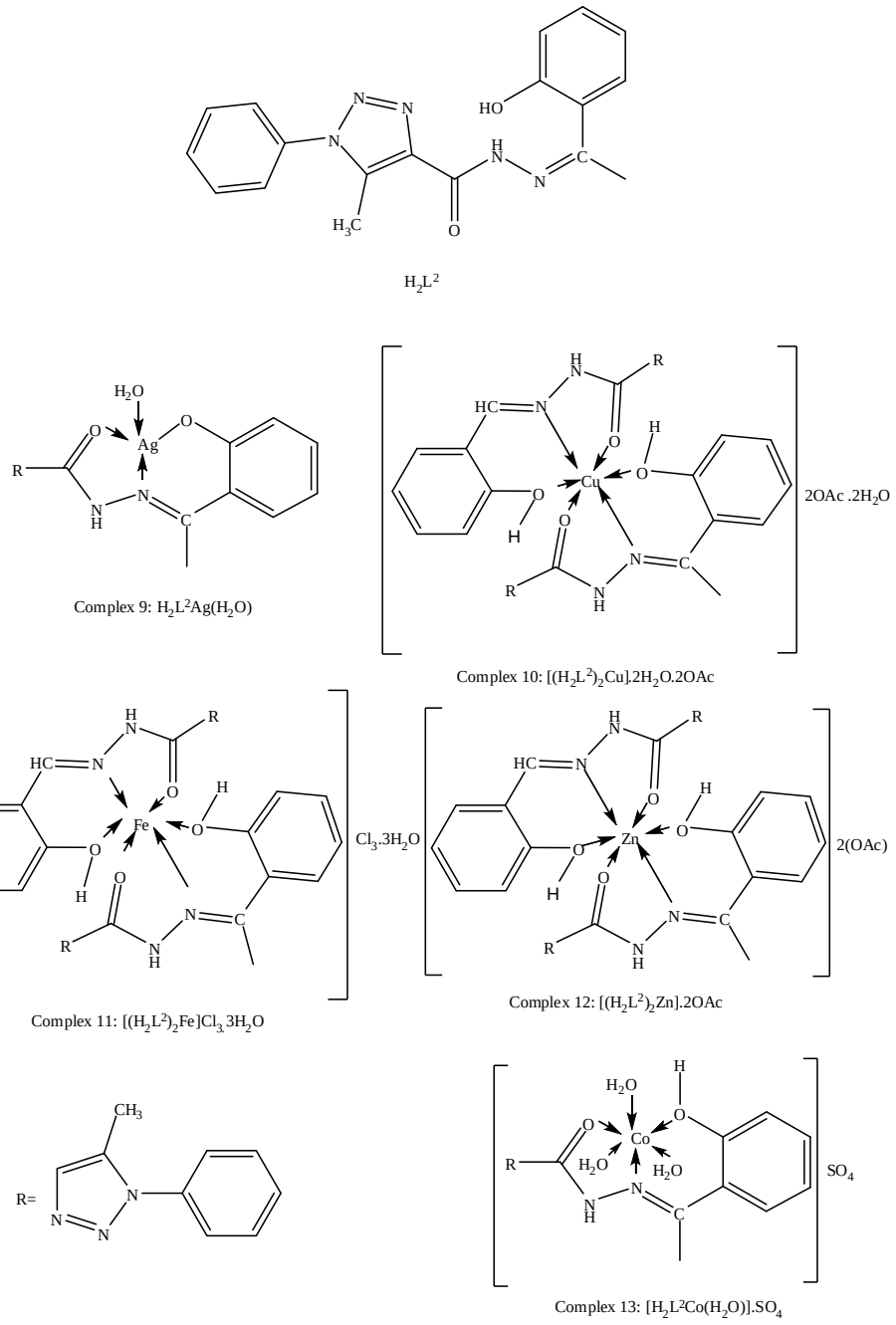

Figure 3. The proposed structures of H2L2 metal complexes.

Table 5. In vitro cytotoxicity activity and the percent of uPA inhibition of the synthesized complexes on different cell lines

No	Ligand/ complex	IC50 (µg/ml)			% of uPA inhibition		
		MCF-7	HepG2	A549	MCF-7	HepG 2	A549
1	H_2L^1	18.60±1.91	21.17±1.82	26.60±2.65	8	N.A.	N.A.
2	$(H_2L^1)_2$ Cu	5.23±045	5.70±0.62	5.96±0.60	55	50	48
3	$[H_2L^1FeCl_3].3H_2O$	N.A.	N.A.	N.A.	N.A.	N.A.	N.A.
4	$HL^1NiCl(H_2O)_2$	3.70±0.29	4.86±0.50	4.45±0.40	76	69	65
5	$H_2L^1Ag(H_2O)$	19.00±1.86	18.34±1.87	43.76±4.60	5	6	N.A.
6	$[(H_2L^1)_2Zn]Cl_2.2H_2O$	3.60±0.26	4.66±0.44	4.11±0.43	80	77	70
7	$(HL^1)_2Co$	4.62±0.37	5.75±0.64	5.90±0.55	68	60	58
8	H_2L^2	9.90±0.86	10.43±1.12	22.27±2.18	16	11	4
9	$H_2L^2Ag(H_2O)$	12.80±1.60	13.60±1.43	29.17±2.80	11	6	N.A.
10	$[(H_2L^2)_2Cu].2H_2O.2OAc$	4.80±0.42	5.33±0.52	5.76±0.60	60	56	54
11	$[(H_2L^2)_2Fe]Cl_3.3H_2O$	N.A.	N.A.	N.A.	N.A.	N.A.	N.A.
12	$[(H_2L^2)_2Zn].2OAc$	2.71±0.19	4.12±0.38	3.72±0.35	85	80	78
13	$[H_2L^2Co(H_2O)].SO_4$	4.18±0.36	5.10±0.47	5.70±0.63	74	64	62
Ref.	Doxorubicin	2.98±0.21	4.20±0.32	3.77±0.34	86	84	81
	DMSO	N.A.	N.A.	N.A.	N.A.	N.A.	N.A.

Data were expressed as Mean ± Standard error (S.E.) of three independent experiments.

N.A. is no activity.

Zn(II) complexes 6, 12 and Ag(I) complexes 5 and 9 do not exhibit d–d electronic transition due to completely filled d-orbital and show absorptions only in the higher frequency region attributed to the ligand electron transitions. According to the elemental analysis and other spectroscopic techniques it is believed that these complexes have a coordination number equal to four as well as six and are likely to be tetrahedral and octahedral structure.

Suggested Structural Formulae of the Complexes

From the spectral data and the elemental analysis, the structure of the prepared complexes may be formulated as shown in Figures 2 and 3.

3.7. Biological Activity

As shown from Table 5, the cytotoxicity of the two ligands H_2L^1, H_2L^2 and their metal complexes was tested using SRB assay as described by Skehan [33] in breast cancer cell line MCF-7, liver cancer cell line HepG2, and lung carcinoma cell line A549. For comparison, doxorubicin was used as reference.

The results showed that:

1. The two ligands and their metal complexes have anticancer activity, in breast cancer cell line MCF-7, liver cancer cell line HepG2, and lung carcinoma cell line A549 except the iron complexes 3 and 6.
2. The metal complexes have more anticancer activity than their parent's ligands. This may be as a result of the change in structure due to coordination and chelating trends to make metal complexes act as more powerful and potent anticancer agents, thus inhibiting the expression of uPA. Moreover, this would suggest that the chelation could facilitate the ability of a complex to cross a cell membrane and can be explained by Tweedy's chelation theory Chelation considerably reduces the polarity of the metal ion mainly because of partial sharing of its positive charge with the donor groups and possible electron delocalization over the whole chelate ring. Such chelation could also enhance the lipophilic character of the central metal atom, which subsequently favours its permeation through the lipid layer of the cell membrane [50].
3. Comparing the studied complexes, revealed that ligand H_2L^2 and its complexes have cytotoxicity more than that of ligand H_2L^1 and its complexes in the three tested kinds cell lines which may be attributed to the presence of the extra methyl group in ligand H_2L^2. Generally, it was found that the presence of groups such as methyl, OH, OCH_3, $COOCH_3$, or $COCH_3$, seems essential for antiproliferative activities [51].
4. The iron complexes 3 and 11 showed no activity while, Zn complexes 6 and 12 have the highest cytotoxic activity in the three cell lines. Also, the Zn complex 12 was more potent than the doxorubicin. The cytotoxic activity shown by this Zn complex 12 against MCF-7, HepG2 and A549 cell lines indicates that coupling of ligand H_2L^2 to Zn(II) metal center results in a metallic complex with important biological properties and remarkable cytotoxic activity, since it displays IC_{50} value better than that of the antitumor drug doxorubicin. Thus, complex 12 is considered as agent with

potential antitumor activity, and can therefore be candidates for further stages of screening in vitro.

It is clear from the data that the activity order of the ligands and their metal complexes follows the order: complex 12 > complex 6 > complex 4 > complex 13 > complex 10 > complex 2 > H_2L^2 > H_2L^1 > complex 9 > complex 5. To identify the mechanism of action responsible for the cytotoxicity of two ligands and their complexes, the expression of uPA protein expressed in the three cell lines (breast MCF-7, HepG2 and A549 cell) was estimated. As shown in Table 5, the uPA expression decreased by the ligand H_2L^1 and its complexes. The percent of uPA expression in the breast cancer cell line MCF-7 is 8, 55, 76, 5, 80 and 68 % in case of complexes 1, 2, 4, 5, 6 and 7, respectively. In HepG2 cell line the percent of uPA expression is 50, 69, 6, 77 and 60 % in case of complexes 2, 4, 5, 6 and 7, respectively. In case of A549 cell line the percent of uPA expression is 48, 65, 70 and 58 % in case of complexes 2, 4, 6 and 7, respectively. Also, in case of ligand H_2L^2 and its complexes, the percent of uPA expression of the breast cancer cell line MCF-7 is 16, 11, 60, 85, 74 and 86 % in complexes 8, 9, 10, 12 and 13, respectively. In case of HepG2 percent of expression is 11, 6, 56, 80, 64 and 84 % in complexes 8, 9, 10, 12 and 13, respectively. In case of the A549 percent of uPA expression is found to be 4, 54, 78, 62 and 81 % in complexes 8, 10, 12 and 13, respectively. Also, the results revealed that iron complexes 3 and 11 have no effect on the expression of uPA in the three cancer cell lines, while complex 12 has the highest activity in the tested complexes, whereas doxorubicin suppress the expression of uPA in breast MCF-7, liver HepG2 and lung A549 cell line by 85, 80 and 78 %, respectively [43].

CONCLUSION

This work reports a study of two Schiff base triazole ligands H_2L^1 and H_2L^2 and their metal complexes with Co(II), Ni(II), Cu(II), Zn(II), Fe(III) and Ag(I). They were synthesized and characterized by IR, ^1H and ^{13}C NMR, UV–Vis, mass spectra, and magnetic measurements. The IR spectra show that these ligands are coordinated to the metal ions in a tridentate manner. From the magnetic measurements and electronic spectra, it is found that the geometrical structure of these complexes are octahedral except the silver complexes have tetrahedral structure. The cytotoxicity and the percent of Urokinase plasmingen activator (uPA) inhibition of ligands H_2L^1 and H_2L^2 and their metal complexes against three different human cancer cell lines including breast MCF-7, liver HepG2, and lung A549 that may act through uPA inhibition were evaluated. The activity order follows the order: complex 12 > complex 6 > complex 4 > complex 13 > complex 10 > complex 2 > H_2L^2 > H_2L^1 > complex 9 > complex 5.

REFERENCES

[1] Ozben, T., Mechanisms and strategies to overcome multiple drug resistance in cancer. *FEBS Lett.* 2006, *580*, 2903-2909.

[2] Kamal, A.; Prabhakar, S.; Janaki Ramaiah, M.; Venkat Reddy, P.; Ratna Reddy, C.; Mallareddy, A.; Shankaraiah, N.; Lakshmi Narayan Reddy, T.; Pushpavalli, S. N. C. V.

L.; Pal-Bhadra, M., Synthesis and anticancer activity of chalcone-pyrrolobenzodiazepine conjugates linked via 1,2,3-triazole ring side-armed with alkane spacers. *European Journal of Medicinal Chemistry* 2011, *46* (9), 3820-3831.

[3] Duan, Y.-C.; Zheng, Y.-C.; Li, X.-C.; Wang, M.-M.; Ye, X.-W.; Guan, Y.-Y.; Liu, G.-Z.; Zheng, J.-X.; Liu, H.-M., Design, synthesis and antiproliferative activity studies of novel 1,2,3-triazole–dithiocarbamate–urea hybrids. *European Journal of Medicinal Chemistry* 2013, *64* (0), 99-110.

[4] Mahmoud, A. E.; Ali, M. M. Fermented pomegranate (Punica granatum) peel extract as a novel anticancer agent targeting angiogenesis and metastasis. *International Journal of Toxicological & Pharmacological Research* 2014, 6(4), 60-66.

[5] Omar M. A.; Shaker, Y. M.; Galal, S. A.; Ali, M. M.; Kerwin, S. M.; Li, J.; Tokuda, H.; Ramadan, R. A.; El Diwani, H. I. Synthesis and docking studies of novel antitumor benzimidazoles. *Bioorganic & Medicinal Chemistry* 2012, 20(24), 6989-7001.

[6] Agalave, S. G.; Maujan, S. R.; Pore, V. S., Click Chemistry: 1,2,3-Triazoles as Pharmacophores. *Chemistry – An Asian Journal* 2011, *6* (10), 2696-2718.

[7] Aher, N. G.; Pore, V. S.; Mishra, N. N.; Kumar, A.; Shukla, P. K.; Sharma, A.; Bhat, M. K., Synthesis and antifungal activity of 1,2,3-triazole containing fluconazole analogues. *Bioorganic & Medicinal Chemistry Letters* 2009, *19* (3), 759-763.

[8] Demaray, J. A.; Thuener, J. E.; Dawson, M. N.; Sucheck, S. J., Synthesis of triazole-oxazolidinones via a one-pot reaction and evaluation of their antimicrobial activity. *Bioorganic & Medicinal Chemistry Letters* 2008, *18* (17), 4868-4871.

[9] Buckle, D. R.; Outred, D. J.; Rockell, C. J. M.; Smith, H.; Spicer, B. A., Studies on v-triazoles. 7. Antiallergic 9-oxo-1H,9H-benzopyrano[2,3-d]-v-triazoles. *Journal of Medicinal Chemistry* 1983, *26* (2), 251-254.

[10] Giffin, M. J.; Heaslet, H.; Brik, A.; Lin, Y.-C.; Cauvi, G.; Wong, C.-H.; McRee, D. E.; Elder, J. H.; Stout, C. D.; Torbett, B. E., A Copper(I)-Catalyzed 1,2,3-Triazole Azide−Alkyne Click Compound Is a Potent Inhibitor of a Multidrug-Resistant HIV-1 Protease Variant. *Journal of Medicinal Chemistry* 2008, *51* (20), 6263-6270.

[11] Patpi, S. R.; Pulipati, L.; Yogeeswari, P.; Sriram, D.; Jain, N.; Sridhar, B.; Murthy, R.; T, A. D.; Kalivendi, S. V.; Kantevari, S., Design, Synthesis, and Structure–Activity Correlations of Novel Dibenzo[b,d]furan, Dibenzo[b,d]thiophene, and N-Methylcarbazole Clubbed 1,2,3-Triazoles as Potent Inhibitors of Mycobacterium tuberculosis. *Journal of Medicinal Chemistry* 2012, *55* (8), 3911-3922.

[12] De Simone, R.; Chini, M. G.; Bruno, I.; Riccio, R.; Mueller, D.; Werz, O.; Bifulco, G., Structure-Based Discovery of Inhibitors of Microsomal Prostaglandin E2 Synthase−1, 5-Lipoxygenase and 5-Lipoxygenase-Activating Protein: Promising Hits for the Development of New Anti-inflammatory Agents. *Journal of Medicinal Chemistry* 2011, *54* (6), 1565-1575.

[13] Pagliai, F.; Pirali, T.; Del Grosso, E.; Di Brisco, R.; Tron, G. C.; Sorba, G.; Genazzani, A. A., Rapid Synthesis of Triazole-Modified Resveratrol Analogues via Click Chemistry. *Journal of Medicinal Chemistry* 2005, *49* (2), 467-470.

[14] Ferreira, J. P. A.; Silva, V. L. M.; Elguero, J.; Silva, A. M. S., Synthesis of new pyrazole-1,2,3-triazole dyads. *Tetrahedron Letters* 2013, *54* (39), 5391-5394.

[15] Aufort, M.; Herscovici, J.; Bouhours, P.; Moreau, N.; Girard, C., Synthesis and antibiotic activity of a small molecules library of 1,2,3-triazole derivatives. *Bioorganic & Medicinal Chemistry Letters* 2008, *18* (3), 1195-1198.

[16] Buechel, K. H.; Gold, H.; Frohberger, P. E.; Kaspers, H. 1975.
[17] Boddy, I. K.; Briggs, G. G.; Harrison, R. P.; Jones, T. H.; O'Mahony, M. J.; Marlow, I. D.; Roberts, B. G.; Willis, R. J.; Bardsley, R.; Reid, J., *Pestic. Sci.* 1996, *48*, 189-196.
[18] Krueger, H. R.; Schroeer, U.; Baumert, D.; Joppien, H. 96. 1981.
[19] Fan, W.-Q.; Katritzky, A. R., 4.01 - 1,2,3-Triazoles. In *Comprehensive Heterocyclic Chemistry II*, Katritzky, A. R.; Rees, C. W.; Scriven, E. F. V., Eds. Pergamon: Oxford, 1996; pp 1-126.
[20] Kamal, A.; Shankaraiah, N.; Devaiah, V.; Laxma Reddy, K.; Juvekar, A.; Sen, S.; Kurian, N.; Zingde, S., Synthesis of 1,2,3-triazole-linked pyrrolobenzodiazepine conjugates employing 'click' chemistry: DNA-binding affinity and anticancer activity. *Bioorganic & Medicinal Chemistry Letters* 2008, *18* (4), 1468-1473.
[21] Iqbal, A.; Siddiqui, H. L.; Ashraf, C. M.; Ahmad, M.; Weaver, G. W., *Molecules* 2007, *12*, 245-254.
[22] Vashi, K.; Naik, H. B., *Eur. J. Chem.* 2004, *1*, 272-276.
[23] Hossain, M. E.; Alam, M. N.; Begum, J.; Akbar Ali, M.; Nazimuddin, M.; Smith, F. E.; Hynes, R. C., The preparation, characterization, crystal structure and biological activities of some copper(II) complexes of the 2-benzoylpyridine Schiff bases of S-methyl- and S-benzyldithiocarbazate. *Inorganica Chimica Acta* 1996, *249* (2), 207-213.
[24] Shukla, S.; Srivastava, R. S.; Shrivastava, S. K.; Sodhi, A.; Kumar, P., Synthesis, characterization, in vitro anticancer activity, and docking of Schiff bases of 4-amino-1,2-naphthoquinone. *Medicinal Chemistry ResearchMed. Chem. Res.* 2013, *22* (4), 1604 - 1617.
[25] Sadana, A. K.; Mirza, Y.; Aneja, K. R.; Prakash, O., Hypervalent iodine mediated synthesis of 1-aryl/hetryl-1,2,4-triazolo[4,3-a] pyridines and 1-aryl/hetryl 5-methyl-1,2,4-triazolo[4,3-a]quinolines as antibacterial agents. *European Journal of Medicinal Chemistry* 2003, *38* (5), 533-536.
[26] Rezaei, Z.; Khabnadideh, S.; Pakshir, K.; Hossaini, Z.; Amiri, F.; Assadpour, E., Design, synthesis, and antifungal activity of triazole and benzotriazole derivatives. *European Journal of Medicinal Chemistry* 2009, *44* (7), 3064-3067.
[27] Guo-Qiang, H.; Li-Li, H.; Song-Qiang, X.; Wen-Long, H., *Chin. J. Chem.* 2008, *26*, 1145-1149.
[28] Jin, J.; Zhang, L.; Zhang, A.; Lei, X. X.; Zhu, J. H., *Molecules* 2007, *12*, 1596-1605.
[29] Bagihalli, G. B.; Avaji, P. G.; Patil, S. A.; Badami, P. S., Synthesis, spectral characterization, in vitro antibacterial, antifungal and cytotoxic activities of Co(II), Ni(II) and Cu(II) complexes with 1,2,4-triazole Schiff bases. *European Journal of Medicinal Chemistry* 2008, *43* (12), 2639-2649.
[30] Chohan, Z. H.; Hanif, M., Synthesis and characterization of biologically active new Schiff bases containing 3-functionalized 1,2,4-triazoles and their zinc(II) complexes: crystal structure of 4-bromo-2-[(E)-(1H-1,2,4-triazol-3-ylimino)- methyl]phenol. *Applied Organometallic Chemistry* 2011, *25* (10), 753-760; (b) Hanif, M.; Chohan, Z. H., Design, spectral characterization and biological studies of transition metal(II) complexes with triazole Schiff bases. *Spectrochimica Acta Part A: Molecular and Biomolecular Spectroscopy* 2013, *104* (0), 468-476.
[31] Vogel, A. I., A Text Book of Quantitative Inorganic Analysis, 4th edn. Longmans: London, 1978; (b) Holzbecher, Z.; Divis, L.; Kral, M.; Sucha, L.; Vracil, F., Handbook of Organic Reagents in Inorganic Analysis. Wiley: Chichester, 1976.

[32] Salama, T. M.; Ahmed, A. H.; El-Bahy, Z. M., Y-type zeolite-encapsulated copper(II) salicylidene-p-aminobenzoic Schiff base complex: Synthesis, characterization and carbon monoxide adsorption. *Microporous and Mesoporous Materials* 2006, *89* (1-3), 251-259.

[33] Skehan, P.; Storeng, R.; Scudiero, D.; Monks, A.; Mahon, J.; Vistica, D.; Warren, J. T.; Bokesch, H.; Kenney, S.; Boyd, M. R., New Colorimetric Cytotoxicity Assay for Anticancer-Drug Screening. *J. Natil Cancer Inst.* 1990, *82* (13), 1107-1112.

[34] Li, L.; Qu, R.; de Kochko, A.; Fauquet, C.; Beachy, R. N., An improved rice transformation method using the biolistic method. *Plant Cell Rep.* 1993, *12*, 250-255.

[35] Geary, W. J., The use of conductivity measurements in organic solvents for the characterisation of coordination compounds. *Coordination Chemistry Reviews* 1971, *7* (1), 81-122.

[36] Ilhan, S.; Temel, H.; Yilmaz, I.; Şekerci, M., Synthesis and characterization of new macrocyclic Schiff base derived from 2,6-diaminopyridine and 1,7-bis(2-formylphenyl)-1,4,7-trioxaheptane and its Cu(II), Ni(II), Pb(II), Co(III) and La(III) complexes. *Polyhedron* 2007, *26* (12), 2795-2802.

[37] Faheim, A. A.; Abdou, S. N.; Abd El-Wahab, Z. H., Synthesis and characterization of binary and ternary complexes of Co(II), Ni(II), Cu(II) and Zn(II) ions based on 4-aminotoluene-3-sulfonic acid. *Spectrochimica Acta Part A: Molecular and Biomolecular Spectroscopy* 2013, *105* (0), 109-124.

[38] Jayabalakrishnan, C.; Natarajan, K., Synthesis, characterization, and biological activities ofruthenium (II) carbonyl complexes containing bifunctional tridentate Schiff bases. *Synthesis and Reactivity in Inorganic and Metal-Organic Chemistry* 2001, *31* (6), 983-995.

[39] Majumder, A.; Rosair, G. M.; Mallick, A.; Chattopadhyay, N.; Mitra, S., Synthesis, structures and fluorescence of nickel, zinc and cadmium complexes with the N,N,O-tridentate Schiff base N-2-pyridylmethylidene-2-hydroxy-phenylamine. *Polyhedron* 2006, *25* (8), 1753-1762.

[40] Kumar, R.; Chandra, S., Spectroscopic techniques and cyclic voltammetry with synthesis: Manganese(II) coordination stability and its ligand field parameters effect on macrocyclic ligands. *Spectrochimica Acta Part A: Molecular and Biomolecular Spectroscopy* 2007, *67* (1), 188-195.

[41] Singh, A. K.; Pandey, O. P.; Sengupta, S. K., Synthesis, spectral characterization and biological activity of zinc(II) complexes with 3-substituted phenyl-4-amino-5-hydrazino-1, 2, 4-triazole Schiff bases. *Spectrochimica Acta Part A: Molecular and Biomolecular Spectroscopy* 2012, *85* (1), 1-6.

[42] Singh, M.; Aggarwal, V.; Singh, U. P.; Singh, N. K., Synthesis, characterization and spectroscopic studies of a new ligand [N-(2-methoxybenzoyl)hydrazinecarbodithioate] ethyl ester and its Mn(II) and Cd(II) complexes: X-ray structural study of Mn(II) complex. *Polyhedron* 2009, *28*, 107-112.

[43] Kovala-Demertzi, D.; Alexandratos, A.; Papageorgiou, A.; Yadav, P. N.; Dalezis, P.; Demertzis, M. A., Synthesis, characterization, crystal structures, in vitro and in vivo antitumor activity of palladium(II) and zinc(II) complexes with 2-formyl and 2-acetyl pyridine N(4)-1-(2-pyridyl)-piperazinyl thiosemicarbazone. *Polyhedron* 2008, *27* (13), 2731-2738.

[44] Mohamed, G. G.; Omar, M. M.; Hindy, A. M. M., Synthesis, characterization and biological activity of some transition metals with Schiff base derived from 2-thiophene carboxaldehyde and aminobenzoic acid. *Spectrochimica Acta Part A: Molecular and Biomolecular Spectroscopy* 2005, *62* (4–5), 1140-1150.

[45] El-Wahab, Z. H. A.; Mashaly, M. M.; Salman, A. A.; El-Shetary, B. A.; Faheim, A. A., Co(II), Ce(III) and UO2(VI) bis-salicylatothiosemicarbazide complexes: Binary and ternary complexes, thermal studies and antimicrobial activity. *Spectrochimica Acta Part A: Molecular and Biomolecular Spectroscopy* 2004, *60* (12), 2861-2873.

[46] Youssef, N. S.; El-Zahany, E.; El-Seidy, A. M. A.; Caselli, A.; Cenini, S., Synthesis and characterization of some transition metal complexes with a novel Schiff base ligand and their use as catalysts for olefin cyclopropanation. *Journal of Molecular Catalysis A: Chemical* 2009, *308* (1–2), 159-168.

[47] Abu-Melha, K. S.; El-Metwally, N. M., Spectral and thermal studies for some transition metal complexes of bis(benzylthiocarbohydrazone) focusing on EPR study for Cu(II) and VO2+. *Spectrochimica Acta Part A: Molecular and Biomolecular Spectroscopy* 2008, *70* (2), 277-283.

[48] Youssef, N. S.; El-Zahany, E.; El-Seidy, A. M. A.; Caselli, A.; Fantauzzi, S.; Cenini, S., Synthesis and characterisation of new Schiff base metal complexes and their use as catalysts for olefin cyclopropanation. *Inorganica Chimica Acta* 2009, *362* (6), 2006-2014.

[49] Klayman, D. L.; Bartosevich, J. F.; Griffin, T. S.; Mason, C. J.; Scovill, J. P., 2-Acetylpyridine thiosemicarbazones. 1. A new class of potential antimalarial agents. *Journal of Medicinal Chemistry* 1979, *22* (7), 855-862.

[50] Tümer, M.; Ekinci, D.; Tumer, F.; Bulut, A., Synthesis, characterization and properties of some divalent metal(II) complexes: Their electrochemical, catalytic, thermal and antimicrobial activity studies. *Spectrochim. Acta Part A: Mol. Biomol. Spectrosc.* 2007, *67*, 916-929.

[51] Moreau, E.; Fortin, S.; Lacroix, J.; Patenaude, A.; Rousseau, J. L. C.; Gaudreault, R. C., N-Phenyl-N′-(2-chloroethyl)ureas (CEUs) as potential antineoplastic agents. Part 3: Role of carbonyl groups in the covalent binding to the colchicine-binding site. *Bioorganic & Medicinal Chemistry* 2008, *16* (3), 1206-1217.

Smart Nanocomposites
Volume 5, Number 2
ISSN: 1949-4823

APPLICATION OF IMPEDANCE SPECTROSCOPY TO THE ANALYSIS OF THE MECHANISM OF ELECTRON TRANSPORT IN DISORDERED MATERIALS

I. P. Zvyagin and M. A. Ormont*
Faculty of Physics, Moscow State University
Moscow, Russia

ABSTRACT

It is argued that experimentally observed sharp crossover from linear to quadratic frequency dependence of low temperature conductivity $\mathrm{Re}\,\sigma(\omega)$ can be related to the suppression of hybridization at high frequencies and the transition from variable-range to fixed-range hopping regime. Large observed values of the ratio $|\mathrm{Im}\,\sigma(\omega)|/\mathrm{Re}\,\sigma(\omega)$ at frequencies below the crossover frequency can be due to the fact that the conductivity is determined by two contributions - resonance (phononless) and relaxation; indeed, in the frequency region under study the imaginary part of the conductivity is determined by large phononless contribution, whereas the real part is determined by the relaxation contribution.

Keywords: disordered semiconductors, AC conductivity, dielectric loss, resonance hopping conductivity, Coulomb gap

INTRODUCTION

For disordered systems (e.g., doped and amorphous semiconductors, granular metals, conductive polymers), the theory of hopping conductivity predicts a frequency dependence of the real part of the hopping conductivity that can be described by the universal power law $\mathrm{Re}\,\sigma(\omega) = A\omega^s$, where A and s are constants; the value of the exponent s usually lies in the interval $0 < s \le 1$ [1-4]. The frequency dependence with $s \approx 1$ is generally associated with phonon-assisted hopping [1]. A similar slightly sublinear frequency dependence ($s < 1$) can be obtained for phononless (resonance) hopping conductivity at low temperatures if one

* E-mail: ormont@phys.msu.ru

takes into account Coulomb correlations for localized electrons [3]. At high frequencies, the theory of phononless conductivity predicts a crossover from a slightly sublinear frequency dependence in the presence of Coulomb interaction [3] to a quadratic frequency dependence ($s = 2$) in the higher-frequency region, where Coulomb interaction effects can be disregarded [2]. In this case the quantum energy $\hbar\omega$ is greater than the energy of Coulomb interaction between the electrons of "active" pairs $U(r_\omega) = e^2/\kappa r_\omega$ (here r_ω is the characteristic frequency-dependent hopping distance and κ is the permittivity). The crossover frequency ω_{cr} is determined by the condition $U(r_{\omega_{cr}}) = \hbar\omega_{cr}$. At low temperatures and not too high frequencies, the real part of the conductivity $\mathrm{Re}\,\sigma(\omega)$ is determined by the phonon mechanism, and the zero-phonon conductivity begins to dominate over relaxation with increasing frequency. Resonance transitions give the main contribution to $\mathrm{Re}\,\sigma(\omega)$ at low temperatures and high frequencies. The crossover from linear to quadratic frequency dependence was actually observed near $1\ THz$ in doped semiconductors (Si:P, Si:B) near the metal–insulator transition [5 – 7] and in metallic nanocomposites [8].

In the pair approximation [2, 3], the minimum distance r_ω between the centers of the pairs giving the main contribution to the conductivity is determined from the condition $\hbar\omega = 2I(r)$, where $I(r) = I_0 \exp(-r/a)$ is the resonance integral, $I_0 \sim e^2/\kappa a$ is the preexponential factor, and a is the localization length. We have $r_\omega = a\ln(\omega_c/\omega)$, where $\omega_c = 2I_0/\hbar$. Provided that the intercenter distance in a pair is $r_{if} < r_\omega$, level repulsion due to hybridization makes resonance transitions impossible. Therefore, the main contribution to the conductivity comes from the pairs with intercenter distances r_{if} such that $r_\omega < r_{if} < r_\omega + a$.

There are, however, some features that disagree with the conventional theory of phononless conductivity. At high frequencies the approach based on the pair approximation predicts a nonmonotonic frequency dependence of $\mathrm{Re}\,\sigma(\omega)$ with a smooth maximum at the frequency $\omega_m \sim 0.05\omega_c$ [9]. Such behavior is due to a decrease in the number of final sites taking part in the conductivity and to a decrease in the dipole moment $e\,r_\omega$ with increasing frequency. The transition to the falling portion of the curve $\mathrm{Re}\,\sigma(\omega)$ preceding the saturation occurs before the region of quadratic dependence ($s \sim 2$) is achieved and the crossover from linear to quadratic frequency dependence with increasing frequency is not expected. Accordingly, up to the frequency ω_m, corresponding to the maximum of $\mathrm{Re}\,\sigma(\omega)$, the Coulomb interaction between the electrons of "active" pairs plays an important role and generally cannot be disregarded; therefore, the frequency dependence of $\mathrm{Re}\,\sigma(\omega)$ should be close to linear ($s \approx 1$) [9]. This disagrees with the experimentally observed sharp crossover of the real part of conductivity from linear to quadratic frequency dependence (kink on the curves of $\ln(\mathrm{Re}\,\sigma(\omega))$ vs $\ln\omega$ [5 – 7]). Moreover, non-monotonic frequency dependence of the conductivity $\mathrm{Re}\,\sigma(\omega)$ predicted by the theory is not observed (see the data for doped silicon Si:B [5], Si:P [6, 7]).

At frequencies below the crossover frequency, $\omega < \omega_{cr}$, measured frequency dependences of the real and imaginary parts of the complex conductivity are similar [6] $\left|\mathrm{Im}\,\sigma(\omega)\right| \sim \mathrm{Re}\,\sigma(\omega) \sim \omega^{s}$ ($s \sim 1$).

In this case, the frequency dependence of the imaginary part of conductivity has no singularities in the vicinity of ω_{cr}, remaining almost linear. For $\omega < \omega_{cr}$, the measured ratio $\left|\mathrm{Im}\,\sigma(\omega)\right| / \mathrm{Re}\,\sigma(\omega) \sim 10^{2}$ exceeds the value given by the theory of relaxation conductivity by a factor of about 30 [10].

Thus, the standard theory of resonance conductivity using the concept of frequency-dependent hopping distance r_{ω} does not describe the behavior of the conductivity $\mathrm{Re}\,\sigma(\omega)$ in the crossover region [9].

FREQUENCY DEPENDENCE OF THE CONDUCTIVITY IN THE CROSSOVER REGION

The kink on the curves $\ln\left(\mathrm{Re}\,\sigma(\omega)\right)$ vs $\ln(\omega)$ may be related to the transition to the regime of fixed-range hopping when the optimum hopping distance r_{opt} becomes frequency-independent due to the suppression of the hybridization of electronic states as hybridization times become long compared to the period of the AC field, i.e., for $\omega > \omega_{R}$, where $\omega_{R} = 2I(r_{if})/\hbar$ is the Rabi frequency characterizing the hybridization.

At high frequencies in the fixed-range hopping regime, when hybridization effects are unimportant and optimal hopping distance r_{opt} is frequency independent, the frequency dependence of the phononless conductivity has the form [11]

$$\mathrm{Re}\,\sigma(\omega) = \frac{\pi^{2}}{3} C e^{2} \rho_{0}^{2} a^{5} \omega \left(\hbar\omega + \frac{e^{2}}{\kappa r_{opt}} \right), \tag{1}$$

where $r_{opt} \approx 3a$, ρ_{0} is the density of states, and $C \approx 10$ is the numerical coefficient.

The frequency-independent optimal hopping distance r_{opt} determines a monotonic frequency dependence of conductivity over a wide frequency range. The optimal hopping distance r_{opt} is determined by the trade-off between the increase in the dipole moment at one-electron transition and the exponential decrease in the overlap of the wave functions as the distance between the centers increases. Thus, the main contribution to the conductivity comes from electron transitions in pairs with optimal distances between centers. In this case, the number of final sites for these transitions and the variations in the dipole moment are frequency-independent.

According to (1), the crossover frequency for the transition from a linear to quadratic frequency dependence of the phononless conductivity $\mathrm{Re}\,\sigma(\omega)$ is determined by [11]

$$\hbar\omega_{cr} = e^2 / \kappa r_{opt} . \qquad (2)$$

It follows that $\omega_{cr} \sim 0.1\omega_c$; for the characteristic value of localization radius $a \sim 30$ Å, we obtain that the crossover frequency $\nu_{cr} = \omega_{cr} / 2\pi$ is about 1 THz.

The transition to the fixed-range hopping regime with frequency independent optimal hopping distance r_{opt} takes place at $r_\omega \approx r_{opt} \approx 3a$, i.e., at the frequency $\omega_{opt} = \exp(-3)\,\omega_c \approx 0.05\omega_c$, that corresponds to the vicinity of the crossover frequency $\omega_{cr} \sim 0.1\omega_c$.

The frequency ω_{opt} of the transition from variable-range hopping to fixed-range hopping regime lies near the frequency of the maximum $\omega_m \sim \omega_{opt}$ of $\mathrm{Re}\,\sigma(\omega)$ in the standard theory of phononless conductivity (Figure 1).

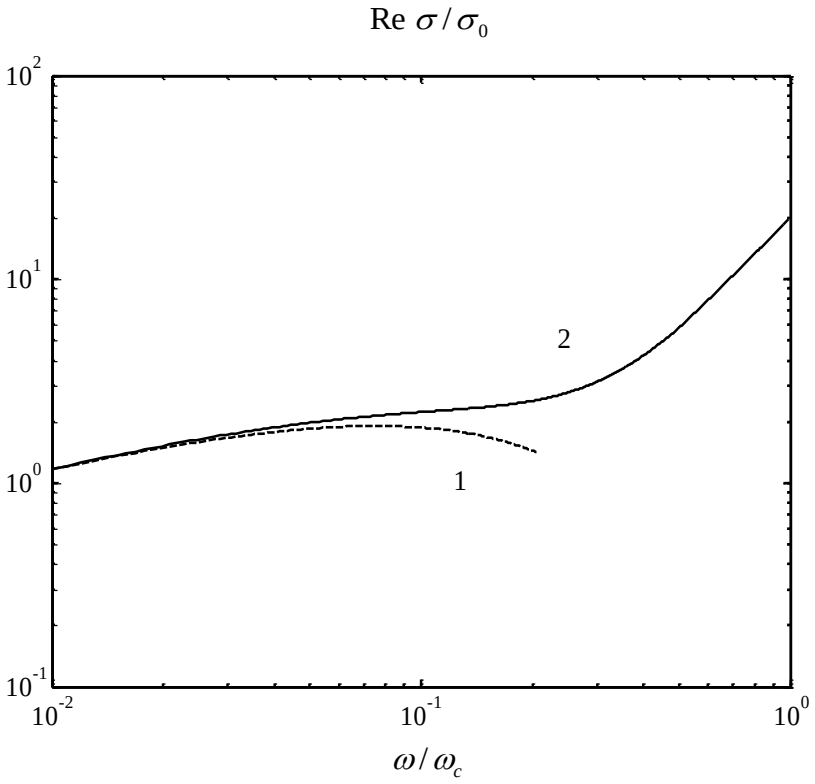

Figure 1. Frequency dependence of the real part of the conductivity, taking into account both resonance and relaxation contributions: (curve 1) conventional theory; (curve 2) model that takes into account transition from variable-range hopping to fixed-range hopping regime.

FREQUENCY DEPENDENCE OF THE LOSS ANGLE

A possible reason for a large value of the ratio $|\mathrm{Im}\,\sigma(\omega)|/\mathrm{Re}\,\sigma(\omega) \sim 10^2$, compared with the value given by the theory of relaxation conductivity, can be related to the fact that the conductivity is determined by two contributions - resonance (phononless) and relaxation. Accordingly,

$$\mathrm{ctg}\,\gamma(\omega) = \mathrm{Im}(\sigma^{res}(\omega) + \sigma^{rel}(\omega))/\mathrm{Re}(\sigma^{res}(\omega) + \sigma^{rel}(\omega)), \quad (3)$$

where γ is the dielectric loss angle, which complements the phase-shift angle between the current and voltage to $\pi/2$.

Large value of ratio $|\mathrm{Im}\,\sigma(\omega)|/\mathrm{Re}\,\sigma(\omega)$ indicates that at frequencies below the crossover frequency $\omega < \omega_{cr}$, where frequency dependence of loss angle $\gamma(\omega)$ is weak, imaginary part of the conductivity is determined by large phononless contribution $\mathrm{Im}\,\sigma^{res}(\omega)$ that substantially exceeds $\mathrm{Im}\,\sigma^{rel}(\omega)$, whereas the real part is determined by the relaxation contribution $\mathrm{Re}\,\sigma^{rel}(\omega)$. At frequencies above the crossover frequency ω_{cr}, both real and imaginary parts of the complex conductivity are determined by the phononless contribution.

CONCLUSION

Thus, a sharp crossover from linear to quadratic frequency dependence of phononless conductivity in the vicinity of ω_{cr} can be explained by the suppression of hybridization at high frequencies and transition from variable-range hopping to fixed-range hopping regimes.

The analysis of the magnitude and frequency dependence of the loss angle γ, in general, requires the simultaneous consideration of both resonance and relaxation contributions to the conductivity. At the same time in different frequency regions the ratio of the resonance to relaxation contributions may be different for the real and imaginary parts of the conductivity, which leads to the observed large values of $|\mathrm{ctg}\,\gamma|$.

REFERENCES

[1] Pollak, M.; Geballe, T.H. *Phys. Rev.* 1961, vol 122, 1742-1753.
[2] Mott, N. F. *Phil. Mag.* 1970, vol 22, 7-29 .
[3] Shklovskii, B. I.; Efros, A. L. *JETP* 1981, vol 81, 406-415.
[4] Zvyagin, I. P. In Charge Transport in Disordered Solids with Applications in Electronics, Ed. S. Baranovski; John Wiley & Sons: Chichester, 2006; pp 339-378.
[5] Lee, M.; Stutzmann, M.L. *Phys. Rev. Lett.* 2001, vol 87, 056402-1-056402-4.
[6] Helgren, E.; Armitage, N.P.; Gruner, G. *Phys. Rev.* 2004, vol B69, 014201-1-014201-15.

[7] Hering, M.; Scheffler, M.; et al. *Phys. Rev*. 2007, vol B75, 205203-1-205203-9.
[8] Reedijk, J. A.; Adriaanse, L.J.; et al. *Phys. Rev*. 1998, vol B57, R15116- R15119.
[9] Zvyagin, I. P.; Ormont, M.A. Moscow University Physics Bulletin 2008, vol 63, No. 4, 272-275.
[10] Efros, A. L. *JETP* 1985, vol 62, 1057-1059.
[11] Ormont, M. A. Moscow University Physics Bulletin 2011, vol 66, No. 2, 162-168.

SHORT COMMUNICATIONS

INTRODUCTION

Short communications below represent the selected proceedings of the 8-th International Symposium “Molecular Order and Mobility in Polymer Systems”. The Symposium is one of the most important international polymer meetings in Russia. It continues a series of Symposia organized by the Institute of Macromolecular Compounds of Russian Academy of Sciences and titled alternatively as “Molecular Mobility and Order in Polymer Systems”(I-1994, III-1999, V- 2005, VII - 2011) and “Molecular Order and Mobility in Polymer Systems”.(II- 1996, IV-2002, VI- 2008). Selected short communications were chosen among the best results presented at this international symposium.

Smart Nanocomposites
Volume 5, Number 2
ISSN: 1949-4823

COMPUTER SIMULATION OF DENDRONIZED POLYMERS: EFFECT OF THE GRAFTS BRANCHING ON THE SEGMENT ANISOTROPY OF THE BACKBONE

I. V. Michailov[1] and A. A. Darinskii[1,2]
[1]Institute of Macromolecular Compounds of RAS, St. Petersburg, Russia
[2]ITMO University, St. Petersburg, Russia

ABSTRACT

Langevin dynamics simulations were performed for the bead-spring model of dendronized polymers with the same grafting density and molecular mass of grafts by the variation of the branching degree of grafts. The cases of the good (athermal model) and theta solvents were considered. The effect of the branching on the macromolecular thickness D and the induced persistence length l_p of the backbone was studied and compared with the mean-field theory predictions. D decreases with the branching of grafts in both solvents. l_p doesn't depend on the branching in the good solvent in agreement with the theory predictions. In the theta solvent l_p increases with the branching but this increase is weaker than the theory predicts. Correspondingly the segment anisotropy l_p/D increases by the increase of the grafts branching in both solvents.

INTRODUCTION

Dendronized polymers consist of the linear backbone with repeatedly grafted branched side groups. Due to the repulsion of neighboring grafts the backbone is remarkably stretched as comparing to the free chain.One of the most important problems is the dependence of this induced stiffness on the grafting density and molecular parameters of side chains, such as the molecular mass and the architecture. There are a lot of publications devoted to the theory or computer simulation of comblike polymers with linear side chains (bottle-brushes). However, only few simulations consider macromolecules with branched side chains. Recently the mean-field theory of dendronized polymers was developed [1]. The theory predicts that at good solvent conditions the induced persistence length l_p of the backbone depends on the grafting density and molecular mass N_s of the grafts and doesn't depend on their architecture. It means that l_p should not change by subsitition of linear side chains in the bottle-brush by branched ones with the same molecular mass. Moreover, in the theta solvent l_p even increases with the branching.From another side, the effective thickness D of the macromolecule decreases with the branching. As a result, the anisotropy of the segment measured by the ratio l_p/D should

increase.Therefore, one can tune the segment anisotropy by the variation of the side chain architecture.The theory [1] is based on several important assumptions. In particular, all the calculations were performed for a fully stretched backbone. However in many real polymers the backbone is flexible and the question arises if the theory predictions are applicable to these systems. One of the way of the validation of the theory is a computer simulation. In the present work we perform computer simulation of polymer brushes with the same grafting density and N_s but with different architecture of side chains.The induced persistence length and the thickness will be estimated and compared with the theory predictions.

MODEL AND METHOD

The schematic picture of the simulated polymers is shown in Figure 1. Both for the backbone and side chains we use a coarse-grained bead-spring model.The backbone contains N_b=121 beads. Every second bead is considered as a grafting point to which side chains of the different architecture were grafted. Every side chain consists of N_s =15 beads independently on its architecture. So the overall number N of beads is 1021.As graft models (Figure 2) we consider a linear chain 1 and dendrons 2-4 with different number of branching points.

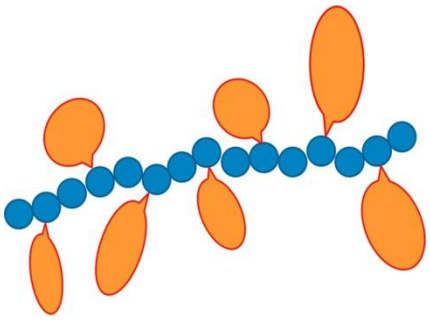

Figure 1. The schematic picture of the polymer segment.

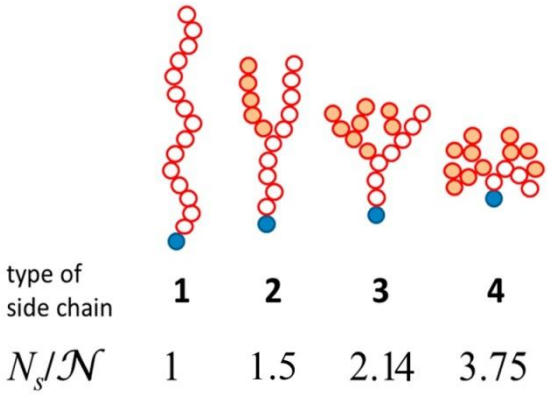

Figure 2. Types of side chains with different degree of branching.

In [1] the ratio $(N_s/\mathcal{N})$ was suggested as a characteristic of the branching degree where $\mathcal{N}$ is the length of the longest path from the grafting point to the terminal bead. This ratio doesn't

depend on the number of monomers N_s in the grafts. The values of $(N_s/\mathcal{N})$ are shown in Figure 2 for every graft architecture.

The bonds between neighboring beads in the backbone and in the grafts are fixed by the potential

$$U_{bond}(r_{ij}) = k(r_{ij} - l_{bond})^2, \quad (1)$$

where r_{ij} is the distance between two bonded beads, k is an elasticity coefficient.

Its value was taken to be equal to 30 k_BT keeping the less than 1% deviation of r_{ij} from the bond lengthl_{bond}. All size characteristics are given below in l_{bond} units. Non-bonded interactions were described by two types of the potentials depending on the solvent quality. For the good solvent conditions we use a truncated and shifted Lennard-Jones (LJ) potential

$$U(r_{ij}) = 4\varepsilon\left[\left(\frac{\sigma}{r_{ij}}\right)^{12} - \left(\frac{\sigma}{r_{ij}}\right)^{6}\right] + \varepsilon: r_{ij} < 2^{\frac{1}{6}}\sigma;\ U(r_{ij}) = 0: r_{ij} \geq 2^{\frac{1}{6}}\sigma, \quad (2)$$

where $\sigma = 0.8$ and $\varepsilon = k_BT$.

This potential corresponds to the athermal model representing very good solvent conditions. For the simulation of theta conditions the Lennard-Jones potential

$$U(r_{ij}) = 4\varepsilon\left[\left(\frac{\sigma}{r_{ij}}\right)^{12} - \left(\frac{\sigma}{r_{ij}}\right)^{6}\right] \quad (3)$$

with ε/k_BT =0.3 was used.

As the simulation method we use the Langevin dynamics where the solvent is considered implicitly as a viscous medium and a source of random forces. The velocity $v_i(t)$ of the i-th bead evolves in time t according to the equation of motion:

$$\frac{d\boldsymbol{v}_i(t)}{dt} = \frac{f_i(t)+R_i(t)}{m_i} - \chi v_i(t), \quad (4)$$

where m_i is the mass of the bead, $f_i(t)$ is the total potential force acting on the i-th bead due to its interactions with other beads, χ is the friction coefficient, and $R_i(t)$ is the associated random force.

RESULTS AND CONCLUSION

Thickness of the Brush

In [1] the cross-sectional thickness of the brush D was estimated as a diameter of the cylinder shell containing N_s monomers with the thickness h equal to the distance between grafting points along the backbone. In our case h=2

$$D = \sqrt{\frac{4N_s}{\pi h <c>}} \quad (5)$$

<c > is the average concentration of side chain monomers in the shell.

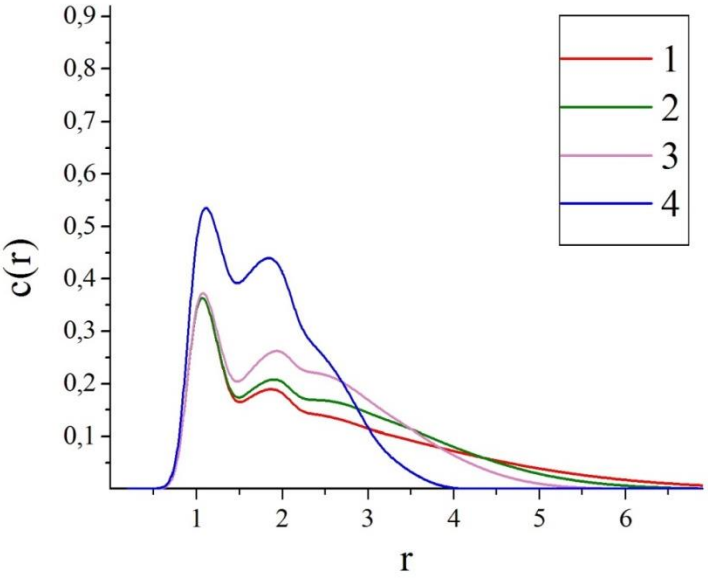

A

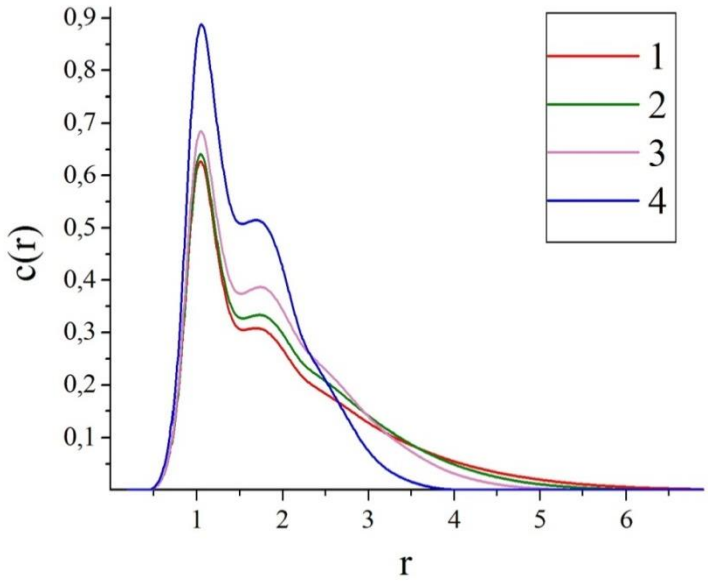

B

Figure 3. The density profiles of side chain monomers for brushes under good (a) and theta (b) solvent conditions.

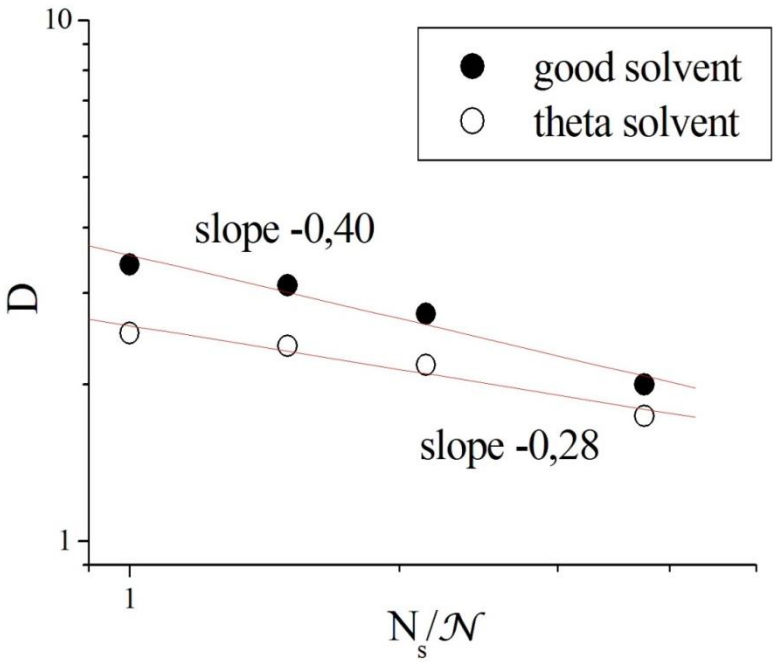

Figure 4. Thickness *D* of brushes as a function of the branching degree of the grafted side chains.

The theory predicts $D\sim(N_s/\mathcal{N})^{-ß/4}$ for good solvent and $D\sim(N_s/\mathcal{N})^{-ß/6}$ for theta solvent with1<ß<2. Fig 3 shows the density profiles of side chain monomers for simulated brushes. On the base of these profiles the average concentration of side chain monomers was calculated

$$\langle c \rangle = \frac{\int_{r=0}^{r=r_{max}} c^2(r) r dr}{\int_{r=0}^{r=r_{max}} c(r) r dr}, \tag{6}$$

and the thickness *D* was obtained by use of eq. (5) for all types of brushes (Figure 4). It is seen that simulated dependences agree with the theory predictions. In both solvents ß=1.6.

Induced Persistence Length

Authors of [1] have used the wormlike chain model for the estimation of the persistence length l_p of the backbone induced by the repulsion interactions between grafts. The theory predicts an insensitivity of l_p to $N_s/\mathcal{N}$ of in the good solvent. For theta conditions $l_p\sim(N_s/\mathcal{N})^{ß/3}$ was predicted.

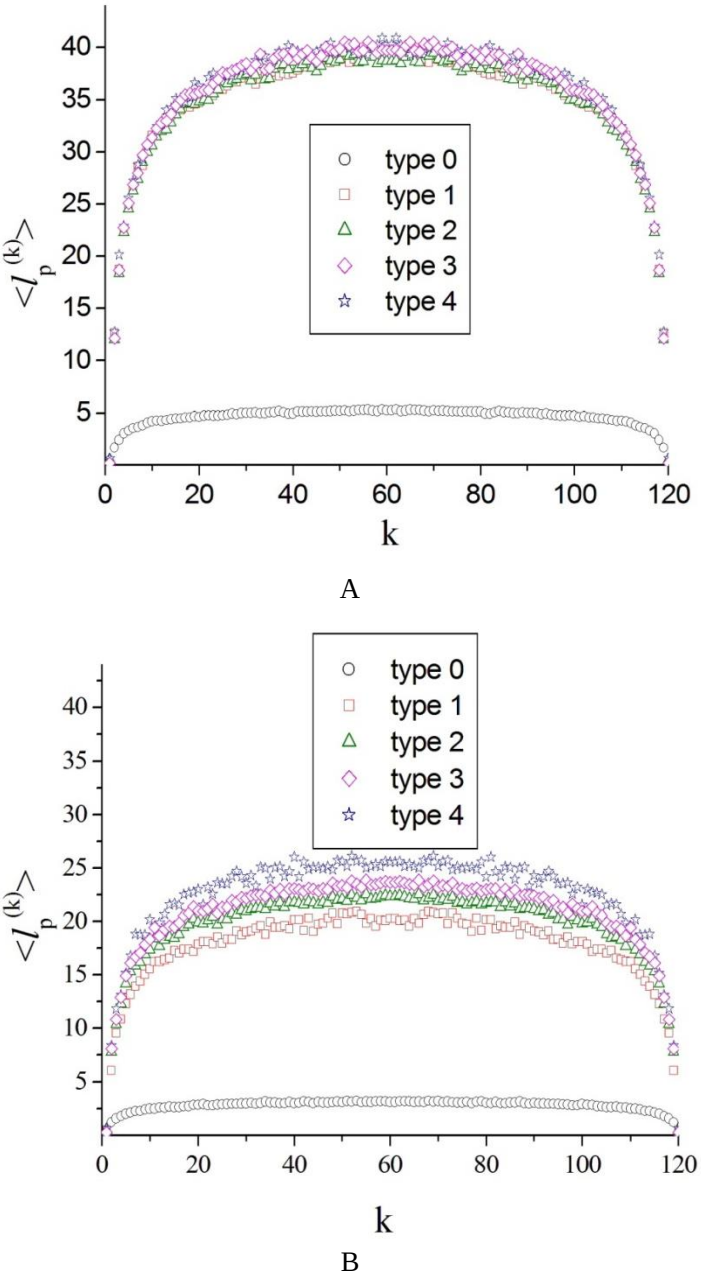

Figure 5. Dependence of the local persistence length$<l_p^{(k)}>$ on the monomer number k along the back bone under good (a) and theta (b) solvent conditions.

The applicability of the persistence length concept to molecular brushes was challenged in [2]. Nevertheless it is used in many experimental and theoretical works devoted to such systems.

In the present work for the estimation of the persistence length we use the Flory definition [3] of the local persistence length as the projection of the monomer vector r_k on the end-to-end vector R_b

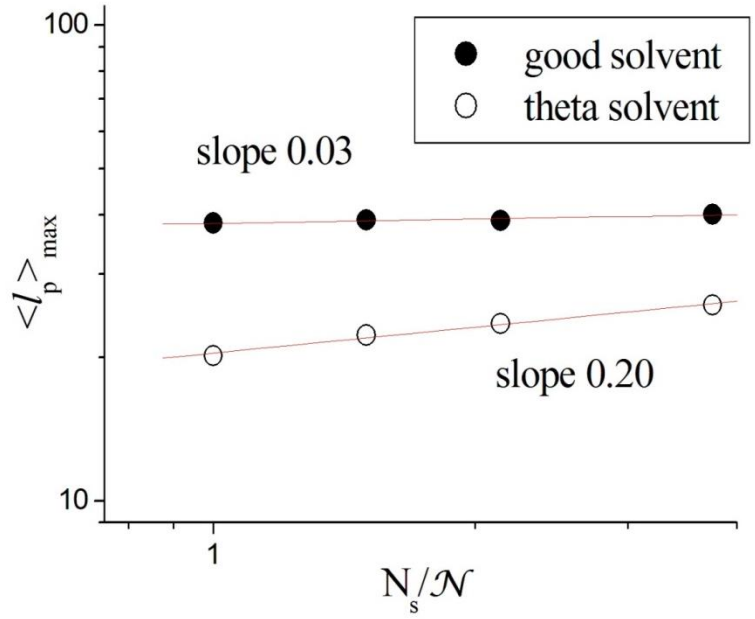

Figure 6. The persistence length$\langle l_p \rangle_{max}$ of brushes as a function of the branching degree$\left(\frac{N_s}{\mathcal{N}}\right)$.

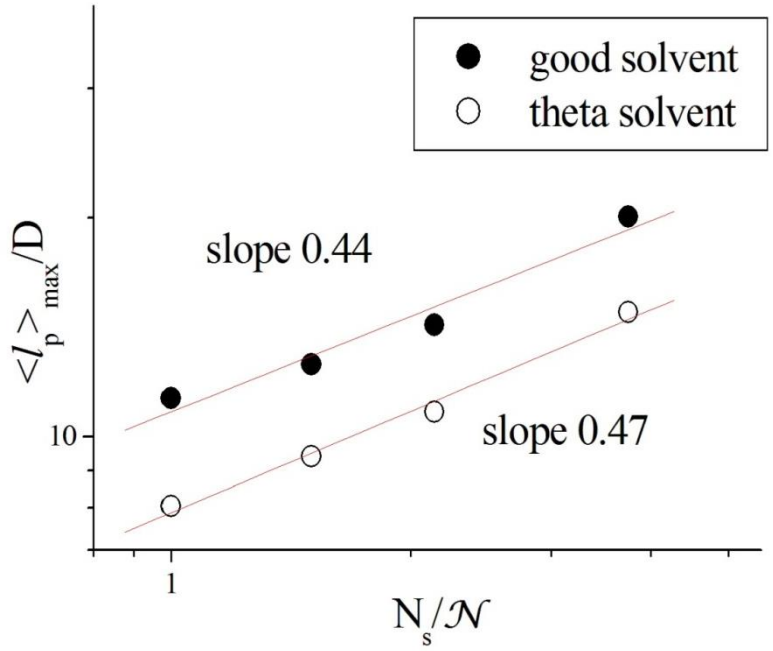

Figure 7. Ratio of persistence length$\langle l_p \rangle_{max}$ over thickness of brushes*D*as a function of the branching degree $\left(\frac{N_s}{\mathcal{N}}\right)$.

$$\langle l_p^{(k)} \rangle \equiv \langle \frac{\vec{r}_k}{|\vec{r}_k|} \cdot \vec{R}_b \rangle \quad (7)$$

Figure 5 shows the dependence of $<l_p^{(k)}>$ on the monomer number k along the backbone.The curves have a "bell"-like shape reflecting the reduced stiffness of the backbone close to its ends.The values of are remarkably larger than those for the main-chain without grafts (type 0), indicating the strong effect of grafts interactions.

For the quantification of our results we use the plateau value $l_p = <l_p>_{max}$ where the end effects disappear. In the good solvent l_p doesn't depend on the branching degree. In the theta solvent l_p increases with the branching. But in this case the simulated dependence $l_p\left(\frac{N_s}{\mathcal{N}}\right)$ is more weak than the theoretical one with of ß=1.6 obtained from the dependence $D\left(\frac{N_S}{\mathcal{N}}\right)$ (Figure 4).

Correspondingly the segment anisotropy l_p/D increases with the branching in both solvents (Figure 7).

ACKNOWLEDGMENTS

This work was partially supported by Government of Russian Federation, grant 074-U01.

Authors are thankful also to the RFBR grant13-03-00524 and to the program 3 of the Department of the Chemistry and Material Science of Russian Academy of Science for the financial support.

REFERENCES

[1] Borisov, O. V.; Zhulina, E. B.; Birshtein, T. M. *ACS Macro Lett*. 2012,1, 1166−1169.

[2] Hsu, H.-P.; Paul, W.; Binder, K. *Macromol.* 2010, 43, 3094.

[3] Connolly, R.; Bellesia, G.; Timoshenko, E. G.; Kuznetsov, Yu A.; Elli, S.; Ganazzoli, *F*. *Macromolec*. 2005, 38, 5288-5299.

Smart Nanocomposites
Volume 5, Number 2
ISSN: 1949-4823

COMPUTER SIMULATION OF LYSINE DENDRIMERS BY MOLECULAR DYNAMICS METHOD

I. Neelov[1,2], M. Ilyash[1,2], S. Falkovich[1] and A. Darinskii[1,2]
[1]Institute of Macromolecular Compounds, Russian Academy of Sciences,
St. Petersburg, Russia
[2]St. Petersburg National Research University of Information Technologies,
Mechanics and Optics (ITMO University), St. Petersburg, Russia

ABSTRACT

Molecular dynamics simulation of polylysine (PL) dendrimers of different generations (G = 1-5) with an asymmetric branching was performed. The size and anisotropy of PL dendrimers as well as their internal structure were determined. It was shown that absolute values and changes of all global characteristics of PL dendrimers with generation number are very close to that of symmetrical dendrimers. Our calculations also show that for asymmetric PL dendrimers the "dense core and a loose shell" model is valid as for dendrimers with symmetrical branching. In general asymmetrically branched PL dendrimers have global structural properties similar to those of dendrimers with symmetrical branching.

1. INTRODUCTION

Dendrimers are highly branched macromolecules having a tree-like structure with branches growing out of the central core. One of the key features of their molecular architecture is the high concentration of end groups available for functionalization. This feature makes dendrimers popular tools for biomedical applications [1-3]. Peptide dendrimers are biocompatible dendrimers consisting of natural amino acid residues. They are used, for example, as a core for a branched multiple antigen peptides (MAPs), as an antibacterial, antiviral and antiamyloid agents as well as for drug and gene delivery, and in many other biomedical applications [4-8].

There are many publications on computer simulation of dendrimers. In most of them the dendrimers with symmetrical branching were studied while for peptide dendrimers there are a few studies [10-13], where mainly small or hybrid dendrimers for specific applications were simulated. The main purpose of this chapter is to determine the spatial structure of real polylysine (PL) dendrimers (with generation number 1 to 5) synthesized in the group of Professor Vlasov [14]. The paper is organized as follows. Description of the molecular model

is given in Part 2. Part 3 presents the results of computer simulation and discussion. Conclusion is given in Part 4.

2. MODEL

It is well known that PL dendrimers have asymmetric branching. It means that spacers originated from each branching point have different length (3 and 7 valence bonds correspondingly).

In present simulation the PL dendrimers of generation G=1-5 with charged NH3 + terminal groups were built by convergent methods: the dendrimer of generation G was constructed by linking the two smaller generation dendrimers.

The force field AMBER-99SB-ildn which describes well the mobility of the atoms in the side groups of the lysine aminoacid residue was used for the most of the calculations. The potential energy of the system in this forcefield is the sum of energies of valence bond stretching, valence and dihedral angles deformations and the energy of the van der Waals and electrostatic interactions.

Preparation of initial conformations in our simulations consists of several stages, including optimization of the structure of a single dendrimer, placing it in the solvent (TIP3P water) with the addition of counter ions (to achieve the electroneutrality of the system), additional optimization and balancing of the whole system. Molecular modeling package Gromacs - 4.5.5 was used for most of these calculations.

Details of PL dendrimers (from first to fifth generations) are listed in Table I, where G is the generation number of dendrimer, M is its molecular weight in g/mol, N_b - number of branching points, N_t-number of terminal groups, and A - the average size of the periodic cell used in the simulation.

The simulation was performed using molecular dynamics simulations with the integration step of 2 fs. Bond lengths were fixed, the van der Waals interactions have been "cut" at a distance of 0.9 nm, the electrostatic interactions were accounted for using the PME (Particle Mesh Ewald) fourth-order method.

Cutoff radius of electrostatic interactions in real space was chosen to be 0.9 nm, lattice in Fourier space - 0.12 nm and accuracy for Ewald sums - 1e-5. The simulation was performed in NPT ensemble at T = 300K during 200ns.

Table I. Parameters of the simulated systems containing dendrimers

G	M (g / mol)	Nb	Nt	A (nm)
1	958	7	8	6.0
2	2028	15	16	6.0
3	4095	31	32	7.0
4	8229	63	64	8.5
5	16496	127	128	9.4

3. RESULTS

Main characteristics of any nanoparticle including dendrimers are their size, shape and internal structure as well as distribution of bioactive groups on their surface. Dendrimer size is usually characterized by its mean square radius of gyration (see Fig1a and Table II). We have found that the dependence of Rg on molecular weight M for polylysine dendrimers (Figure 1a) is well described by a power law with exponent 0.34 which is close to value 0.33 typical for spherical particles with a constant density.

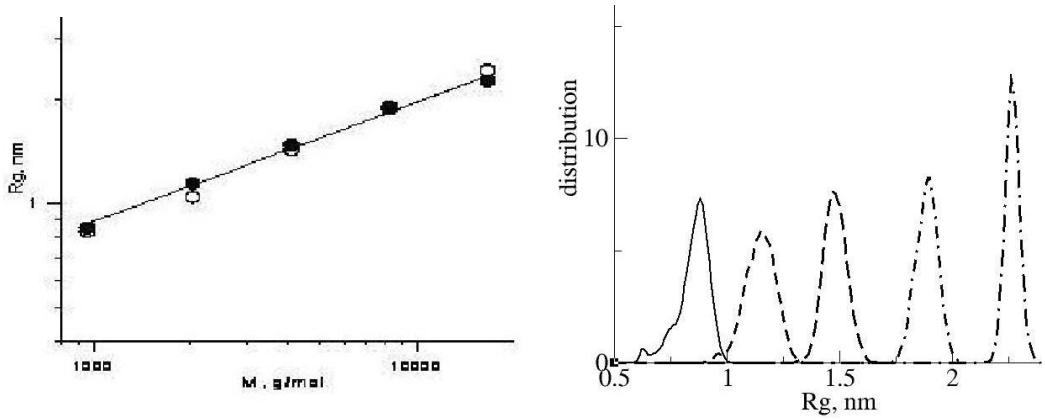

Figure 1 a) Dependence of the radius of gyration Rg on the molecular weight M of PL dendrimers. The filled symbols correspond to dendrimer simulation with AMBER, and hollow - with CHARMM force field, b) the distribution function of Rg for PL dendrimers: G = 1 - solid line, 2 - short dotted, 3 - long dashed, 4 - short dash-dot and 5 - long dash-dotted line.

However, more quick density increase can be expected for the higher generation dendrimers because their molecular weight increases with the number of generations faster than their size. For example, Gotze et al. [15] showed that for coarse-grained model of neutral flexible dendrimers with repulsive Lennard – Jones interactions the exponent of power law for Rg dependence on M is about 0.33 only for G4-G6 generations of dendrimers and decreases to 0.24 for G7 - G9 generations of dendrimers.

The distribution function of the radius of gyration Rg for dendrimers of different generations (G = 1-5) is shown in Figure 1b. The peak positions of this function increase with G, however the fluctuations (half-width of the distribution function Rg) decreases monotonically with the size of the dendrimer. This means that PL dendrimers become more "rigid" with increase of generation G.

The shape of the dendrimer can be characterized by means of its inertia tensor. Diagonalization of this tensor gives the three eigenvalues that allow to evaluate the shape anisotropy of PL dendrimers. Instantaneous eigenvalues were calculated at each time moment, and then they were averaged over the entire molecular dynamics trajectory.

Table 2. Ratio of the principal moments of λ_1: λ_2: λ_3 of the inertia tensor for lysine dendrimers generations G = 1-5

G	1	2	3	4	5
λ_1: λ_2: λ_3	1:0.94:0.56	1:0.92:0.65	1:0.93:0.66	1:0.92:0.76	1:0.95:0.82

As seen from Table 2, for all the studied lysine dendrimers the values of λ_1 and λ_2 are close to each other, and λ_3 has substantially smaller value (especially for dendrimers with a small number of generations). It means that the shape of dendrimers of small generations is close to the disk. Difference between eigenvalues λ_1, λ_2 and λ_3 is reduced with generation number of dendrimer G, indicating the approach of the dendrimer to spherical shape. Such a behavior was obtained earlier for symmetrically branched dendrimers (for example, for PAMAM dendrimers see Liu [16]).

The internal structure of the dendrimer may be characterized by the density profile of its atoms relative to its center of mass. We obtained the density profile for polylysine dendrimers of generation G=1-5 (see Figure 2a) and found that it is in good agreement with the theoretical "dense core - loose shell model [17]." Previously it was shown that the same model is valid for symmetrical branching dendrimers, such as, for example, PAMAM [18]. Changes in the curves with increasing generation number are also similar to those observed for symmetric dendrimers. All studied dendrimers have maximum density near the center. A similar maximum is observed in the simulation (both by Monte Carlo and molecular dynamics) of many symmetric dendrimers. For lower generation dendrimers (G = 1-2) the density decreases monotonically with increasing the distance r from the center of mass. For higher generation dendrimers (G = 3-5) density profile has a plateau. The similar plateau is observed for symmetric dendrimers with large numbers of generations [18].

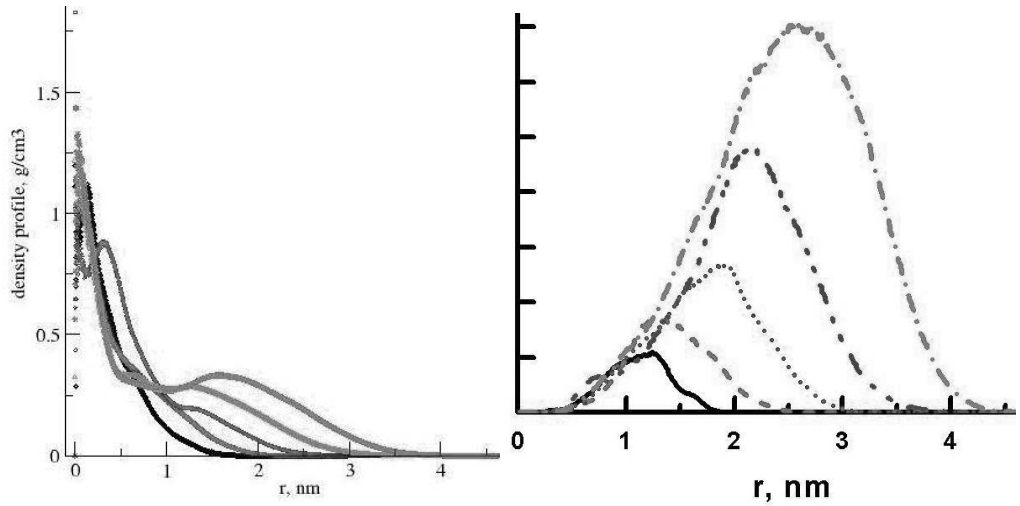

Figure 2 a) The density distribution for PL dendrimers generations G 1 to 5 (density dependence on the distance from the dendrimer center of mass), b) the distribution of end groups at a distance r from the center of the dendrimer G = 1 - solid, 2 - dashed, 3 - dotted 4 - double dotted bar, 5 – dash-dotted lines (arbitrary units).

The distribution of terminal groups is important characteristic of dendrimers. As mentioned above, our data support a model "dense core-loose shell" model [17] for dendrimers with asymmetric branching. This model is considered as an alternative to the originally proposed by de Gennes and Hervet theoretical model "hollow core - a dense shell" [19] for the density of the dendrimers.

In their model, all branches of the dendrimer are equally stretched and all the terminal groups are located at the same distance from the center of the molecule. Their model can describe the dendrimers with rigid immobile branches resembling snowflakes or dandelions. Implementation model of de Gennes-Hervet [19] leads to overcrowding and strong steric interactions on the periphery of the molecule. That is why branches of most of real dendrimers usually bent or turned back (the effect of back-folding) which leads to more uniform filling of the interior space by the dendrimer atoms. As a result sufficiently large number of end groups can be found in the dendrimer interior and even near to its center of mass. Back-folding was previously observed for the terminal groups, and for the internal branching point (subgenerations) of symmetrical dendrimers (see, for example, [18]).

As we already noted, the contour length of spacers (linear fragments between adjacent branch points) originating from each branch point of polylysine dendrimers differs by more than two times. Therefore, even if all branches of these asymmetric dendrimers are fully extended, the contour length of path for particular end groups will be different. It will be determined by number of short and long spacers in this particular path (by combinatorial rule of Pascal's triangle). For symmetric dendrimers the contour length of all paths from the center to all ends is the same, so this distribution will take the form of the delta function. Thus for uniform filling of the space inside symmetric dendrimers it needs back folding of end groups. At the same time, dendrimers with asymmetrical branching of the terminal groups will be distributed inside the dendrimers even without the effect of back-folding and we calculated this distribution for completely extended branches (not shown).

Distribution of terminal groups, which we obtained for PL dendrimers from the MD simulations (see Figure 2b), is similar to the corresponding distribution for the fully extended branches, but all curves are shifted toward smaller distances to the center. This is due to the additional effect of back-folding. Thus we have shown that the effect of back-folding exists not only in symmetric dendrimers with flexible spacers, but also in real polylysine dendrimers with asymmetric branching. This means that the effect of back-folding is a universal feature of dendrimers regardless of symmetry of branching.

CONCLUSION

A systematic molecular modeling of polylysine dendrimers of different generations (G = 1-5) with an asymmetric branching is performed. It is shown that the global structural characteristics of asymmetric lysine dendrimers are similar to corresponding properties of the symmetrical dendrimers such as PAMAM. In particular, we obtained that the dependence of dendrimer size and the shape anisotropy on the molecular weight, as well as the changes in the internal structure of PL dendrimers with generation number are very close to that of symmetrical dendrimers. Our calculations also show that for asymmetric PL dendrimers "a dense core and a loose shell" model [17] works equally well as for dendrimers with symmetric branching points. Taken together, these data suggest that asymmetrically branched

PL dendrimers have global structural properties similar to those of dendrimers with symmetrical branching, which is important for their practical use in various biomedical applications.

All computer calculations were performed on the supercomputer "Lomonosov" in Computer Centre of MSU. This work was partially supported by the Government of Russian Federation (grant 074-U01).

REFERENCES

[1] S. M. Grayson, J. M. *J. Frechet, Chem. Rev*. 101. 3819 (2001).
[2] A. W. Bosman, H. M. Janssen, E. W. Meijer, *Chem. Rev*. 99. 1665 (1999).
[3] L. Crespo, G. Sanclimens, M. Pons, E. Giralt, M. Royo, F. Albericio, *Chem. Rev*.105,1663 (2005).
[4] C. Rao, J. P. Tam, *J. Am. Chem. Soc.* 116. 6975 (1994).
[5] T. Darbre, J. L. Reymond, *Acc. Chem. Res*. 39. 925 (2006).
[6] B. Klajnert, J. Janiszewska, Z..Urbanczyk-Lipkowska, M. Bryszewska, D. Shcharbin, *Int, J. Pharm*. 309. 208 (2006).
[7] D. Tyssen et al, *PLoS ONE* 5. e12309 (2010).
[8] I. M. Neelov et al, *Curr.Med.Chem*. 20. 134 (2013).
[9] B. J. Boyd, L.M. Kaminskas, P. Karellas, G. Krippner, R. Lessene, C. Porter. *J. Mol. Pharm*. 3, 614 (2006).
[10] S. Javor, A. Natalello, S. M. Doglia, J. L. Reymond *J. Am. Chem. Soc*. 130. 17248 (2008);
[11] B. P. Roberts, M. J. Scanlon, G. Y. Krippner, D. K. Chalmers, *Macromol.* 42. 2775 (2009).
[12] L. Filipe, M. Machuqueiro, A. Baptista, *J. Am. Chem. Soc*. 133. 5042 (2011).
[13] I. M. Neelov, D. A. Markelov, A. G. Falkovich, M. Yu. Ilyash, B. M. Okrugin, A. A. Darinskii, *Polymer Sci.* C. 55. 154 (2013).
[14] G. P. Vlasov et al, Rus. *J. Bioorg. Chem*. 30. 12 (2004).
[15] I.O. Gotze, C. N. Likos, *Macromolecules* 36. 8189 (2003).
[16] Y. Liu, V. S. Bryantsev, M. S. Diallo, W. A. Goddard, *J. Am. Chem. Soc*. 131.2798 (2009).
[17] D. Boris, M. Rubinstein *Macromol.* 1996, *29,* 7251-7260.
[18] J. S. Klos, J. U. Sommer, *Macromol.* 42. 4878 (2009);43. 4418 (2010).
[19] P. G. D. Gennes, H. Hervet, *J. Phys. Lett*. 44. 351 (1983).

Smart Nanocomposites
Volume 5, Number 2
ISSN: 1949-4823

ADSORPTION OF A PERIODIC HETEROPOLYMER ONTO A PERIODIC CHEMICALLY HETEROGENEOUS SURFACE: A THEORETICAL STUDY USING A SIMPLE DIRECTED WALK MODEL

Alexey A. Polotsky*

Institute of Macromolecular Compounds, Russian Academy of Sciences, St. Petersburg, Russia and St. Petersburg National Research University of Information Technologies, Mechanics and Optics, St. Petersburg, Russia

ABSTRACT

The problem of a periodic heteropolymer adsorption onto a periodic heterogeneous surface is solved exactly in the framework of the two-dimensional partly directed walk model and the generating functions approach. Analysis of the adsorption transition point dependence on polymer and surface block sizes reveals interesting "odd-even" and "recognition" effects. Beyond the transition point, temperature dependences of the main conformational and thermodynamic characteristics demonstrate that adsorption can occur as a two-stage process which is characterized by appearance of the second maximum on the heat capacity curves.

Keywords: polymer adsorption, periodic heteropolymer, periodic heterogeneous surface

INTRODUCTION

Adsorption of heteropolymers – polymers composed of monomer units of two and more types, onto chemically heterogeneous surfaces – was intensively studied in the last decades. A particular interest to this problem is motivated to its connection to the question of molecular recognition, playing a crucial role in living organisms and in various biomedical/ biotechnological applications.

To understand the mechanisms of the polymer-surface recognition, the problem was extensively investigated from different angles by using relatively simple and physically transparent models. Here a particular role was played by the so called directed walk models, where conformations of polymer chains are represented as directed walks on a lattice [1, 2].

* E-mail: alexey.polotsky@gmail.com

The main advantage of using the directed walk models is that in the most cases they are exactly solvable. For the problem of heteropolymer adsorption onto heterogeneous surface, the simplest (or "minimal") model which is not reduced to simpler situations and takes into account the heterogeneity in both the polymer and the surface is the 2-dimensional partially directed walk (2D-PDW). In the 2D-PDW, steps in the "west" direction and immediate reversal steps are forbidden.

RESULTS AND DISCUSSION

We showed how the approach developed earlier for the adsorption of a random copolymer onto a homogeneous [3] or random [4] surface can be extended to the regular periodic case [5]. Specifically, we considered a single periodic heteropolymer chain adsorbing onto a periodic heterogeneous surface. In the general case, the heteropolymer chain can be represented as a periodic monomer sequence with a repeating unit of m_p monomers $(M_1, M_2, \ldots, M_{mp})_x$. Since, in the 2D-PDW model, that is, in two dimensions, the adsorbing surface is merely a line, the periodic surface is represented in a similar way, as one-dimensional sequence of sites with a repeating unit of m_s sites: $(S_1, S_2, \ldots, S_{ms})_x$. To describe interactions between different monomer units and surface sites, $m_p \times m_s$ interaction energies, ε_{ij} , should be defined.

An important observation was that the periodic heteropolymer can be represented as a first order Markov chain with m_p states and *circulant* transition probability matrix (of dimensions $m_p \times m_p$) with unit entries

$$\mathbf{P} = \begin{pmatrix} 0 & 1 & 0 & . & 0 \\ 0 & 0 & 1 & . & 0 \\ . & . & . & . & . \\ 0 & 0 & 0 & . & 1 \\ 1 & 0 & 0 & . & 0 \end{pmatrix} \tag{1}$$

Similarly, the periodic sequence of surface sites can be represented by the matrix **S** that has the same structure but different dimensions ($m_s \times m_s$).

To solve the problem we used the generating functions (GFs) approach, where, instead of calculating the partition function

$$Z_n(\beta) = \sum_{\omega} \exp[-\beta E(\omega)], \tag{2}$$

one computes its GF:

$$\Xi(z) = \sum_{n=1}^{\infty} Z_n(\beta) z^n , \tag{3}$$

which is typically a much more easier task. Here $\beta = 1/k_B T$ is the inverse temperature, ω

stands for chain conformation, E denotes the energy of this particular conformation, n is the chain length, and z is the auxiliary variable conjugate to n. Then, in the long chain limit,

$$Z_n(\beta) = z_c^{-n} , \tag{4}$$

where z_c is the smallest singularity (radius of convergence) of the GF $\Xi(z)$. The equation for funding the smallest singularity z_c is a determinant equation that requires computation of the determinant of a $(m_p\, m_s) \times (m_p\, m_s)$ matrix, it can be easily solved with the aid of standard numerical computational packages like, for example, *Scilab*. Once the smallest singularity z_c (that is, the partition function of adsorbed chain) is found, various *observables* can be calculated by differentiating it with respect to the proper variable, see [5] for the details.

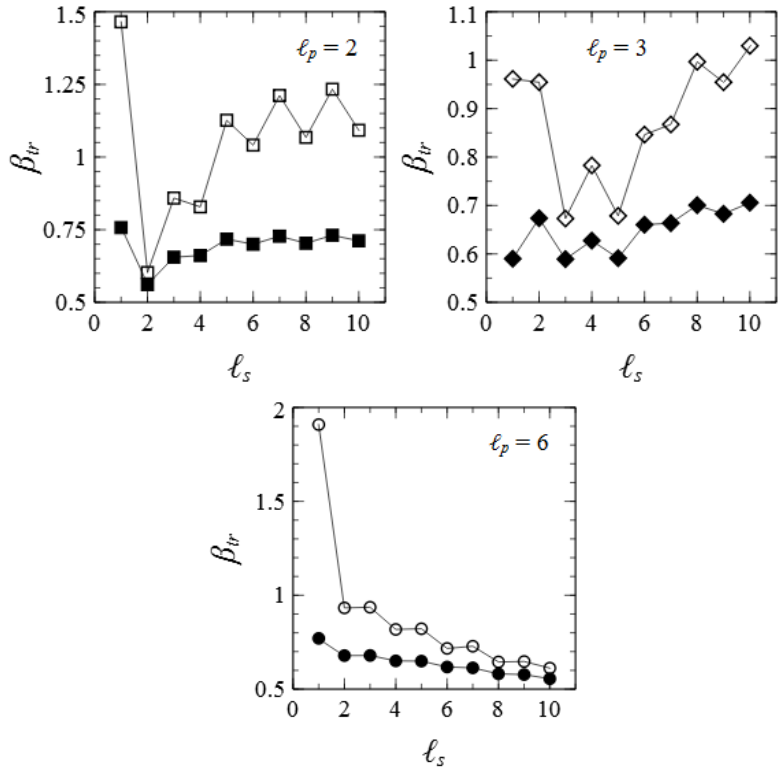

Figure 1. Inverse adsorption transition temperature for a symmetric *AB*-copolymer adsorbing onto a symmetric *ab*-surface as a function of copolymer block length, $\ell_p = m_p/2$, for various surface block sizes, $\ell_s = m_s/2 = 2$, 3, and 6, as indicated, calculated for $\varepsilon_{Aa} = \varepsilon_{Bb} = -1$, $\varepsilon_{Ab} = \varepsilon_{Ba} = 0$ (full symbols) or +1 (open symbols).

We applied the developed approach to adsorption of a symmetric multiblock *AB*-copolymer onto a symmetric multiblock two-letter *ab*-surface [5]. Here "symmetric" means that the copolymer has a structure $(A_{\ell_p}B_{\ell_p})_x$ and the surface $(a_{\ell_s}b_{\ell_s})_x$, that is, the period of the sequence is $m_p = 2\ell_p$ for the polymer and $m_s = 2\ell_s$ for the surface. Analysis of the adsorption transition point dependence on polymer and surface block sizes and different sets of polymer-surface interaction parameters reveals "odd-even" alternation of the inverse transition

temperature β_{tr} and "recognition effect" (Figure 1, ℓ_p = 2 and 3), that is, for a given ℓ_p there exists the value of ℓ_s corresponding to the lowest β_{tr}. When the periods become larger both effects, however, disappear (Figure 1, ℓ_p = 6).

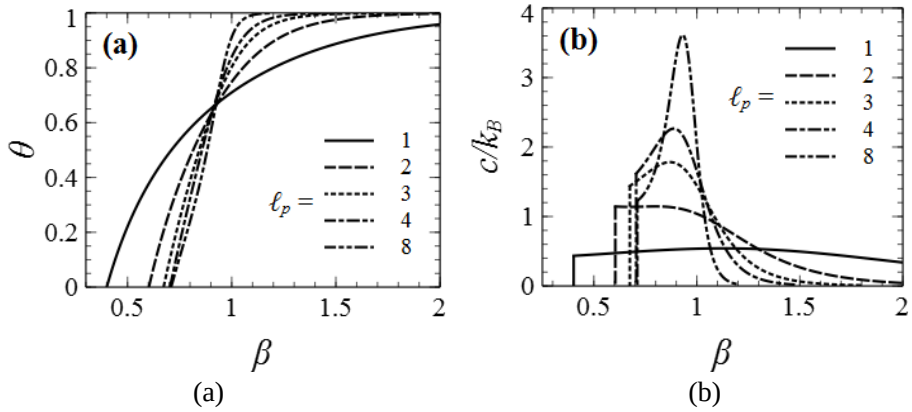

(a) (b)

Figure 2. Fraction adsorbed monomer units (a) and heat capacity (d) as functions of inverse temperature b for a symmetric *AB*-copolymer adsorbing onto a symmetric *ab*-surface as a function of copolymer block length calculated for $\varepsilon_{Aa} = \varepsilon_{Bb} = -1$, $\varepsilon_{Ab} = \varepsilon_{Ba} = +1$ at various $\ell_p = \ell_s$ (ideal matching between polymer and surface patterns) as indicated.

Beyond the transition point, temperature dependences of the main conformational and thermodynamic characteristics demonstrate that adsorption can occur as a two-stage process, where binding of the polymer chain to the surface is followed by "tuning" the chain conformations in order to maximize the number of energetically favorable contacts. The two-stage adsorption is characterized by appearance of the second maximum on the heat capacity curves (Figure 2).

CONCLUSION

In the present work, adsorption of a periodic heteropolymer onto a periodic heterogeneous surface is studied by using the 2-dimensional partially directed walk model of the polymer.

We show how the generating functions approach developed for the adsorption of a random copolymer onto a random surface in [4] can be extended to the case of an arbitrary periodic heteropolymer and a chemically heterogeneous surface.

The developed approach was then applied to adsorption of a symmetric multiblock copolymer onto a symmetric multiblock two-letter surface, where we revealed interesting "odd-even" and "recognition" effects for the transition point and demonstrated that that adsorption can occur as a two-stage process, where binding of the polymer chain to the surface is followed by "tuning" the chain conformations in order to maximize the number of energetically favorable contacts.

It is important to note that the developed approach is quite general and can be straightforwardly applied to study, for example, the effects of asymmetry in polymer and surface composition or that of a larger alphabet size.

ACKNOWLEDGMENT

This work is supported by the Government of Russian Federation (grant 074-U01).

REFERENCES

[1] Janse van Rensburg, E. J. *The Statistical Mechanics of Interacting Walks, Polygons, Animals and Vesicles;* Oxford Lecture Series in Mathematics and Its Applications 18; Oxford University Press: Oxford, 2000.
[2] Janse van Rensburg, E. J. *J. Phys. A: Math. Gen.* 2003, *36*, R11.
[3] Polotsky, A.; Degenhard, A.; Schmid, F. *J. Chem. Phys.* 2009, *131*, 054903.
[4] Polotsky, A. A. *J. Phys A: Math. Theor.* 2012, *45*, 425004.
[5] Polotsky, A. A. *J. Phys. A: Math. Theor.* 2014, *47*, 245002.

Smart Nanocomposites
Volume 5, Number 2
ISSN: 1949-4823

ON THE STRUCTURE OF A STAR BRUSH SUBJECTED TO DEFORMATION

***Alexey A. Polotsky*[*,1,2], *Alexey K. Misorin*[1,3] *and Tatiana M. Birshtein*[1,3]**

[1]Institute of Macromolecular Compounds, Russian Academy of Sciences, St. Petersburg, Russia
[2]St. Petersburg National Research University of Information Technologies, Mechanics and Optics, St. Petersburg, Russia
[3]St. Petersburg State University, Physics Department, Petrodvorets, St. Petersburg, Russia

ABSTRACT

A planar polymer brush of arm-grafted polymer stars subjected to external deformation is studied theoretically by using a simple mean-field model of the star brush that takes into account segregation of the brush-forming stars in two populations of weakly and strongly extended stars. The polymer density profile in the brush is assumed to have a "two-step" shape. We show that the theory quantitatively accurately describes earlier numerical results obtained with Scheutjens-Fleer numerical self-consistent field approach for free (non-deformed) star brush. We study compression of the star brush by an impenetrable plane and demonstrate that depending on the grafting density compression could affect the two-population brush structure in opposite ways. In sparsely grafted brushes the fraction of stars in the stretched population increases while in densely grafted brushes it decreases with deformation.

Keywords: polymer brush, polymer star, brush deformation

INTRODUCTION

Layers of polymers densely grafted to impenetrable surfaces, or polymer brushes, are intensively studied, both experimentally and theoretically, for more than 30 years, and the interest to such systems is keeping on growing. Practical interest to polymer brushes is motivated by their use in surface modification which allows to improve the surface biocompatibility, barrier, or tribological properties. Modification of surfaces by the brushes

[*] E-mail: alexey.polotsky@gmail.com

with stimuli-responsive properties (thermosensitive, pH-sensitive, etc.) allows obtaining the so called “smart” surfaces.

The present work is devoted to theoretical study of brushes made of arm-grafted polymer stars immersed into a good solvent. Earlier self-consistent field (SCF) modeling [1, 2] and Langevin dynamics simulation [3] studies have revealed a non-trivial structure of the star brush (Figure 1a): At moderate and high grafting density the stars in the brush are divided into two populations (i) those with weakly extended arms and (ii) those with a very strongly stretched grafting arm (stem) and all free arms extended toward the solvent.

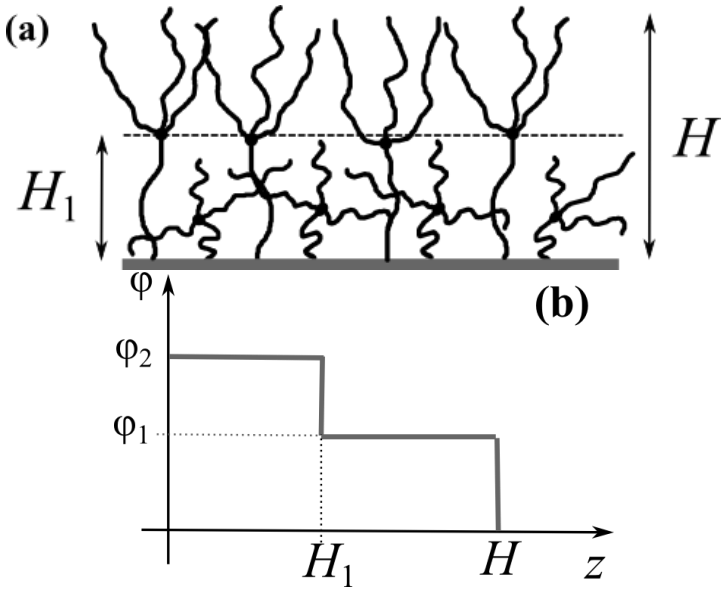

Figure 1. A schematic picture (a) and a two-step density profile (b) of the two-population star brush.

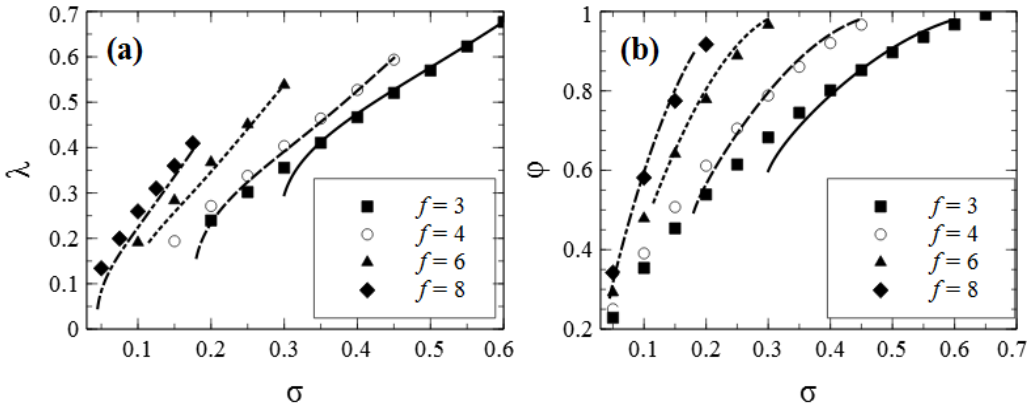

Figure 2. Fraction of stars in the extended population (a) and average polymer density (b) as functions of grafting density in a brush made of arm-grafted stars with various number of arms *f* calculated from the results of SCF modeling [2] (symbols) and theory (lines).

We developed a simple mean-field theory of the star brush that takes into account its two-population structure [4].

The theory is based on a box-like model of the brush: The brush is divided into two parts, in the inner part, close to the grafting surface, stars of weakly stretched population and stems of extended stars are found while the free arms of extended stars are located in the outer part of the brush (Figure 1a).

The polymer density profile in the brush is assumed to have a "two-step" shape (Figure 1b). Stars in the extended population are assumed to be equally stretched, the position of extended stars' branching points sets the boundary between two parts of the brush. This model is very similar to that introduced by Merlitz et al. [5], except that in [5] polymer density in two parts of the brush was the same (and the profile was a "one-step"). Figure 2 shows that the theory quantitatively accurately describes earlier numerical SCF results [2] for free star brush (SCF calculations in [2] and in the present study were performed by using *SFBox* software developed in Wageningen University).

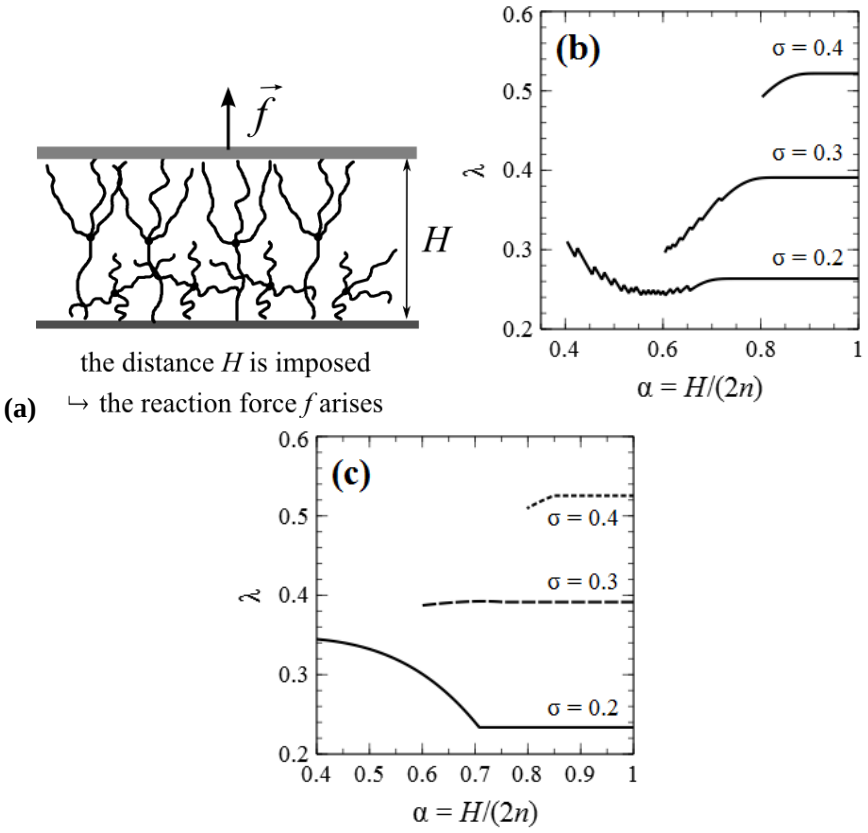

Figure 4. (a) Schematic picture of deformed star brush. (b, c) Fraction of stars in the extended population as function of the brush deformation in a brush made of four-arm-grafted stars ($f = 4$) at various grafting density σ as indicated calculated from the results of SCF modeling (b) and theory (c). The deformation is expressed via the reduced distance between grafting and squeezing planes $\alpha = H/(2n)$ where, n is the star arm length.

We studied compression of a star brush by an impenetrable plane (Figure 3a) by using the Scheutjens-Fleer numerical SCF approach and by applying the developed mean-field theory [4]. Again, a very good quantitative agreement was observed. In particular, it was demonstrated than deformation affects the two-population structure of the star brush; moreover, the effect essentially depends on the density at which stars are grafted: in sparsely grafted brushes the fraction of stars in the stretched population increases while in densely grafted brushes it decreases with deformation (Figure 3b, c).

ACKNOWLEDGMENTS

This work was supported by the Russian Foundation for Basic Research (grant 14-03-00372-a), by the Department of Chemistry and Material Science of the Russian Academy of Sciences, and by the Government of Russian Federation (grant 074-U01).

REFERENCES

[1] Polotsky, A. A.; Gillich, T.; Borisov, O. V.; Leermakers, F. A. M.; Textor, M.; Birshtein, T. M. *Macromolecules* 2010, *43*, 9555-9566.
[2] Polotsky, A. A.; Leermakers, F. A. M.; Zhulina, E. B.; Birshtein, T. M. *Macromolecules* 2012, *45*, 7260-7273.
[3] Merlitz, H.; Wu, C.-X.; Sommer, J.-U. *Macromolecules* 2011, *44*, 7043-7049.
[4] Polotsky, A. A.; Misorin, A. K.; Zhulina, E. B.; Birshtein, T. M. *Macromol. Symp.* 2015, *348*, 33-43.
[5] Merlitz, H.; Cui, W.; Wu, C.-X.; Sommer, J.-U. *Macromolecules* 2013, *46*, 1248-1252.

REVIEW ARTICLE UPDATE

"Phase and Structure Transitions in Nanoparticles of Semiconductors within Porous

Dielectric Matrices" written by S. Khanin, V. Solovyev, S. Trifonov, and V. Veisman (Smart Nanocomposites, 2013, Volume 4, Issue 1, P. 29 - 36)

Taking into account priority considerations, the authors should like to add one more original paper (which we have learned about recently) to the list of references:

[15] Ilinski A., Silva-Andrade F., Shadrin E. The Influence of the Phase Transition in the Energy of Photonic Band Gap in the Opal Based Composites // Conferences, Cancun 2004. Mexico.

The other papers on this topic written by S. Khanin and co-workers are cited in the monograph [6].